

UNIVERSITY OF COPENHAGEN
THE FACULTY OF SCIENCE

Ph.D. Thesis

***R*-Hadron Search at ATLAS**

Author:

Simon J.F. HEISTERKAMP

Supervisor:

Troels C. PETERSEN

This thesis has been submitted to the PhD School
of The Faculty of Science, University of Copenhagen

21. November, 2012

Preface

The work presented in this thesis was carried out by my group based at the Niels Bohr Institute, Copenhagen under the leadership of Troels C. Petersen in collaboration with a group from the Technion University at Haifa, Israel led by Professor Shlomit Tarem. Our work was based on earlier work on the same topic within the ATLAS collaboration which has resulted in numerous publications such as theses by Mackeprang [1], Kraan [2] and Ohm [3] and papers published by the ATLAS collaboration [4–7].

The parts that are truly new and have not been used in earlier work are the calibrations presented in chapter 7, the weighted combination of layers and sub-detectors to one overall β measurement presented in chapter 8, and the inclusion of the liquid argon calorimeters. Also our work was the first to use all information available from the ATLAS detector in a combined analysis.

Our work was submitted to Phys.Lett.B. titled *Searches for heavy long-lived sleptons and R-Hadrons with the ATLAS detector in pp collisions at $\sqrt{s} = 7$ TeV* [8].

In addition to this physics analysis I have carried out technical work on the transition radiation tracker (TRT), an ATLAS sub-detector. This work is described along with the description of the TRT in chapter 5.

Abstract

In this thesis I motivate and present a search for long lived massive R -hadrons using the data collected by the ATLAS detector in 2011. Both ionisation- and time-of-flight-based methods are described. Since no signal was found, a lower limit on the mass of such particles is set. The analysis was also published by the ATLAS collaboration in Phys.Lett.B. titled ‘Searches for heavy long-lived sleptons and R-Hadrons with the ATLAS detector in pp collisions at $\sqrt{s} = 7$ TeV’.

Summary in Danish

Denne afhandling handler om søgningen efter en ny type partikel, såkaldte R -hadroner, som kunne blive skabt i proton-proton kollisioner ved LHC acceleratoren. Til vores analyse brugte vi data fra ATLAS detektoren og vores arbejde har ført til en publikation fra ATLAS kollaborationen med titlen ‘Searches for heavy long-lived sleptons and R-Hadrons with the ATLAS detector in pp collisions at $\sqrt{s} = 7$ TeV’.

R -hadroner er sammensatte partikler som består af en tung, lang levende partikel som bærer farveladningen fra kvantekromodynamik, sammen med lette standard-model kvarker og gluoner. Efter skabelsen i midten af ATLAS ville den slags partikel bevæge sig ud igennem hele detektoren lige som en myon. Signalerne vi brugte var målinger af specifik ionisation og tidsmålinger som begge to gav et estimat af partikelhastigheden. Hastigheden kunne derefter kombineres med den målte impuls til at give et estimat af partiklens masse. Vi ledte efter et signal ved at sammenligne antallet af begivenheder hvor begge masser lå over et vist niveau mellem data og en baggrundsforventning.

Vi fandt ingen tegn på eksistensen af sådanne tunge partikler i masseområdet mellem 100 til 1500 GeV/ c^2 . Ved at sammenligne med en teoretisk forventet produktionsrate kunne vi udelukke eksistensen af R -hadroner med en masse under 985 GeV eller 612 GeV for henholdsvis gluino eller stop baserede R -hadroner.

Summary in English

Please see section 1.2.

Contents

Preface	2
Abstract	3
Summary in Danish	3
Summary in English	3
1 Introduction	9
1.1 Motivation	9
1.2 Analysis Outline	10
1.3 Document Layout	12
1.4 The Author's Contributions	13
2 Theory	15
2.1 Units and Coordinates	15
2.2 Quantum Field Theory	16
2.3 The Standard Model	17
2.4 Electroweak Theory	17
2.5 Quantum Chromo Dynamics	18
2.5.1 Hadronisation	19
2.6 Particle Content	19
2.7 Stable and Meta-Stable Particles in the SM	20
2.8 Beyond the Standard Model	22
2.8.1 Gravity	22
2.8.2 Dark Matter	23
2.8.3 The Hierarchy Problem	23
2.8.4 Dark Energy	24
2.8.5 Models Beyond the SM	25
2.8.6 Supersymmetry	26
3 Stable Massive Particle Theory	29
3.1 Motivation	29
3.1.1 Theoretical Motivation	29
3.1.2 Experimental Motivation	31
3.2 Production and Decay	33
3.2.1 Production	33

3.2.2	Decay	33
3.2.3	ISR and FSR	34
3.3	Types of Stable Massive Particles	34
3.3.1	Sleptons	35
3.3.2	R -hadrons	35
3.4	R -hadron Hadronisation and Hadronic Interactions	36
3.4.1	Hadronisation	36
3.4.2	Interactions	36
3.5	Cross-Section Calculations	38
4	The CERN Accelerator Complex	39
4.1	The Accelerators	39
4.2	The Detectors	42
4.3	Proton Collision Physics	42
4.3.1	The Rapidity Plateau	43
4.3.2	Total Cross-Section	44
4.4	Accelerator Operation	44
5	The ATLAS Detector	47
5.1	Layout	47
5.2	The Magnet System	49
5.3	The Inner Detector	49
5.3.1	Interactions of Ionising Particles	50
5.4	The Pixel Detector	51
5.4.1	Layout	51
5.4.2	Specific Ionisation Measurement	52
5.5	The Silicon Strip Detector	53
5.6	The Transition Radiation Tracker	54
5.6.1	Layout	54
5.6.2	Signal Reception	54
5.6.3	Aside on Electron Gas Drift	55
5.6.4	Tracking	57
5.6.5	Electron Identification	58
5.6.6	Double Binomial Fit Method	60
5.6.7	Specific Energy Loss Measurement	63
5.6.8	Time of Flight Measurement	65
5.7	The Calorimeters	66
5.8	The Muon Spectrometer	68
5.9	The Trigger System	69
5.9.1	Trigger Pre-scaling	71
5.9.2	Luminosity Counting	72
5.9.3	Data Storage	73
5.10	Timing in ATLAS	73
5.11	Detector Operation	74

6	Techniques	77
6.1	ATLAS Full Chain	77
6.2	From Collisions to Plots	78
6.3	Data Samples	78
6.4	Triggering	78
6.4.1	E_T^{miss} Trigger	80
6.4.2	Muon Trigger	81
6.5	Monte Carlo Simulation	81
6.5.1	MC samples	83
6.5.2	Pile-up Re-weighting	85
6.6	Calibration Samples	85
7	Detector calibration	89
7.1	Motivation	89
7.2	dE/dx to $\beta\gamma$ Calibration	92
7.3	Time-of-Flight to β Calibration	92
7.3.1	Geometric Errors	94
7.3.2	Timing Errors	98
7.3.3	Calibration Overview	101
7.3.4	Motivation	103
7.4	Results	105
8	Analysis Strategy	109
8.1	Goals	109
8.2	Choice of Sub-detector	110
8.3	Combination Strategy	111
8.3.1	Global Track Fit	113
8.3.2	Likelihood Method	114
8.3.3	Average + 2D Cut Method	116
8.4	R -hadron versus Slepton Search	117
9	Quality Selection	119
9.1	Quality Check	120
9.1.1	Stream Overlap Removal	120
9.1.2	Detector Conditions	121
9.2	Candidate Selection	121
10	Final Selection & Background	127
10.1	Goals	127
10.1.1	Motivation for Data-Driven Background	127
10.2	Final Selection	128
10.2.1	Primary Estimator Cuts	129
10.2.2	Derived Estimator Cuts	129
10.3	Background Generation	130

10.4	Limit Setting	135
10.4.1	Derivation of CL_s	135
10.4.2	Implementation	137
11	Results	139
11.1	Interpretation of Limits	139
11.2	Comparison to Competing Experiments	142
11.3	Systematic Uncertainties	142
11.3.1	Theoretical Cross Section	143
11.3.2	Expected Signal	143
11.3.3	Background Estimation	144
12	Outlook & Discussion	145
12.1	Looking Back	145
12.1.1	Calibration	145
12.1.2	Trigger	146
12.1.3	MC Charge-Flip Truth	146
12.1.4	Flight Path Length	146
12.2	Looking Ahead	147
12.2.1	LHC Schedule	147
12.2.2	Mass Reach	147
12.2.3	Pile-Up	147
12.2.4	Trigger	147
12.2.5	Time of Flight	148
A	Additional Figures	149
	List of Figures	151
	List of Tables	157
	Bibliography	159

Chapter 1

Introduction

1.1 Motivation

Modern particle physics has reached a point where the Standard Model (SM) predicts no further particles in order to be self consistent. Also, all particles that have been observed can be described consistently within the SM. Thus the SM stands as a very good theory that is unchallenged by any particle-physics data. Yet, at the same time we know that the Standard Model is not complete and must break down at energies beyond those on which it was originally based. Also, there are phenomena in other areas of physics that can not be explained by the SM, such as the Dark Matter and Dark energy of astronomy, or even gravity itself. Of these Dark Matter is thought to be the one most suitable for a particle explanation.

With the availability of new data from the LHC at unprecedented high energy scales we would ideally like to make progress in our search for deeper understanding of the natural world just by looking at the data and inferring from them any new laws of nature that are active in these new energy regions. Unfortunately our experiments today are so complex, and so many peripheral effects are convoluted into the data, that a straight deduction of this kind is no longer possible. This is why we rely on mathematical models to guess what nature is like and then we try to verify or falsify these guesses experimentally where the observed outcome is compared to an outcome predicted by a model. Making good models that are consistent both with themselves and with existing experimental data as well as making interesting predictions for new data is a difficult job in and of itself and is the realm of theoretical physics.

Much experimental work today consists of taking these new mathematical models and trying to find or exclude the new particles or interactions they predict. The models provide a useful starting point at which to search for signals in a vast multi-parameter space of possible signatures. However, if these searches are too closely based on the predicted models, new physics

might be missed unless it matches one of the models. Historically the most interesting new discoveries in physics were those that did not conform to any predicted or anticipated models. Therefore many experimentalists today try to make their searches model independent wherever possible.

One type of new physics that is predicted by a range of models is the existence of new stable or meta-stable particles at masses that are accessible at the LHC. The lifetime of these heavy particles may be so great that they could be observed directly as they are passing through our detectors. These stable massive particles (SMP) present a very striking signature if they exist. There are no known particles or processes that could mimic the physical signal from an SMP and thus a search for SMPs has no irreducible background. Because of this it is possible to search for SMPs using physical intuition and data driven methods and thereby arrive at a model independent search, the epitome of experimental particle physics analysis.

Searches of this kind have been carried out before both at ATLAS [5] and at other experiments such as CMS [9], D0 [10], CDF [11] and others. In the work underlying this thesis we tried to improve upon previous ATLAS results [5, 7] by using improved calibration methods and more data.

1.2 Analysis Outline

The analysis presented in this thesis was intended to discover the existence of stable or meta-stable massive particles that may be created at the unprecedented high collision energies at the LHC and leave the detector without decaying. Should they not exist, the aim was to set an upper limit on the production cross section of such particles in as general a way as possible. Such a limit would be useful in constraining many proposed models of physics beyond the Standard Model (SM). The work was based on data from the ATLAS detector at the Large Hadron Collider (LHC) at Cern.

In this analysis we looked for particles that did not decay again and were stable at least on scales of the size of the detector. Thus such particles could be observed, detected and measured directly instead of via their decays. This made our analysis very unusual within the ATLAS collaboration where nearly all other analyses deal with decay products only. This led to a number of challenges where we had to address some low level issues ourselves, such as calibration, that would already be taken care of in a more standard analysis.

In our work we focussed on the search for R -hadrons, compound states of new massive coloured particles, hadronised with SM quarks and gluons. Although the heavy component of these hadrons originates in an unknown theory, the resulting compound particles nevertheless have well-modelled hadronic and electromagnetic interactions because the interactions nearly only proceed via the SM components. Our collaborators from the Technion institute in Israel used the same analysis framework, but tuned their cuts to

the search for sleptons, heavy stable leptons without colour charge and hence without hadronic interactions, such as those predicted by Supersymmetry (SUSY).

The way to look for both types of particles was by measuring their mass via their speed. Assuming a mass of a few hundred GeV the new particles, collectively called Stable Massive Particles (SMP) would be non-relativistic at typical LHC energies, a property which clearly separates them from any other known particle. The speed was measured in two different ways by several different sub-detectors using different technologies.

The pixel detector, the innermost tracker, is able to measure the specific ionisation of traversing particles. At speeds of $0.25 < \beta\gamma < 1.0$ the relationship between the specific ionisation and a particle's velocity is a single valued function, allowing a translation from one to the other.

The other speed measurement, a direct measurement of the time of flight (ToF) was performed by both the calorimeters and the muon spectrometer which both have a high timing resolution. Together with a known distance from the collision point each hit time in these detectors could be translated into a speed measurement, giving overall a very reasonable resolution on the particle's β .

The fact that no other SM particle can give a meaningful signal in either of these measurements was both a blessing and a curse for us. Since neither measurement is meaningful to carry out on SM particles, timing and specific ionisation (dE/dx) are not centrally calibrated like most other features of the ATLAS data. Also, both are not properly reproduced in simulated Monte Carlo samples. We therefore had to carry out extensive calibration on our data before the resolution became good enough for our purposes.

The timing systems suffer from random offsets that differ from one sub-detector to another, from run to run, and can depend on particle momentum, hit-energy deposit, etc. These offsets were calibrated using samples of muons tagged in data from $Z \rightarrow \mu\mu$ decays. Muons are known to have a $\beta \approx 1$ and the timing offsets as well as accuracy in various categories could thus be obtained.

The dE/dx measurements were calibrated using low momentum protons. Tagged from Δ baryon decays, the known proton mass and well measured momentum make these particles excellent calibration probes, allowing for a good calibration of the dE/dx to $\beta\gamma$ conversion function.

After all calibrations, each of these speed measurements was separately combined with the momentum obtained from the track curvature to give two measurements of the particle's mass. A signal of a true SMP would be expected to show a peak in both mass spectra. This gave a good rejection power against cases where only one or the other measurement randomly gave a very high mass. To be able to quantify our discovery potential, however we needed to find a good description of our background.

Since no known particles of high mass exist, the only source of back-

ground in the double-high-mass signal region were mismeasurement. Such outliers in the mass spectrum can come from an error in the momentum measurement, the ToF or the dE/dx . It is extremely unlikely for a error to occur in all three measurements at once such that a SM particle lands in the signal region. This is positive for our analysis, but makes it expensive to simulate Monte Carlo (MC) background in the signal region. For this and other reasons we decided to implement a data-driven background method.

If errors in the three measurements are totally uncorrelated, a large amount of background can quickly be generated by the following method: The distribution of each estimator is produced without any cut on the others. This gives a high-statistics graph from which a representative value can be chosen at random. A set of three random values of the three estimators can thus quickly be generated without a full simulation of a particle. By then combining these estimators into the mass measurements, a smooth distribution of the expected background can quickly be generated. Even a small admixture of true signal does not invalidate this method, as will be explained later. In practice, the distributions were not fully independent, but by binning in pseudorapidity η , sets of independent distributions could still be found.

Using this data-driven background, we could now evaluate the significance of the number of data events observed in the signal region of our analysis of the ATLAS data collected in 2011. No deviation from a background only hypothesis was found.

We proceeded to set cross section limits. For this we needed to evaluate the efficiency for discovering signal using our analysis. We used sets of simulated MC samples of R -hadrons of various masses and measured how efficient we were at selecting these tracks in our analysis. Using these numbers and the used total integrated luminosity of our data we were able to set cross section limits around 10^{-2} pb for most of the range of masses available to us (400 to 1400 GeV). Combining these with the cross section prediction as a function of mass in a certain supersymmetric model we were able to exclude \tilde{g} R -hadrons with masses below 985 GeV and \tilde{t} and \tilde{b} R -hadrons with masses below 683 and 612 GeV respectively.

1.3 Document Layout

In chapter 2 I start out by giving a brief introduction to the theory of particle physics in order to form a background upon which the further work can be understood. Chapter 3 dives further into the background and phenomenology of the particular type of SMP that we worked on namely R -hadrons. Chapters 4 and 5 introduce the experimental setup. The LHC accelerator and the ATLAS detector are introduced in some detail. Chapter 5 also includes an account of the technical work on the TRT that I carried out in

2010. This chapter also describes some aspects of the detector operation, such as triggering, in as far as they are relevant to our analysis. Some details on data processing and our computing setup are given in chapter 8. In chapter 7 I describe the various calibration schemes that we employed to calibrate the time measurements.

Chapter 8 then outlines how we intended to observe the stable massive particles. The data-driven background method used in our analysis is also introduced here. The several stages of selection are described in chapter 9. The limit setting procedure is described in chapter 10.

Finally chapter 11 presents the results of our search and the conclusions that can be drawn from them as well as an outlook for how this work might be extended into the future.

1.4 The Author's Contributions

In this section I summarise in how far the work presented in this thesis is attributable to my own efforts and which parts are my collaborators' work which is added here for completeness.

January to August 2010 I was involved in improving the electron identification capability of the TRT. For this I thoroughly revised a software tool that forms part of the ATLAS reconstruction algorithms, extending it with new, more detailed calibration and time-over-threshold based methods developed within the collaboration. This software work was accredited as authorship qualification.

For the main stable massive particle (SMP) search I was directly involved in planning, setting up and running the whole analysis since spring 2011. The search for lepton-like SMPs which also formed part of our combined analysis was more reliant on the muon spectrometer (MS) which our Israeli colleagues had more expertise on and was therefore left to them. This is also why the MS calibration is not described in as much detail as the calorimeter calibration which I was directly involved in.

Chapter 2

Theory

2.1 Units and Coordinates

Throughout this thesis I will use a system of measurement that is known as natural units. This is the standard in high energy physics (HEP). Natural units are based on a simple scaling which is

$$\hbar = c = 1. \tag{2.1}$$

This simplifies many equations of relativity and quantum field theory by removing those factors. It means that mass, impulse and energy are all measured in units of energy.¹ Multiples of eV (electron-volts) have a natural relationship to high energy physics (HEP) because they relate to the experimental setup, namely the electric acceleration of unit charges. They are therefore used as the unit of energy instead of the SI unit Joules.

The coordinate system of the ATLAS detector is set up such that the x -axis points to the centre of the accelerator ring, the y -axis points straight up and the z -axis points in the anti-clockwise direction of the accelerator, leading to a right-handed coordinate system. Often the cylindrical symmetric construction of ATLAS make it more appropriate to use a polar coordinate system centred on the z -axis with ϕ being the angle in the x - y plane starting at the x -axis. The physics of hadron collisions make it more appropriate to use pseudorapidity instead of a polar angle, defined as

$$\eta = -\ln \left[\tan \left(\frac{\theta}{2} \right) \right] \tag{2.2}$$

where θ is the polar angle away from the z -axis. Pseudorapidity is related to the relativistic rapidity in a way that is explained in more detail in section 4.3. Distances between particles are often expressed in terms of ΔR

¹Space and time would thus have units of inverse energy, but these are rarely used. Millimetres (mm) and nanoseconds (ns) are the conventional units in ATLAS.

defined as

$$\Delta R = \sqrt{(\Delta\eta)^2 + (\Delta\phi)^2}. \quad (2.3)$$

This should not be confused with r which is sometimes used as the radial distance from the beam-pipe, i.e.

$$r = \sqrt{x^2 + y^2} \quad (2.4)$$

In our analysis two different means of expressing speeds are used. β is the speed of the particle in units of the speed of light and thus has values in the interval $[0, 1)$. Speeds are also expressed as values of $\beta\gamma$ where γ is the Lorentz gamma factor. This is the more convenient quantity when working with specific ionisation losses as described in section 5.3.1. It takes values on the range $[0, \infty)$. The two are equivalent and can be converted to each other.

2.2 Quantum Field Theory

All modern theories that we use to describe the behaviour of particles at sub-atomic scales are of a type called Quantum Field Theories (QFTs). They describe the world as consisting of a number of fields. Particles are the quantised excitations of these fields. Interactions are described as local interactions of the fields with themselves or each other.

The structure of a QFT can be expressed in a single equation, called the Lagrangian, which sets all possible interactions and thus all possible physics. The Lagrangian is expressed as a special relativistic scalar. This ensures Lorentz invariance and makes all interactions local. In order to make statements about experiments, advanced mathematics is required in order to turn the Lagrangian into interaction rules for particles. One such set of rules are the Feynman rules that make it possible to make a perturbative expansion of an interaction around the vacuum state. Using this and other tools, such as renormalisation, interaction cross-sections for, say, electron-positron collisions can be calculated.

One aspect of QFTs that make them be considered mathematically beautiful, is that various mathematical constraints, such as self-consistency and renormalisability, severely limit the number of possible interactions. Further, as it turns out, the majority of all interactions that are mathematically possible, are in fact realised in nature. Thus according to QFT the world we live in is the only possible world, up to a number of free parameters, like particle masses and interaction strengths. This fact, together with experimental successes, is the beauty of QFTs that make them a popular candidate for a possible theory of everything.

2.3 The Standard Model

Our current understanding of the world of particle physics is summed up in the collection of QFTs that are collectively called the Standard Model of Particle Physics (SM). The SM is thus not a single theory that can easily be overthrown as additions, such as the recent discovery of neutrino masses, can be added, extending the meaning of the name ‘the Standard Model’.

The SM consists of two separate theories, Electroweak Theory (EW) and Quantum Chromo Dynamics (QCD). Each will be introduced in some more detail in the following sections. The EW part is a unified QFT description of the electromagnetic and the weak force. QCD describes the force that holds quarks bound inside protons and neutrons and also in turn binds these into nuclei.

The SM is very successful in as far as all its parts unite into a self-consistent theory. All experiments to date, of the kind where the SM is applicable, confirm the theory time and time again even as the energy frontier is being pushed further and further away from the region for which the SM was first constructed. With the recent discovery of a candidate for the higgs particle [12, 13] the SM has once again proven its worth as a good description of nature at sub-atomic scales.

2.4 Electroweak Theory

Electromagnetism is the force that acts between all particles that carry electrical charge. It is transmitted by a single massless boson, called the photon (symbol γ). Free charges can only be integer multiples of the electron charge (abbreviated e), although fractional charges of $1/3e$ and $2/3e$ are observed in the quark sector. Electromagnetism is the part of the SM that is most easily observed and studied. It was first described as the unification of electricity and magnetism by Maxwell in 1862. It was also the first part of the SM to be cast into a QFT.

The weak nuclear force is the one that is responsible for nuclear beta-decays and interactions of neutrinos with matter. The weak force is special in that it is the only force of the SM that is able to change particles from one species into another (within certain restrictions). It is also the only force that is transmitted by massive bosons. These boson masses restrict the force to act over very small distances and make it appear weak in all interactions where the total energy is less than the boson mass scale. All known particles carry weak charge and can interact via this force.

The first successful description of the weak force was in its unification with electromagnetism in 1964, a discovery for which Sheldon Glashow, Abdus Salam and Steven Weinberg shared the 1979 Nobel Prize. This unified description predicted five bosons, one of which is the photon of electromag-

netism. The other four, the Z^0 , the W^+ and W^- and the higgs boson have all subsequently been found. They are presented in table 2.2.

The structure of EW theory forbids an intrinsic mass term for any particle, a problem which was remedied with the introduction of a new field, called the higgs field. Couplings of all particles to the non-zero vacuum value of this new field lead to the apparent masses that we observe. The prediction of at least one higgs boson is a consequence of this mechanism. In spite of the recent discovery of a matching boson [12, 13], the mechanism is not yet generally considered as accepted and all mentions of the higgs boson in this thesis should thus be treated with caution.

2.5 Quantum Chromo Dynamics

Quantum Chromo Dynamics (QCD) is the theory of the internal structure of protons, neutrons and other hadrons. The force of QCD is also called the strong force due to its confining nature.

QCD describes protons and neutrons to be made up of quarks, elementary particles that carry fractional electric charge and also carry a colour charge, the charge of QCD. Colour charge has three possible values, red, green, and blue and the corresponding anti-charges, anti-red, anti-green, and anti-blue. Quarks are colour singlets, they carry a single colour charge. Anti-quarks carry anti-colour. The force between quarks is carried by a massless boson, called the gluon. Gluons are colour octets, they carry a combination of a colour and an anti-colour. In an interaction where a quark absorbs or emits a gluon the colour of the quark is changed, and the difference between the two states is carried by the gluon involved in the interaction. Thus colour continuously flows within any system that contains colour. Systems of this kind that carry colour charges on the inside are collectively referred to as hadrons.

The interactions of colour charges are distinctly different from interactions of other kinds because of the property of QCD that is called asymptotic freedom. This means that at high energies, above Λ_{QCD} , colour charges are asymptotically free and non-interacting, while they are confined at lower energies. For experiments, this means that only colour-neutral or ‘white’ objects can ever be observed in detectors. A colour-neutral state can be achieved as the combination of three coloured quarks (or anti-quarks) or the combination of one quark with an anti-quark. Combinations of three quarks are called baryons while quark-anti-quark states are termed mesons. The conservation of quark-numbers means that baryon-number is conserved in all processes if baryons are assigned a value of +1 while anti-baryons carry -1.

When describing QCD processes at colliders, one generally views the process as being split into a hard and a soft part. The hard part is the in-

teraction between particles that originate from the two different beam and have large initial relative momentum. Due to the asymptotic freedom of QCD this process can be calculated using perturbative calculations. The processes before and after this part are soft and confining and can therefore not be described perturbatively. The soft processes leading up to and following a hard interaction are generally viewed as independent of the actual hard process. Before a hard process, the colliding partons have to be selected from the incoming hadrons. This process is described by parton distribution functions which are described more closely in section 4.3. The evolution of coloured particles that are the products of a hard collision is called hadronisation.

2.5.1 Hadronisation

The evolution of coloured systems can not be described mathematically using the bare equations of QCD. The perturbative equations that are valid for hard QCD processes diverge as the momentum exchanged in an interaction decreases. . The experimental consequence of this is that the coloured products of a hard interaction that are initially free, become bound in colour-neutral hadrons before they emerge from the interaction region. The process is called hadronisation. The non-observability of colour charges is called colour confinement.

A number of phenomenological models exist that describe the process of hadronisation. One of the key criteria of such models is that they should be able to explain the observed structure of the jets of hadrons that are observed in hadronic interactions. One such model is the Lund String Model [14] which is implemented in the program PYTHIA [15]. The Lund model describes the colour field between two receding charges as a tube of with constant energy density per unit length. This tube can break to produce new pairs of quarks and anti-quarks with intermediate momenta to the primary quarks. The jets created by PYTHIA have been confirmed to behave very similar to real jets [16]. On top of this, PYTHIA is tuned to the observed jet structure at the LHC (e.g. [17]).

2.6 Particle Content

The SM contains twelve spin-1/2 matter particle, and five unit-spin force carrying particles. Half spin particles are called fermions, unit spin particles are called bosons. The fermions are shown in table 2.1. They are divided into three generations or families, shown as rows here. Corresponding particles in each generation differ only by their mass and have the same charges and relative interactions within their generation, although the difference in mass strongly affects the decay rates, lifetimes and allowed decay channels. All but the neutrinos interact through the electromagnetic force, and carry

Generation	Leptons		Quarks	
1	e (511 keV)	ν_e (<2 eV)	u (up) (~ 2 MeV)	d (down) (~ 5 MeV)
2	μ (106 MeV)	ν_μ (<0.19 MeV)	c (charm) 1.27 GeV	s (strange) (~ 104 MeV)
3	τ (1777 MeV)	ν_τ (<18.2 MeV)	t (top) (171 GeV)	b (bottom) (4.2 GeV)
EM charge	= -e	0	$+\frac{2}{3}e$	$-\frac{1}{3}e$
weak charge	: yes	yes	yes	yes
colour charge	: no	no	yes	yes

Table 2.1: This table shows all matter particles currently known to exist. The mass is shown in parentheses. Not shown are the anti-particles which have identical mass and opposite charges. All matter is made up of these particles and their interactions.

Name	Mass	Description
Z_0	91.19 GeV	EW boson
$W^{+/-}$	80.39 GeV	EW, responsible for β -decay
γ (photon)	0	light, carrier of electric and magnetic force
H (higgs)	125.5 GeV	breaks EW symmetry and gives mass
g (gluon)	0	carrier of the strong force, QCD

Table 2.2: This table shows all force carrying particles currently known to exist.

electric charge. Only quarks carry colour charges and interact through the strong force which binds them into hadrons. The weak force affects all particles and is the only force that can couple different leptons or quarks to each other. Ascribing a lepton number of 1 to all leptons and -1 to all anti-leptons, total lepton-number is always conserved in all known processes. Similarly quark-number is also conserved where quarks have a value of 1 and anti-quarks a value of -1. Anti-particles are denoted by adding a bar above the particles symbol, or by stating the charge in the case of leptons.

The five bosons in the SM are summarised in table 2.2. They are the carriers of the forces. All QFTs are local theories, meaning that all interactions are restricted to occur in a single spacetime coordinate at a time. All interactions between particles that do not directly couple to each other are mediated by bosons. Other than the restrictions of charge conservation, boson numbers are not conserved.

2.7 Stable and Meta-Stable Particles in the SM

The ordinary matter that surrounds us is made up exclusively of fermions from the first generation, namely electrons, *up*-quarks and *down*-quarks.

Name	mass in MeV	charge	composition	lifetime	decay length at 10 GeV
gamma (γ)	0	0	elementary	stable	∞
electron (e)	0.511	-1	elementary	stable	∞
proton (p)	938.3	+1	uud	stable	∞
neutron (n)	939.6	0	udd	881.5 s	2.8×10^{12} m
pion (π^+)	139.6	+1	$u\bar{d}$	26 ns	558 m
muon (μ)	105.7	-1	elementary	2.20 μ s	62.4 km
kaon (K^+)	493.7	+1	$u\bar{s}$	12.4 ns	75.2 m
K-long (K_L^0)	497.6	0	$\frac{d\bar{s}+s\bar{d}}{\sqrt{2}}$	51.2 ns	308 m
deuteron	1876	+1	pn	stable	∞

Table 2.3: *Particles that appear as stable products at collisions at the LHC. Notice that the largest distance of an ATLAS sub-detector from the interaction point is about 25 m, the closest distance of the calorimeters to the collisions is about 1.5 m. In this analysis particles down to 5 GeV were used, so 10 GeV is a representative particle energy. All of these particles can be detected directly by ATLAS before they decay. Anti-partners are not listed separately.*

These are the only elementary particles that are entirely stable. Neutrons are made up of one *up* and two *down* quarks, while protons consist of two *up* and one *down*. Together with electrons they make up the building blocks of atoms, and are thus all that we normally see.

In collider experiments, like ATLAS, the situation is slightly different however. In the high energy interactions created by the LHC, all possible particles are created at some time or other, some more frequently, others very rarely. Since most particles have a rest mass that is considerably below the energy that they are created with, they are moving very quickly, usually at relativistic speeds. Because of the high speed and the associated relativistic time dilation, many of the particles that would ordinarily be called short lived, appear quite stable from the point of view of the experiment. This is because their lifetimes are long enough that they are able to pass through the detector elements before decaying, and can thus be detected directly. The particles that are viewed as stable from the point of view of the ATLAS experiment are listed in table 2.3. Not mentioned in this table are the neutrinos. They cannot be detected by ATLAS due to their weak interactions with matter.

The discovery of the kaon and the muon were historically important to the development of the SM, the kaon being the first particle with ‘strangeness’ to be discovered. They are of particular illustrative value to this analysis though, as they have several of the features that we are looking for in this analysis. This will be explained further in section 3.1.2.

The stable particles of the SM are useful in this analysis for calibration purposes. They are also the source of the background though, as a mismeas-

ured timing or ionisation can make, say, and energetic muon appear quite massive.

2.8 Beyond the Standard Model

The standard model is an extremely successful theory. Most of its predictions are confirmed experimentally, some with very high precision. The most famous example of this is the prediction of the anomalous magnetic dipole moment of the electron where both the theoretical prediction [18] and the experimental value [19] are both precise to better than a part per trillion and agree within 0.26σ .

With the recent discovery of a candidate for the higgs boson the SM stands unchallenged in its description of all processes that can be reduced to non-gravitational interactions between known particles and describes all known processes within these limitations. Nevertheless we know that the SM can not be a fundamental theory of everything because of a number of shortcomings contained in it. In the following, we will outline a few problems that the SM in its current form is unable to solve.

2.8.1 Gravity

There exists today a very good theory of gravity, called General Relativity (GR). It relates the effects of gravity to the curvature of 4-dimensional spacetime. GR is used to describe the evolution of gravitational systems such as the formation of galaxies and the history of the cosmos as a whole since the Big Bang. GR stands as unchallenged in its description of these phenomena as the SM does in particle physics. Nevertheless, the two seem inconsolable on a mathematical level. Any attempt to cast GR in a QFT framework leads to non-renormalisable divergencies preventing a unified description of the two theories. Although experimentally inaccessible to us, we know there exists a scale, called the Plank-scale, at which the effects of both theories must be equally visible. From this we can conclude that the dissonances between the two theories are merely the consequence of our limited understanding, and not an inherent conflict between the phenomena. As long as this problem of unification exists between the SM and GR, neither can be regarded as a fundamental theory of everything.

The inaccessibility of scales at which both theories are active is frequently cited as one of the main reasons for the lack of progress in unifying SM with GR. As an example of how difficult it is to study gravitational effects in particle systems one can look at antimatter. First discovered by in 1933 by Anderson [20] some 80 years ago, there exists as of today no evidence that anti-matter has the same gravitational attraction as matter, even though there is wide consensus that it should. First now, the experiment AEGIS [21] has been proposed at CERN to measure this effect.

2.8.2 Dark Matter

We know today from observations of galactic rotation curves as well as simulations of cosmic scale formation since the Big Bang that there exists about a factor of 5 more matter in the universe than can be seen in the form of atoms and particles, what astrophysicists call baryonic matter. The remaining matter content of the universe is termed Dark Matter (DM), pertaining to its mysterious nature. Not much is known about DM except that it does not interact more than weakly with either itself or with baryonic matter. It also cannot consist of neutrinos since their known low mass would make neutrino DM too hot to be bound in the structures where we see DM today. DM is therefore a true mystery of 21st century physics that must be answered by any theory with aspirations of being considered fundamental or universal.

2.8.3 The Hierarchy Problem

There are a number of internal consistency issues within the SM itself, as an example, I will here mention the hierarchy problem. This name has been given to the unexplained discrepancy between the scale of EW symmetry breaking ($\mathcal{O}(10^2 \text{ GeV})$), the highest scale in the SM, and the Planck scale.

The Planck scale is the scale (in space or energy) where gravitational effects need to take on a quantum aspect. It is universally agreed among physicists that a suitable description of phenomena at this scale must be a true description of quantum gravity. The magnitude of the Planck scale is about 10^{19} GeV .

Within the SM, the hierarchy problem becomes more concrete when considering loop corrections to the higgs mass. In order to fulfil its role in EW symmetry breaking, the mass of the higgs needs to be not too different from the mass at which a suitable candidate has recently been found (126 GeV). When calculating the mass of the higgs from theory, including loop corrections, one finds the following, however.

Because it is predicted to be a true scalar, the higgs is not protected from the type of process shown in figure 2.1. In these processes the higgs radiates and reabsorbs a virtual particle. The momentum of the virtual particle needs to be integrated over in the calculation of the diagram's contribution. This calculation yields for each fermion a correction to the higgs mass of

$$\Delta m_H^2 = -\frac{|\lambda_f|^2}{8\pi^2} [\Lambda_{UV}^2 + \dots] \quad (2.5)$$

where λ_f is the coupling strength of the fermion to the higgs field and Λ_{UV} is the scale to which the momentum integral is evaluated. The contribution of bosons has the same form but an opposite sign.

Hence we see that in the absence of any natural limiting scale below the Planck scale, the mass corrections to the higgs mass would be $\mathcal{O}(m_{\text{Planck}})$.

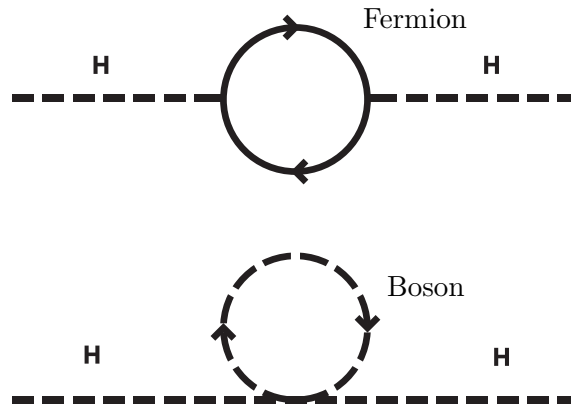


Figure 2.1: *The higgs free propagator is not protected from picking up arbitrarily large mass corrections from fermion or boson loops like this.*

The only way this can be avoided within the SM is to fine-tune the contributions of the SM bosons to be of equal magnitude as the fermionic contribution so that the two can cancel out. This in itself is called the fine tuning problem and is generally not regarded as a solution to the hierarchy problem.

A possible solution to this problem is given by Supersymmetry as presented in section 2.8.6.

2.8.4 Dark Energy

Another experimental challenge to the SM which should be noted for completeness' sake is the existence of Dark Energy. This mysterious quantity has been discovered by astronomers in the study of the cosmological expansion history of the universe. From observations of distant galaxies, we can see that the expansion of the universe, which might be assumed to be slowing down since the Big Bang due to gravity, is actually accelerating. This acceleration is assumed to be driven by a universal pressure that is equivalent to a constant energy density in all of space. This energy density is called 'Dark Energy' or 'the cosmological constant'. It has the unusual property that it maintains its density while space is expanding and is not diluted as would be expected from any ordinary energy, such as, for example, a photon

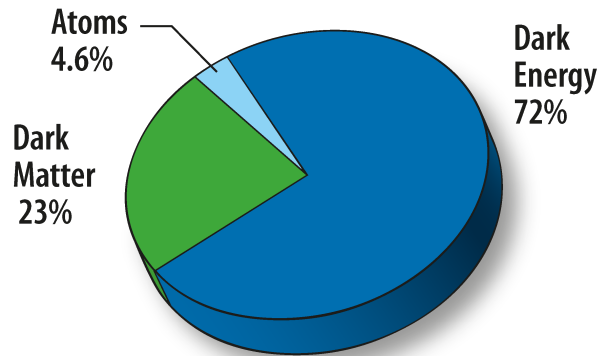


Figure 2.2: *The present energy content of the universe as obtained from cosmological models.*

gas. Figure 2.2 shows that current estimate of the composition of the energy density of the universe.

Dark Energy stands on a much less solid experimental basis than DM as the prediction of its existence is more model dependent than that of DM. Partly due to this and partly due to the strange non-diluting properties, there are currently no good models for physics beyond the SM that attempt to address the issue. Nevertheless, the phenomenon should be explainable in any fundamental theory of everything.

2.8.5 Models Beyond the SM

There exists today a plethora of models for physics beyond the standard model (BSM) that stem from a range of approaches. Given the consistency of available data with the SM, some efforts for BSM theories are guided by trying to bridge the gap between particle physics and other branches of fundamental theory, in particular astronomy and cosmology, others are motivated primarily by considerations of possible mathematical structures.

In general many approaches are based on an extending the symmetries, dimensions and/or particle content of the SM. Thus, for example, Technicolor adds a new $SU(3)$ group that gives compositeness to particles today thought of as fundamental. The most popular and well studied model for new physics is called Super Symmetry (SUSY), which proposes a new symmetry between bosons and fermions in the SM.

From an experimentalists point of view one common requirement to BSM models is that they need to be mathematical, and that they need to allow the calculation of new signatures, such as new resonances or modified cross-sections or angular distributions. This excludes some more esoteric approaches, such as string-theory, from being studied at high energy physics experiments. This requirement for calculable predictions comes from the

fact that virtually all physics analyses today rely on Monte Carlo simulation methods to compare real experimental results with simulated results. From this, conclusions are then drawn about the similarity between the physical reality that controls the collisions and the theory that goes into the MC calculations.

2.8.6 Supersymmetry

Supersymmetry (SUSY) is a symmetry between bosons and fermions. Mathematically it is one of the few ways of directly permitted ways extending the SM Lagrangian.

On the phenomenological side SUSY would mean that there exists a super-partner particle for every boson and fermion with the same mass and quantum numbers. Since the SM bosons and fermions display no such pairing behaviour, imposing SUSY requires at least a doubling of the number of SM particles. New bosons that are the SUSY partners of SM fermions are named by prefixing an ‘s’ to their partners name. Collectively they are referred to as sfermions. New fermions that are the SUSY partners of SM bosons are named by appending ‘-ino’ to the SM bosons name. Thus, the supersymmetric partner of a gluon would be called a gluino. The single letter symbols for SUSY particles are the symbol of their SM partner with a tilde added above them (e.g. \tilde{g} for gluino).

SUSY has a number of attractive features. It provides an elegant solution to the hierarchy problem by cancelling the contribution of each SM particle with the equally large, but oppositely signed contribution of the SUSY partner particle. In fact it was for this purpose that the Minimal Supersymmetric Standard Model (MSSM) as first proposed [22].

Experimentally SUSY partners have not been observed at the same masses as the SM particles, SUSY is therefore assumed to be a broken symmetry, should it exist. This means that the SUSY particles have masses considerably higher than their SM partners. The several different mechanism of this breaking can be postulated leading to different models with different phenomenologies. Examples of such models are listed in table 3.1. The breaking usually originates in a much higher lying sector of the model, which is far out of experimental reach, and is communicated down to the SUSY scale by one or several messenger particles.

One aspect of SUSY that cause problems initially is that when including all possible interactions, SUSY no longer naturally conserves baryon and lepton number separately. This allows, amongst other things, the proton to decay. The experimental limits on proton stability are very stringent with lower limits on the lifetime of over 6×10^{33} years at 90 % confidence [23]. This made it necessary to introduce a new conserved property, called R -parity defined as

$$P_R = (-1)^{2s+3B+L} \tag{2.6}$$

where B is baryon number, L is lepton number and s is spin. All SM particles have $P_R = 1$ while super-partners have $P_R = -1$.

The introduction of R -parity means that SUSY particles can only be produced in pairs, and that the lightest supersymmetric particle (LSP) must be stable since its decay would violate R -parity conservation. This last observation was welcomed when it was realised that the LSP would be a good candidate for DM, provided that it was neutral and only weakly interacting.

The LSP as a DM candidate together with the possible solution to the hierarchy problem are the core motivations behind the development of SUSY as a model for BSM physics.

Chapter 3

Stable Massive Particle Theory

3.1 Motivation

As explained in section 2.8 there is a need for new models that extend the theoretical reach beyond the Standard Model. One recurring theme of such new models is the existence of new types of particles that may be stable or at least long lived on the scale of a detector with

$$c\tau \sim \mathcal{O}(\text{m}) \tag{3.1}$$

where τ is the proper lifetime of the particle. Our search focused on new particles that are heavy and are therefore referred to as stable massive particles (SMP). An excellent overview of various models that predict the existence of SMPs can be found in [24]. A general justification for the possible existence of SMPs can be given both on theoretical and experimental grounds as outlined in the following sections.

3.1.1 Theoretical Motivation

Many proposed models for physics beyond the SM attempt to bridge the gap to other disciplines by including a particle as a candidate for dark matter (DM), a clearly missing part of the SM described in section 2.8. Usually a DM candidate takes the form of a heavy neutral stable particle. The stability of these particles is usually ensured by a new conserved quantum number X . These models usually introduce whole families of new particles that all carry X and that can decay to each other. The lightest particle of this family cannot shed its X through further decay and is therefore stable. A prominent theory that has this feature is supersymmetry (SUSY) where the new quantum number is called R -parity, under which all SM particles have $R = 1$ and all new SUSY particles have $R = -1$. In all following

discussions we will use R -parity although the arguments apply equally well to the conserved parities of other possible new models.

The lightest $R = -1$ particle, also called the lightest supersymmetric particle (LSP), can be a DM candidate. In order to fulfil this role, the LSP can at most couple weakly to all SM particles and itself. This is due to experimental constraints in astronomical and direct DM searches. It must therefore be neutral and colourless. The next-to-lightest supersymmetric particle (NLSP) (or second lightest X -charged particle in other models) however does not have this constraint and can carry both electric charge and/or colour charge. In general the NLSP would be expected to quickly decay to the LSP, but in some cases, if the mass splitting is too narrow or the phase-space is otherwise constrained, the NLSP can obtain a very long lifetime and might be directly observable. In other scenarios, R -parity may be only nearly conserved, meaning that the LSP can decay. In this scenario, charged LSPs are no longer constrained from cosmology and thus the LSP itself may be observed as a charged metastable particle in collider searches.

With the continued absence of any direct evidence for SUSY, the search for SMPs becomes ever more important. The SUSY parameter space is by now very constrained by observation, threatening its “naturalness”. One way of sidestepping these constraints is if there exist one or several stable massive particles, which conventional collider searches are not sensitive to.

Supersymmetry without prejudice

A large effort to describe the phenomenology of the remaining allowed supersymmetric models was published under the name “Supersymmetry without prejudice at the LHC” [25]. This study was carried out by generating a large number of supersymmetric (SUSY) models by randomly choosing sets of SUSY parameters and afterwards checking if the model generated by this set is allowed by current experimental bounds. Disallowed models were rejected, leaving only models that are still allowed by current experimental bounds. The parameters of all models were chosen from a flat prior giving rise to the title ‘without prejudice’. The analysis of common features of the remaining $\sim 70\text{k}$ models showed that one common feature that allowed the models to evade exclusion was to predict long-lived massive charged particles. The non-decay of such particles makes them fall below and outside the signal region of many regular jet- and cascade-based searches. This finding alone provides a large incentive to launch searches for long-lived heavy particles as an orthogonal approach to ordinary resonance searches in the hunt for SUSY.

Model Overview

The SMP overview paper [24] contains a good overview table over various SUSY scenarios that predict the existence of some kind of SMP. The table is reproduced as table 3.1. All models in this table are SUSY models. They differ in the way that the supersymmetry is broken.

MSSM is the Minimal Supersymmetric Standard Model. SUSY breaking is soft and originates in an unspecified sector [22]

GMSB, a version of the MSSM, is Gauge Mediated SUSY Breaking where SUSY is broken in an inaccessible sector and this breaking is communicated down to SUSY scales by gauginos [26,27]

\tilde{g} MSB is like GMSB except the messenger particle is a gluino.

SUGRA stands for Supergravity. The breaking is mediated to the MSSM via supergravity.

AMSB (Anomaly Mediated SUSY Breaking) is a special type of gravity mediated SUSY breaking [28,29]

All these models predict the existence of SMPs of which some carry electric charge ($\tilde{\tau}_1, \tilde{\ell}_{i1}, \tilde{\chi}_1^+$), some carry colour charge (\tilde{g}), and some both (\tilde{t}_1, \tilde{b}_1).

3.1.2 Experimental Motivation

There are ways to justify the search for SMPs on experimental basis alone. Discoveries of new particles with surprisingly long lifetimes are a recurring theme in experimental physics. Examples of such particles are the muon and the kaon. The muon is long lived because its decay can only proceed via an intermediary heavy W -boson. Such a situation can well arise in a new theory if the mass difference between the NLSP and the LSP is much less than the mass of the boson mediating the decay.

In the case of kaons we also find many of the features that can be expected for new SMPs. Kaons carry a quantum number that was unknown until their discovery, namely strangeness. Strangeness is approximately conserved, which is why kaons can easily be produced in pairs, but decay quite slowly. The discovery of kaons played an important role in the development of the quark model of hadrons.

Because of such general considerations, both theoretical and experimental, it can be argued that the search for long lived particles is one of the most essential approaches in the quest for new unexpected physics.

SMP	LSP	Scenario	Conditions
$\tilde{\tau}_1$	$\tilde{\chi}_1^0$	MSSM	$\tilde{\tau}_1$ mass (determined by $m_{\tilde{\tau}_{L,R}}^2$, μ , $\tan\beta$, and A_τ) close to $\tilde{\chi}_1^0$ mass.
	\tilde{G}	GMSB	Large N , small M , and/or large $\tan\beta$
		\tilde{g} MSB	No detailed phenomenology studies, see [30].
		SUGRA	Supergravity with a gravitino LSP, see [31].
	$\tilde{\tau}_1$	MSSM	small $m_{\tilde{\tau}_{L,R}}$ and/or large $\tan\beta$ and/or very large A_τ .
		AMSB	Small m_0 , large $\tan\beta$
\tilde{g} MSB		Generic in minimal models.	
$\tilde{\ell}_{i1}$	\tilde{G}	GMSB	$\tilde{\tau}_1$ NLSP (see above). \tilde{e}_1 and $\tilde{\mu}_1$ co-NLSP and also SMP for small $\tan\beta$ and μ .
	$\tilde{\tau}_1$	\tilde{g} MSB	\tilde{e}_1 and $\tilde{\mu}_1$ co-LSP and also SMP when stau mixing small.
$\tilde{\chi}_1^+$	$\tilde{\chi}_1^0$	MSSM	$m_{\tilde{\chi}_1^+} - m_{\tilde{\chi}_1^0} \lesssim m_{\pi^+}$. Very large $M_{1,2} \gtrsim 2\text{TeV} \gg \mu $ (Higgsino region) or non-universal gaugino masses $M_1 \gtrsim 4M_2$, with the latter condition relaxed to $M_1 \gtrsim M_2$ for $M_2 \ll \mu $. Natural O-II models, where simultaneously also the \tilde{g} can be long-lived near $\delta_{\text{GS}} = -3$.
		AMSB	$M_1 > M_2$ natural. m_0 not too small. See MSSM above.
\tilde{g}	$\tilde{\chi}_1^0$	MSSM	Very large $m_{\tilde{q}}^2 \gg M_3$, e.g. split SUSY.
	\tilde{G}	GMSB	SUSY GUT extensions [32–34]
	\tilde{g}	MSSM	Very small $M_3 \ll M_{1,2}$, O-II models near $\delta_{\text{GS}} = -3$.
		GMSB	SUSY GUT extensions [32–36]
\tilde{t}_1	$\tilde{\chi}_1^0$	MSSM	Non-universal squark and gaugino masses. Small $m_{\tilde{q}}^2$ and M_3 , small $\tan\beta$, large A_t .
\tilde{b}_1			Small $m_{\tilde{q}}^2$ and M_3 , large $\tan\beta$ and/or large $A_b \gg A_t$.

Table 3.1: Brief overview of possible SUSY SMP states considered in the literature. Classified by SMP, LSP, scenario, and typical conditions for this case to materialise in the given scenario. Table from [24].

3.2 Production and Decay

3.2.1 Production

SMPs are generally thought to be pair produced at colliders ([24]) in a process like

$$ab \rightarrow X_c X_d \quad (3.2)$$

where a and b are partons of the incoming beams and the X particles carry a new quantum number. The production cross-section of such a process may be quite large even while the decay of the X can be suppressed by the conservation or near conservation of X . This may make the production of X particles a very prominent feature at the LHC where the centre of mass energy may for the first time be sufficient for the process to occur.

If X is not conserved single production may also be possible as

$$ab \rightarrow X. \quad (3.3)$$

If this process is allowed however, the reverse is also allowed as a decay channel where the strength of the decay is coupled to the production cross section. In order to obtain a long enough lifetime for X to be observable as an SMP from this channel, the production cross section needs to be so low as to make the process essentially never occur at the LHC. Hence pair production via the process 3.2 is the only viable production mechanism for SMPs.

In order to estimate the production cross section of these new states at the LHC, one can calculate the matrix element of the process 3.2 and fold it with the parton distribution functions for a and b . From this all relevant differential cross sections and distributions can be obtained.

The pair production cross section of coloured states can proceed via strong interactions. They can be produced by either gluon-gluon (gg) or fermion-antifermion ($f\bar{f}$) collisions. Charged, colour neutral states however rely on EW production via $f\bar{f}$ only. The relative cross sections of these two types of particles therefore differ by a factor of $(\alpha_s/\alpha_{(EW)})^2$ in the $f\bar{f}$ channel alone. Hence coloured states would be produced in much greater number should they exist [24].

3.2.2 Decay

Our search was motivated by stable as well as meta-stable particle signatures. All particles that are not absolutely stable will decay at some point. The precise phenomenology of that decay is very much dependent on the nature of the SMP. We tried to keep our search as much as possible independent of the theory from which the SMP arises. This is possible because of the detector interaction models that are described in section 3.4.

The signature of a decaying SMP would be a slow, highly ionising track that ends before the end of the detector. Possibilities for what happens next range from simple disappearance to the production of powerful showers, depending on whether the SMP decays to a DM candidate with a small mass difference or whether an R -parity non-conservation leads to the entire SMP mass being turned into SM particles. Selecting candidates based on these possible end-of-track features would severely limit our model coverage. On the other hand, simply assuming that SMPs never decay inside the detector would also limit our model coverage. These considerations together with the possibility of charge-flips in R -hadrons led to the development of the following strategy:

In total we carried out several searches where each search considered a progressively larger part of the detector starting from the interaction point. A search based on the pixel detector only had already been published separately by a different group within ATLAS [4]. We extended this strategy with two more searches, one considering only the inner detector and calorimeters, the other including also the muon spectrometer. This way our discovery potential includes SMPs that decay after any distance and to any secondary particles.

3.2.3 ISR and FSR

In a pair production that has coloured particles in both the incoming and outgoing states, both initial state radiation (ISR) and final state radiation (FSR) can occur. This is the radiation of soft gluons that are more or less collinear with the emitting particles. Since the probability of FSR scales inversely with the mass of the secondaries, which in our case are very heavy, we expect to have a very low levels of FSR.

ISR however may occur at a significant rate such that the production of SMPs is often associated with jets in other regions of the detector. This is an important feature of such events because it allows us to trigger the events even when the SMPs themselves are not detected at the trigger stage.

The rate of ISR emission rises with the amount of colour charge in the initial state. It is therefore expected that gg production will lead to more jets than $f\bar{f}$ production. How these associated jets are relevant for triggering the events will be described in more detail in section 6.4

3.3 Types of Stable Massive Particles

In our analysis we used simulated signal samples of two distinct types of SMPs, R -hadrons and sleptons. Sleptons are supersymmetric lepton partners. This means that they carry a single unit of electric charge and no colour charge. R -hadrons are composite particles of a coloured SMP and several SM quarks. The two types of particles share many characteristics

but also have some distinct differences that make it necessary to tune the search criteria to get the best sensitivity for both types.

3.3.1 Sleptons

The detector interactions of a slepton are be purely electromagnetic. This makes their signature somewhat simpler than R -hadrons. However, as noted in section 3.2.1 the absence of colour charge makes their expected production cross-section considerably lower. Because of this the sleptons predicted by a range of SUSY models with masses of 300 GeV or lower are not yet excluded by previous analyses. At LHC energies SMPs of this low mass can have a large speed β which makes the use of pixel discriminators less useful. Because of this the slepton search makes use of the pairing of candidates to define a cleaner signal region.

3.3.2 R -hadrons

The name R -hadron derives historically from particles carrying the R -parity of super symmetry, but is used today to refer to a wider class of particles with the same kind. R -hadrons are composite hadronic particles consisting of a new coloured massive particle that is bound together with one or several SM quarks and/or gluons to produce a colour neutral particle. The lifetime of the new particle must at least exceed Λ_{QCD} to allow the hadronisation to occur.

The behaviour of R -hadrons is in large parts dependent on their strong interactions. These can be considered in two parts, hadronisation and detector interactions. The dynamics of the creation of the new particles in a parton level hard process (as in equation 3.2) are determined by whatever new theory that describes the SMP. The hadronisation and detector interactions however are much softer processes which can be described within the existing framework of QCD. The probability that the heavy parton interacts perturbatively is small as such a process is suppressed by the square of its inverse mass. Hence all processes and interactions are mainly the result of interactions of the SM partons. The massive parton acts primarily as a momentum source with a colour charge. Hence QCD alone can be used to model both the hadronisation process and nuclear interactions.

The detector interactions of the SMP can be divided into electromagnetic and hadronic interactions. The electromagnetic interactions of an SMP are thought to be very well understood in that they should behave the same as all other charged particles as described in section 5.3.1 [37]. The hadronic interactions however are subject to some uncertainty and various models have been proposed to describe them. They will be presented in section 3.4.

3.4 R -hadron Hadronisation and Hadronic Interactions

3.4.1 Hadronisation

As mentioned in section 3.3.2, the hadronic interactions of any R -hadron is thought to be described entirely by its QCD effects. When an coloured heavy particle emerges from its production in the interaction point it will hadronise with SM particles. The process can not be described perturbatively because it is soft. The end-point of this process depends on the stability of possible hadron states.

A coloured new particle that is a colour triplet, denoted C_3 , can form hadrons of the form $C_3\bar{q}$, C_3qq , $C_3\bar{q}$, a colour anti-triplet, denoted $C_{\bar{3}q}$, $C_{\bar{3}q}\bar{q}$, a colour octet C_8 , can form C_8qqq , C_8g , etc [37]. The energy of the hadronic system can be described by the same equations that can be used to model the energies of the lowest SM hadrons. Higher hadronic states will decay too quickly to be of importance. Modelled this way, the hadronic system contributes less than 1 GeV to the total mass of the R -hadron, the mass is thus essentially the same as that of the heavy parton.

The most important aspect of the relative stability of the various hadronic states in the context of our search is whether the resulting hadron is charged. Fairbairn et. al. [24] show that both PYTHIA [15] and HERWIG [38] predict around 55 % neutral R -hadrons following the hadronisation of a colour octet and around a 41 % neutral fraction for a stop quark (super-symmetric top). The remaining states are charged with both positive and negative single and double charges being seen. Table 3.2 shows the predicted composition of R -hadrons from the two generators.

One feature worth pointing out in table 3.2 is that the squark based R -hadron is only able to acquire positive charge. This is because of the electric charge of the squark.

3.4.2 Interactions

A good overview of R -hadron interactions is given in section 5.2 of [24]. A summary of the essential aspects is given in this section.

The detector interactions of R -hadrons can have profound effects on their observed behaviour. This is because R -hadron are able to change their identity radically by exchange of the light quark system. Such an exchange can result in a change of charge, i.e. an R -hadron is not guaranteed to remain charged throughout the detector. It can lose its charge, or even reverse the charge's sign.

Several models have been proposed to understand these nuclear interactions. One central theme that is common to them all is that the interactions involve only the light quark system. Any interaction of the heavy parton is

3.4. R-HADRON HADRONISATION AND HADRONIC INTERACTIONS 37

R -hadron	PYTHIA Fraction (%)	HERWIG Fraction (%)
$R_{g\bar{u}d}^+, R_{g\bar{d}u}^-$	34.2	28.2
$R_{g\bar{u}u}^0, R_{g\bar{d}d}^0$	34.2	28.2
$R_{g\bar{u}s}^+, R_{g\bar{s}u}^-$	9.7	17.5
$R_{g\bar{d}s}^0, R_{g\bar{s}d}^0, R_{g\bar{s}s}^0$	10.4	26.1
$R_{g\bar{g}}^0$	9.9	—
R_g^{++}, R_g^{--} (anti)baryons	0.1	—
R_g^+, R_g^- (anti)baryons	0.8	—
R_g^0 (anti)baryons	0.7	—

R -hadron	Fraction (%)
$R_{t\bar{d}}^+$	39.6
$R_{t\bar{u}}^0$	39.6
$R_{t\bar{s}}^+$	11.8
R_t^{++} baryons	0.8
R_t^+ baryons	6.7
R_t^0 baryons	1.5

Table 3.2: Predictions from PYTHIA of the fractions of different species of R -hadrons following the hadronisation of a gluino (left) and a stop (right) of mass 500 GeV produced at the LHC. The HERWIG gluino predictions are for a 2000 GeV mass, but almost identical for 50 GeV. (Taken from [24])

suppressed. Thus the heavy C_i can be seen as a spectator to the interaction and serves merely as a reservoir for kinetic energy.

When considering the interaction between the light quark system and a hadron, the interaction energies are low. As an example, a $C_8 q\bar{q}$ with a mass of the C_8 of 300 GeV and a total energy of 450 GeV will have a Lorentz factor of $\gamma = 1.5$. The kinetic energy of the quark system is the only $(1 - \gamma)m_{q\bar{q}} \sim 0.3$ GeV [37]. Thus the interactions of such a system can be seen as analogous as the known interactions of, in this case, a $q\bar{q}$ meson.

Possible iterations are shown in figure 3.1. Elastic scattering (figure 3.1(a)) contributes little to the overall energy loss because of the large difference in mass between the incoming partners. Baryon exchange (figure 3.1(b)) is thought to cause any R -hadron to acquire a baryon number as the reverse process is suppressed by phase space considerations and the low natural abundance of pions in matter. Charge exchange processes as in figure 3.1(c) can occur both for R -baryons and R -mesons. While it is difficult to make precise predictions for the relative strengths of the possible interaction modes, charge exchange may contribute significantly.

Previous publications [7] have investigated the effects of different interaction models and found no strong effect on the final limit. In our simulations we used the same interaction models as in [7].

The hadronisation and interaction model used for our search is described in [39]. According to this model $\sim 50\%$ of the coloured massive particles produced in the hard collision will hadronise to a neutral R -hadron and $\sim 75\%$ of the R -hadron will be neutral in the muon spectrometer after

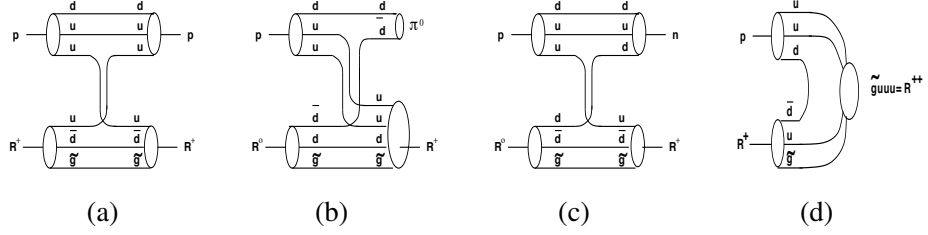


Figure 3.1: R-hadron-proton scattering processes. (a) Elastic scattering, (b) Inelastic scattering leading to baryon and charge exchange, (c) Inelastic scattering leading to charge exchange, (d) Resonance formation. Figure taken from [24]

having passed through the high mass of the calorimeters. Therefore, not all the R -hadrons can be considered as candidates in this analysis.

3.5 Cross-Section Calculations

In the search for stable massive particles, that is the theme of this thesis, we relied in some parts on the predicted behaviour of new hypothetical particles. Particularly the distributions in pseudorapidity, the expected missing transverse energy and the production channel (ff vs. gg) affect our analysis. These predictions can in some parts be justified without losing too much of the model independence that we aspire to.

When thinking about new physics, we mostly think about the hard process that governs the pair production. This is the part that depends on the new physics that may allow the creation of new SMPs for example. Such a model is also needed to generate the signal samples that we used to tune our cuts. The full expression for a differential cross section, however, depends on more than just this new matrix element. One important factor that needs to be folded into a cross section expression is the availability of contribution partons in the incoming protons as a function of their fraction of the full proton momentum, the so-called Parton Distribution Functions (PDFs). While the matrix element is important with respect to the absolute cross section, the PDFs have a strong influence on the η distribution of the resulting particles.

Because PDFs are independent of the nature or strength of the hard interaction, the prediction of the way the SMPs are distributed in the detector can be seen as independent of the model that was used to simulate their generation.

This fact, together with the model independent interaction models we used makes our search applicable to a wide range of theories that predict the existence of SMPs.

Chapter 4

The CERN Accelerator Complex

The particle physics laboratory CERN, located on the Franco-Swiss border is host to a collection of accelerator based high energy physics experiments the best known of which are the Large Hadron Collider (LHC) [40] and the experiments based around it. The LHC is a proton-proton collider. It was designed for a collision centre of mass energy of 14 TeV, but in practice it was run at a per-beam energy of 3 TeV in 2011 and is currently running with 4 TeV per beam for 2012. These lower energies are less demanding on the machine and are used as precautionary measures after a failure of the magnet system in 2009.

The task of the LHC accelerator is to bring protons at high energies into collision at four interaction points, each of which is surrounded by a detector. At these unprecedented high collision energies new physical phenomena reveal themselves and can thus be studied.

4.1 The Accelerators

As a rough overview, the working principle of the accelerators can be described as follows: Protons are collected from ionised hydrogen in bunches with fairly low spacial extent ($\mathcal{O}(\text{cm})$) which are accelerated by sending them through long series of electric cavities. The cavities are fed with a high frequency high voltage signal which is designed such that the alternating fields in the various parts of the cavity always align to push and accelerate the charged protons. The frequency that the cavities are fed with is 400 MHz and lies in the radio band. Therefore the driving signal is often referred to as the radio frequency (RF) signal, and the cavities are called RF-cavities.

Systems of multipole magnets are employed to keep the bunches together in the transverse directions and focus them onto the beam axis. Figure 4.1 shows how quadrupole magnets are arranged in series in order to focus the

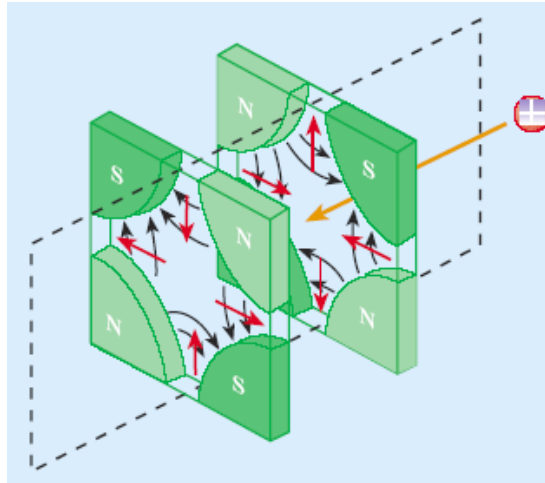


Figure 4.1: *The effect of a quadrupole focussing cell on a charged beam. The beam path is shown in orange, magnetic field lines are black and the effective force on the beam is drawn in red.*

charged beams.

Finally, dipole magnets are used to bend the beam on circular paths and return it to the acceleration cavities. In the LHC there are two beams, one going in each direction. The two beams need opposite magnetic fields and are therefore kept in separate beam-pipes. Figure 4.2 shows the arrangements of the fields in an LHC dipole magnet.

The dynamics of the beam in magnetic and electric fields dictate that the physical dimensions of the accelerator be matched to the beam energy. It is therefore most practical to accelerate the protons from rest in several stages in separate accelerators, each matched to successive ranges of energies. The beams are transferred between the accelerators via transmission lines. At CERN, this has led to the development of a whole series of different accelerators. Where each one started out as an experiment in its own right and ended up as pre-acceleration stage to the next one. A schematic layout of the accelerators at CERN is shown in figure 4.3.

The counterrotating beams are crossed in four interaction points. A very small crossing angle means that the beams collide virtually head-on. The non-zero crossing angle is usually neglected in the analyses. The size of the individual bunches within a beam is dictated by the RF-signal. A part of the beam that can potentially hold a bunch of protons is referred to as a bucket. At the LHC each beam has a total of 2808 bunches. Giving a minimal bunch-spacing of 25 ns and a maximal bunch-crossing rate of 40 MHz. In practice not all buckets are filled, and so far (until 2012) the LHC has not been run with a bunch spacing of less than 50 ns. This was chosen to give the detectors more recovery and processing time after each collision.

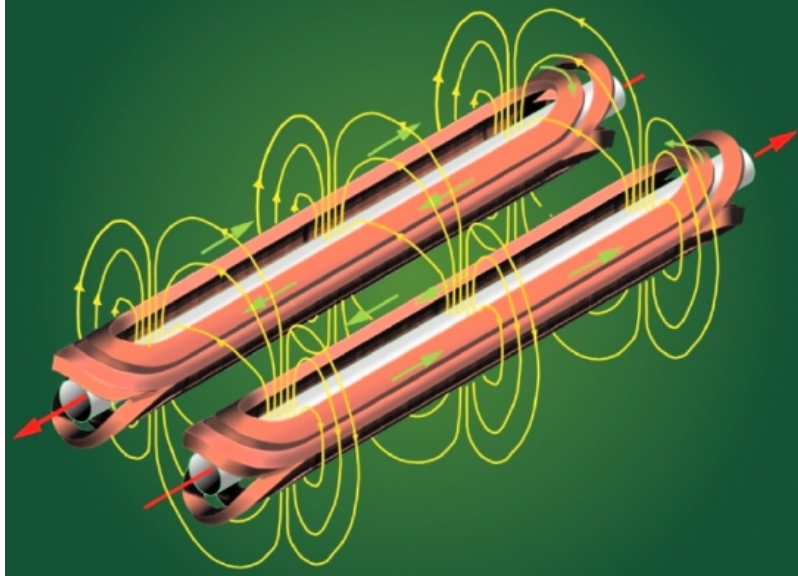


Figure 4.2: The arrangement of the dipole fields in the LHC magnets is shown. Two counterrotating proton beams need opposite fields [41].

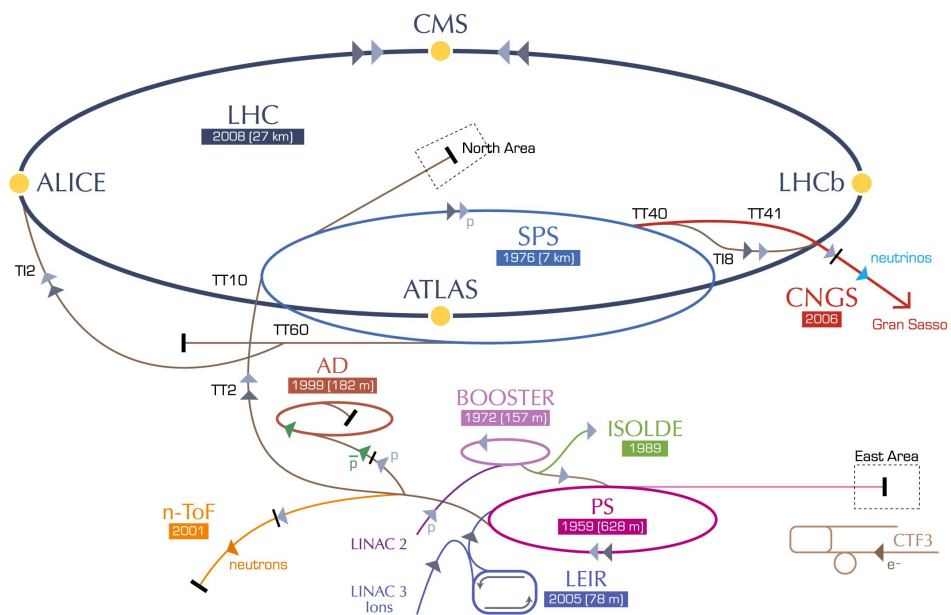


Figure 4.3: The layout of the CERN accelerator complex [42].

During normal operation, bunches are produced by the LINAC, and subsequently accelerated in stages in the BOOSTER, the Proton Synchrotron (PS) and the Super Proton Synchrotron (SPS) up to a total LHC injection energy of 450 GeV. The LHC is filled in steps, bucket by bucket, until the desired number of buckets have been filled. Injection then stops and the beams are accelerated while the magnet current is increased to keep the beams in the ring. Once the beams have reached full energy and are declared stable, they are brought into collision by adjustments of the focusing magnets around the experiments. The whole process including ramp-down of the magnets from a previous fill gives a turn around time between fills of minimum 70 min [40]. The collision rate is highest at the start of a run and then falls roughly exponentially as the bunches slowly disperse through coulomb interactions during collisions. The loss of protons from the bunches due to the collisions themselves is negligible. When the interaction rate has fallen far enough to make it more worthwhile to refill than to keep running, the beams are dumped in tangential beam-dump tunnels near the CMS experiment. At the beam-dump, the beams are dispersed by powerful magnets so as not to overheat the beam dump absorber.

4.2 The Detectors

The four interaction points are each surrounded by a detector. They are called ATLAS, Alice, CMS and LHCb. Their location is shown in the schematic in figure 4.3. ATLAS and CMS are large general purpose detectors that are designed to discover new physics by detecting all particles emerging from the collisions. Alice was designed to study the collision of heavy ions. Only its trackers have full coverage while other sub-detectors only cover a subset of solid angles since these collisions are assumed to behave as thermal systems with spherical symmetry. LHCb is built as a single arm very forward detector. It is designed to study b -physics. On top of these, there are also smaller experiments, TOTEM near CMS and ALFA near ATLAS designed to measure the absolute value of the produced luminosity.

Being a member of the ATLAS collaboration I only used this detector for my analysis. The ATLAS detector is described in detail in chapter 5.

4.3 Proton Collision Physics

Collisions of protons are very complicated processes because protons themselves are composite particles. The internal structure of protons is governed by QCD in the non-perturbative regime and can therefore not be calculated from the theory using Feynman diagram technology. When probing the structure experimentally, the particle content of the proton depends on

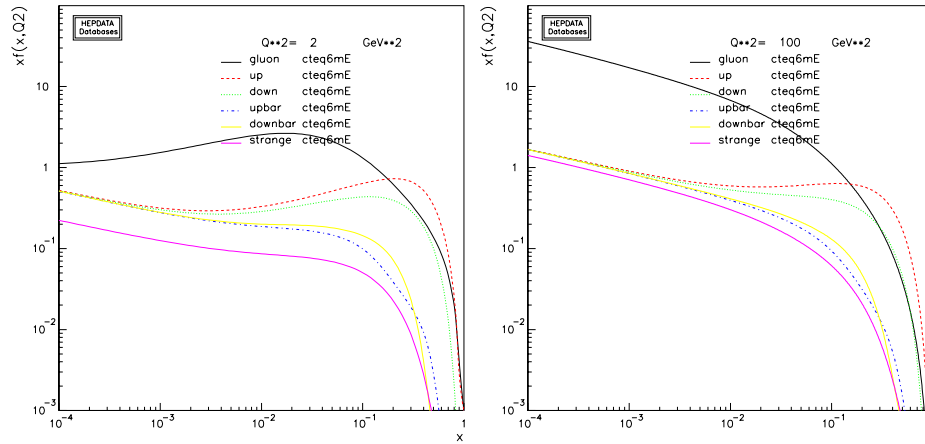


Figure 4.4: The CTEQ6M parton distribution function at $Q^2 = 2$ and 100 GeV^2 . Provided by [45].

the momentum that is exchanged between the probe and the parton but appears independent of the process in which the parton is subsequently involved. To lowest order, the proton can be described to consist of three valence quarks, two up-type and one down-type quark, bound together by some gluons. Since the binding energy of the proton far exceeds the rest masses of the partons, relativistic dynamics are needed to describe the momentum distributions of the partons. Figure 4.4 shows a momentum fraction distribution for low and high Q^2 , where Q is the exchanged momentum. As Q^2 is increased, it becomes increasingly possible to realise a virtual parton. Because of the non-perturbative nature of the proton structure, there exist an infinite number of virtual pairs of gluons and all types of quarks. The number of these particles diverges as the momentum fraction carried by them goes to zero. An input of energy is needed to make these particles real, which is why they become more visible at higher Q^2 . Since the PDFs cannot be calculated, they are obtained by a global fit to all particle physics data by specialised collaborations such as CTEQ [43] or MSTW [44].

4.3.1 The Rapidity Plateau

The entire process of a proton-proton collision can thus be split up into the parton selection and the hard process. From the point of view of the hard process, the proton can be thought of as just a beam of partons. Which partons are selected is governed by the PDFs as described above. Because of the shape of the PDFs, the combination of the two randomly selected momentum fractions, makes the rapidity of centre of mass of the hard collision approximately uniformly distributed with respect to the laboratory frame. The width of this uniform rapidity plateau depends on the process

and the beam energies. Harder processes that require a higher centre of mass energy, also require a larger momentum fraction from each beam, they therefore occur more centrally in the detector and have a narrower rapidity plateau. Since rapidity is the quantity that is additive under successive relativistic boosts, the secondary particles resulting from these collisions will also be uniformly distributed in rapidity. In the ultra-relativistic limit, rapidity reduces to pseudo-rapidity. The rapidity-plateau is also the reason that pseudo-rapidity is chosen as the natural measure of polar angle since equal steps in pseudo rapidity will be occupied by approximately the same number of secondary particles.

4.3.2 Total Cross-Section

The total cross-section of diffractive proton-proton collisions is many orders of magnitude larger than the cross-section of interesting physics. Figure 4.5 shows the expected rates of various physics processes at the LHC in comparison to the total cross-section σ_{tot} . For comparison the scale of the limit that we set with our analysis is added. This figure alone illustrates the need for a good trigger, i.e. to be able to reject the majority of all irrelevant events while still retaining most of the signal.

When comparing to the higgs cross-section predictions one can see that if R -hadrons should yet turn up at the LHC they would be one of the rarest processes known to exist.

4.4 Accelerator Operation

A rough overview over how the accelerators operate is helpful in understanding work behind our analysis. This is because the structure of the run periods and individual runs is reflected in the way the data is organised. Also, all pile-up dependent effects can vary within a run or between runs, so understanding what a run is, is quite important.

A run at ATLAS is a period of continuous detector operation in which the detector settings do not change. In all data that is used for analyses, a detector run has the same length as an accelerator fill. A fill is the procedure of filling, accelerating, colliding, and finally dumping the LHC beams. The filling and acceleration phase take less than an hour before the beams are ready to be collided. When the beams are brought into collision inside the detectors, this is what ATLAS uses as the start of a run. The beams are circling and colliding in the LHC until the beam is either lost through instability or until the instantaneous luminosity has fallen so low as to make it more worthwhile to dump the beam and refill.

In the case of beam instability or failure of any critical element of the LHC the beams are automatically dumped. An actual beam loss at full

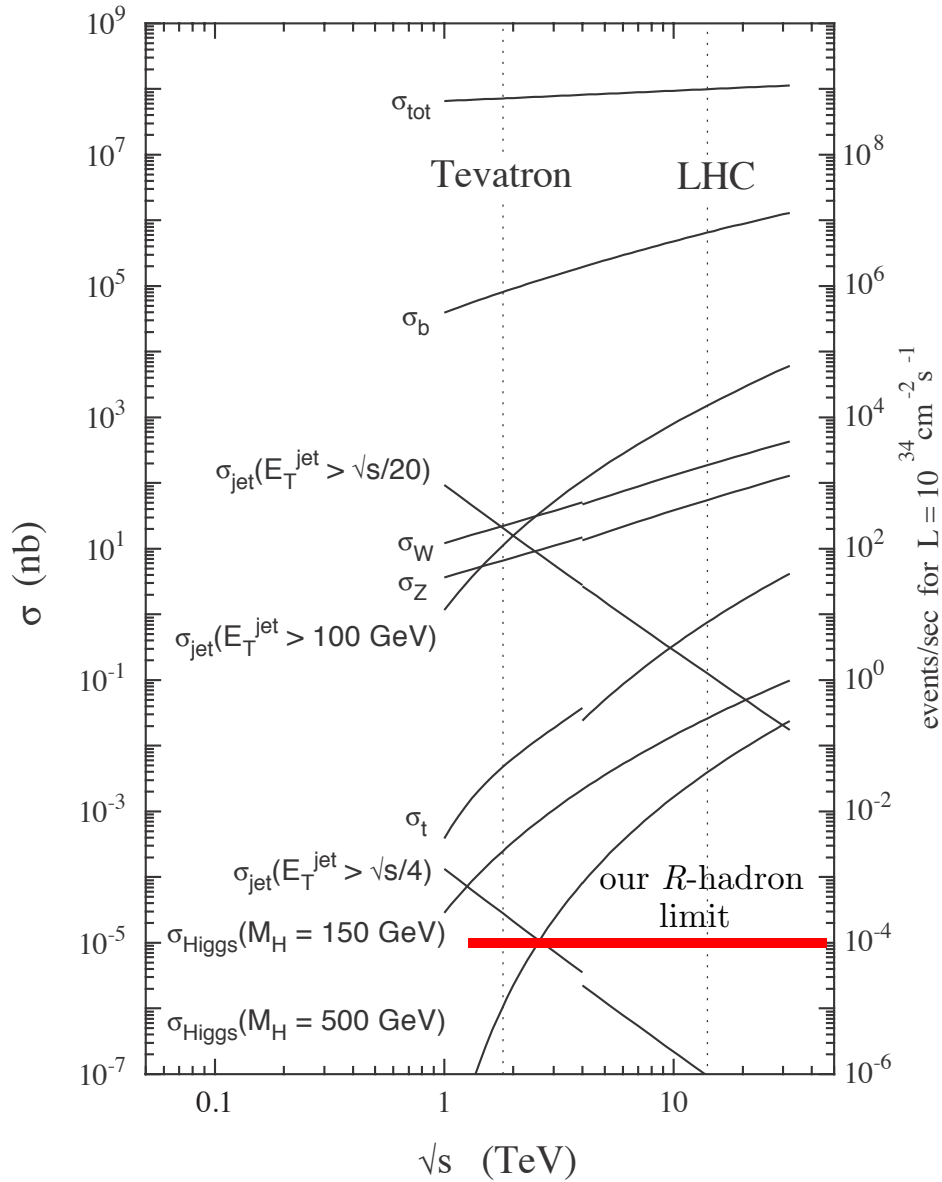


Figure 4.5: The cross-sections and expected rates of various processes against the collision energy. For comparison, the cross-section limit that was set with our analysis has been added. Figure from [46].

energy would be quite a catastrophic event. The total beam energy at 7 TeV per beam is about 360 MJ.

The instantaneous luminosity that the LHC delivers inside ATLAS is a measure of the total number of proton-proton collisions per second. There are a number of factors that limit the achievable instantaneous luminosity. With time these parameters are better understood and the degree of control over the beams is improved. Higher integrated luminosity is mostly associated with better discovery potential for new physics which is why the instantaneous luminosity is always pushed to the maximum safe levels by the LHC operators. Because of this instantaneous luminosity increases with time. This has a number of consequences for our analysis such as changing trigger menus and increasing occupancy. These will be mentioned in the relevant section.

For the data that was used for our analysis the LHC was run at 3.5 TeV per beam with a bunch spacing of 50 ns. The beam was filled with trains of bunches with gaps in between.

Chapter 5

The ATLAS Detector

The ATLAS detector is one of the main four experiments at the LHC and is placed around the LHC's Point 1, closest to CERN's main site. Its operation and parts are described in some detail in this chapter. Most of the information presented here is taken from the official technical description of ATLAS, which can be found in [47] where more details can be found. An overview of the entire ATLAS detector is shown in figure 5.1. It consists of several sub-detectors that are outlined in the following sections.

5.1 Layout

ATLAS is designed as a general purpose detector covering nearly 4π in solid angle. It is built out of several sub-detectors in onion-like layers. The inner sub-detectors are tracking detectors with a low material budget. They try to measure as much as possible about the passing particles while influencing them as little as possible. A 2 T solenoidal magnetic field bends the paths of charged particles allowing for a momentum measurement. The trackers are called the pixel detector, the silicon strip tracker (aka semiconductor tracker or SCT) and finally the transition radiation tracker (TRT).

Surrounding the trackers are the calorimeters. In general with increasing radial distance, the calorimeter density increases, and the spacial resolution decreases. This reflects the fact that electromagnetic showers occur earlier and are more well-described, hence precise measurements can yield good particle information. The later, hadronic showers are intrinsically more random making precise measurements less useful.

The outermost part of ATLAS is the muon spectrometer. Built as a low density tracker with its own toroidal magnetic field it can identify and track muons with high precision up to very high momenta.

In general the design of ATLAS was driven by a range of requirements such as good coverage in η , good muon identification and good triggering. Timing was only a requirement in as far as it was necessary to be able to

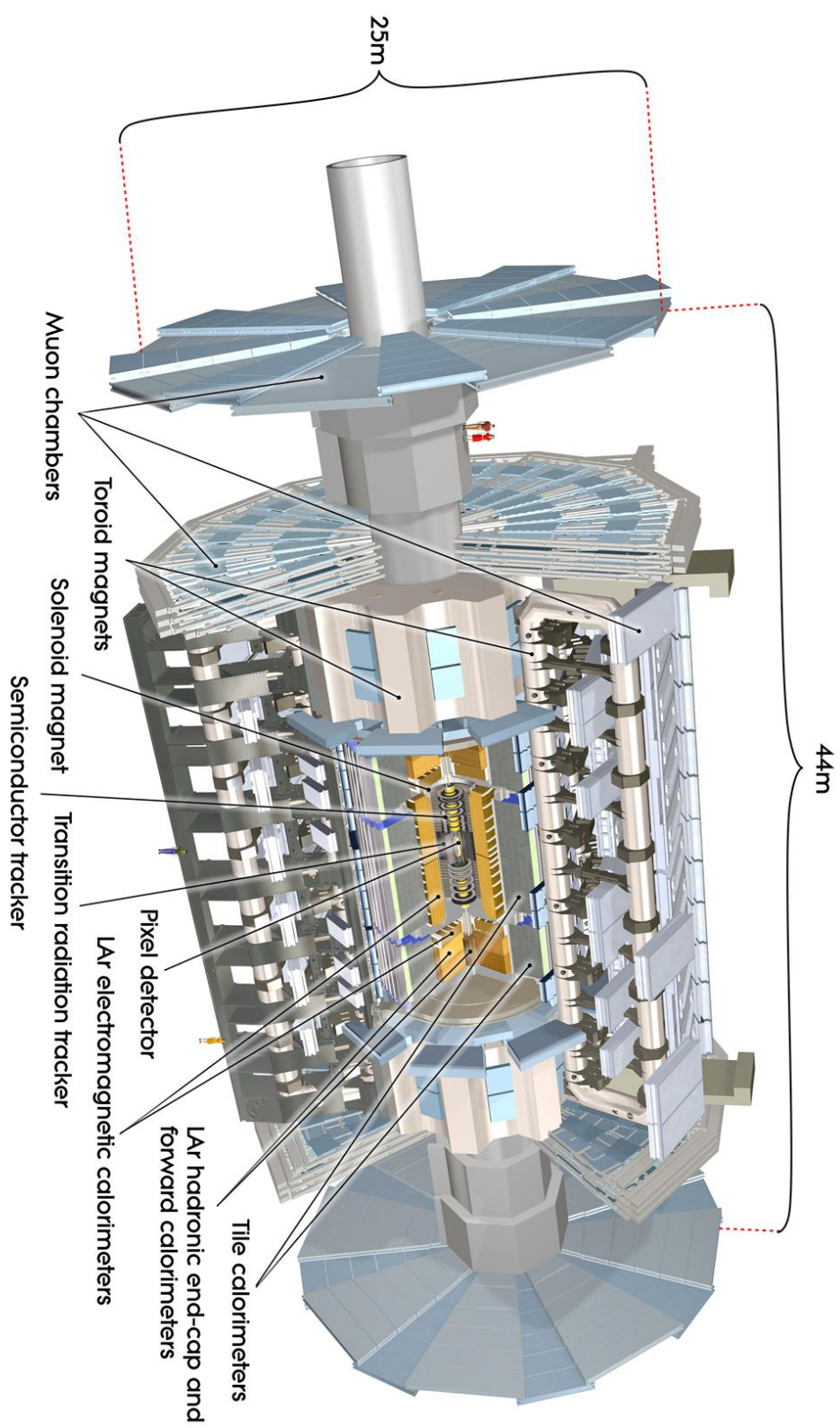


Figure 5.1: A cutaway of the ATLAS detector shows the layout of the sub-detectors. The total height 25 m, the length is 44 m. Figure from [47].

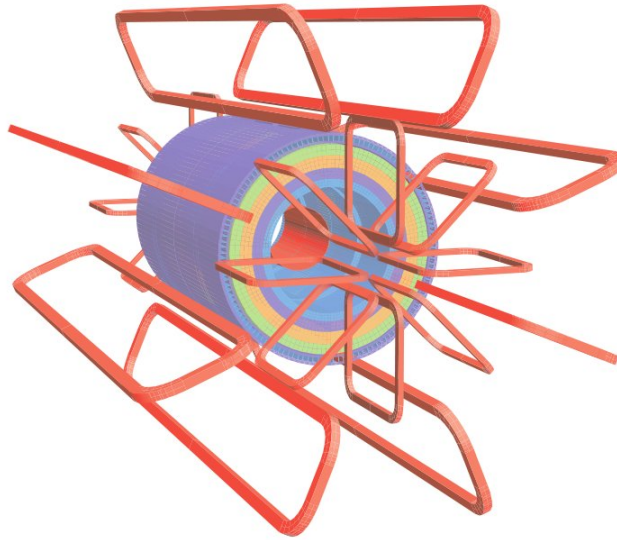


Figure 5.2: *The atlas magnet system consists of a solenoid and three toroid systems. Figure from [47].*

handle and distinguish events at the very high bunch-crossing frequency in nominal LHC operation, up to 40 MHz. This will be mentioned in more detail in section 5.10.

5.2 The Magnet System

The unique ATLAS magnet system consists of a solenoid and three toroid magnets as shown in figure 5.2. The solenoidal field with a strength of 2 T provides the bending power for the momentum reconstruction in the inner detector trackers. The toroidal system consists of a barrel and two end-caps which each consist of eight planar coils. The toroid coils interleave as shown in figure 5.2. The purpose of the toroid magnets is to provide an independent momentum measurement in the muon spectrometer by providing a bending plane perpendicular that of to the inner detector.

5.3 The Inner Detector

Figure 5.3 shows a cutaway of the entire inner detector (ID). There are three different tracking technologies which constructed as concentric cylinders for the barrel part, and as discs that are spaced along the z -axis for the end-cap. The innermost detector uses silicon pixel sensors to obtain distinct space points. The second uses pairs of crossed silicon micro-strips (SCT) to obtain tracking points. The outermost sub-detector, the Transition radiation tracker (TRT), uses gas-tube sensors and is only able to measure in

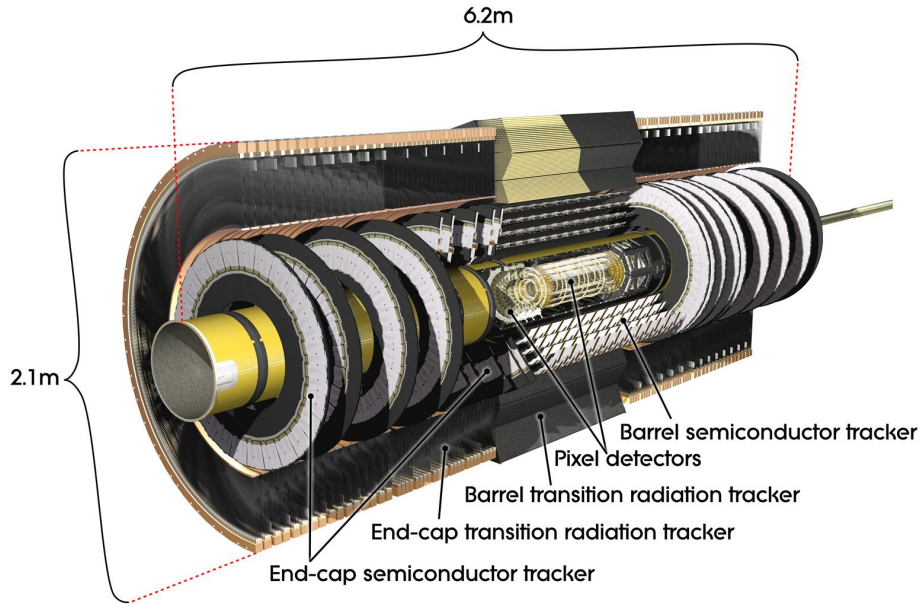


Figure 5.3: An overview of the ATLAS inner detector from [48].

the $r - \phi$ ($z - \phi$) plane in the barrel (end-cap).

The main purpose of the ID is to provide tracking and precision measurements of momenta of charged particles. The entire ID sits inside a 2 T solenoidal magnetic field which bends the paths of charged particles. The desired momentum resolution dictates the spacial resolutions of each sub-detector. Each sub-detector contributes about equally to the total momentum resolution.

5.3.1 Interactions of Ionising Particles

As particles pass through matter, they will interact with the electrons as well as the nuclei of the material being traversed. During these interactions a particle will in general lose energy. This energy can be deposited in the form of electronic excitations, ionisations, production of secondary particles, nuclear transformations or several others. This is a complex stochastic process that is difficult to calculate analytically which is why Monte Carlo (MC) methods are used extensively when trying to predict these interactions.

For energy loss based on ionisation there exists a parametrisation based on various models. Known as the Bethe-Bloch equation, it describes the average ionisation per unit material traversed. Its functional form is complicated and is split up into several regions of increasing $\beta\gamma$ of the particle. Figure 5.5 shows the graph of the Bethe-Bloch equation for muons on copper. For other particle species and materials the graph will be shifted and distorted.

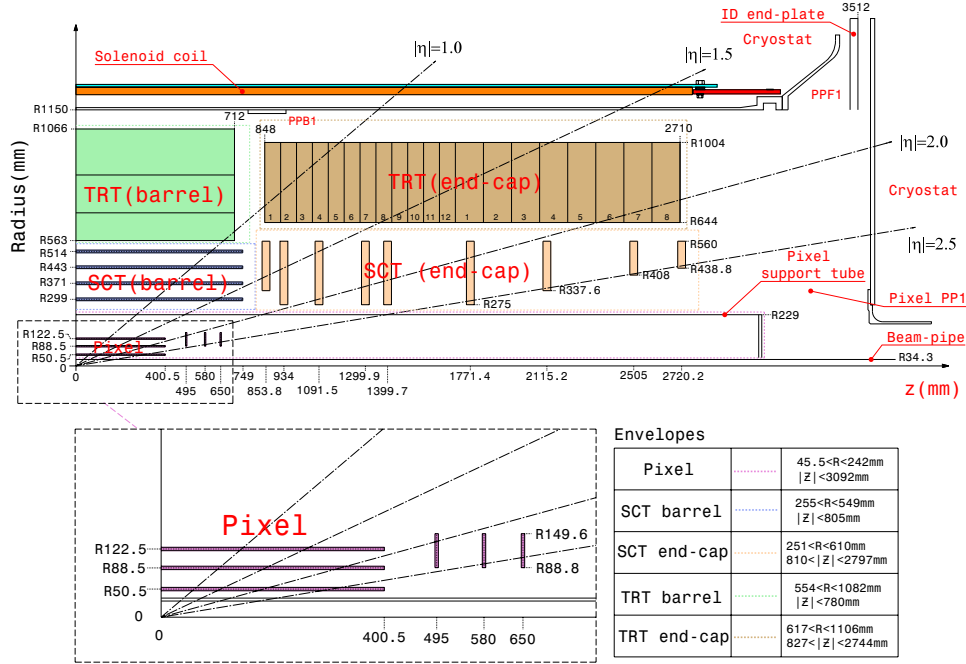


Figure 5.4: A detailed view of the layout of the inner detector. Tracking is possible out to $|\eta| < 2.5$. Figure from ATLAS detector paper [47].

ted slightly, but all general features remain. The regions that are of interest to us are the steep falloff to the Minimum Ionising Particle (MIP) level and the following slow relativistic rise. These occur in the range $0.1 < \beta\gamma < 100$ in figure 5.5.

While the average energy disposition is well defined, the actual process is stochastic. This means that in a given volume the energy deposited is a random number drawn from a Landau distribution [50] with its mode at the value given by figure 5.5. Because of its long tail, the moments of this distribution, like mean and variance, are not well defined.

5.4 The Pixel Detector

5.4.1 Layout

The pixel detector [47] is the innermost tracking detector of ATLAS. Its detector elements are silicon pixel sensors. The pixel detector provides at least three precision hits for most tracks in the region $|\eta| < 2.5$. Each hit has a precision of $10 \mu\text{m}$ in the $r - \phi$ plane and $115 \mu\text{m}$ in the z -direction of the barrel.

The barrel consists of three concentric cylinders while each end-cap consists of three disks. In total there are approximately 80 million channels. In

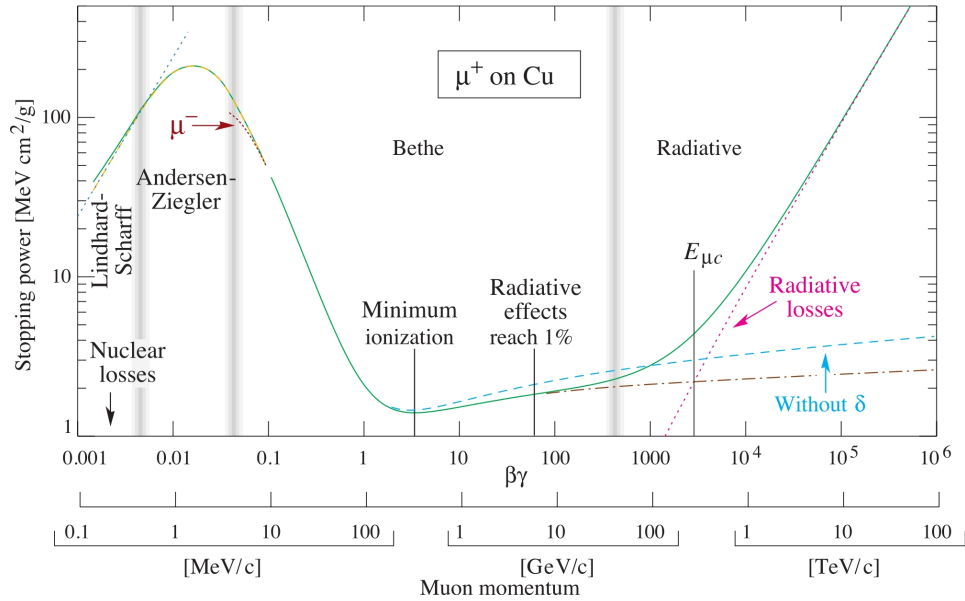


Figure 5.5: The graph of the Bethe-Bloch formula for the special case of muons impacting on copper. The monotonously falling region between $0.25 < \beta\gamma < 1$ will be used to convert the measured specific ionisation to $\beta\gamma$. Figure from [49].

each pixel where a certain signal threshold is crossed, the time over threshold (ToT) is measured with 8 bit dynamic range. The maximum ToT value on a single pixel corresponds to 8.5 times the average charge released by a MIP moving perpendicular to the detector. Pixels where the ToT exceeds this maximum value are discarded as bad measurements.

5.4.2 Specific Ionisation Measurement

The relation between ToT and the charge deposition in each pixel shows good linearity and stability as measured in devoted calibration scans, enabling an energy loss measurement for charged particles using the Pixel detector [4]. To calibrate variations between pixels or pixel modules, the average of all channels is equalised at regular intervals.

The charge deposited by a traversing particle is rarely deposited in a single pixel which is why pixels are grouped into clusters where the charge of the cluster is the sum of the charges of the pixels in the cluster after the local calibration. To define the ionisation loss for a track the average is formed between all clusters on that track. The average of several measurements from a Landau distribution is a biased estimator of the mode. Because of this, the highest cluster is discarded in the average from three or more clusters¹. The resulting value is often referred to as the pixel dE/dx measurement.

¹The highest two clusters are discarded from five or more clusters.

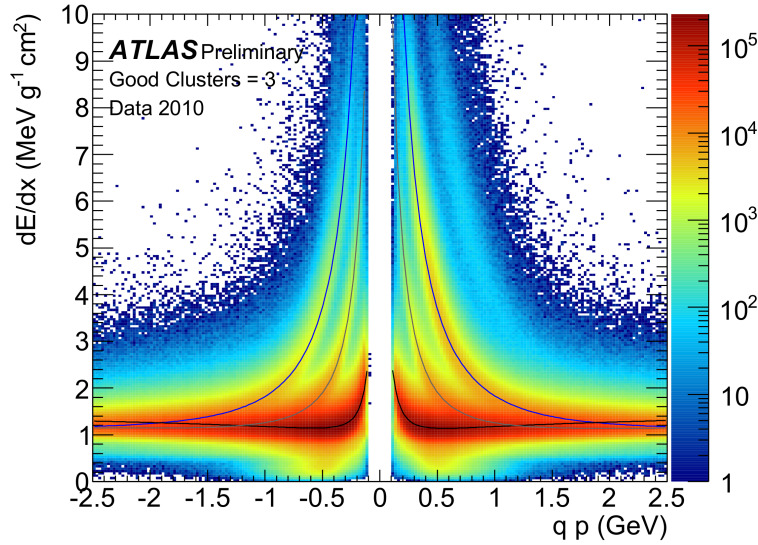


Figure 5.6: *Distribution of dE/dx versus signed momentum for minimum bias collisions and in the case of three good cluster tracks. In this data sample from 2010 collisions, tracks are reconstructed down to 100 MeV of transverse momentum. The distribution of the most probable value for the fitted probability density functions of pions (black), kaons (grey) and protons (blue) are superimposed. Figure taken from [8].*

(dE/dx refers to energy loss per crossed material.)

Figure 5.6 shows the distribution of the pixel dE/dx versus signed momentum in special low-pileup runs where momenta were reconstructed down to 100 MeV. Superimposed are three fitted Bethe-Bloch curves for various particle species. A fourth band, which is not fitted, can be seen on the positive side only. It can be ascribed to deuterons.

5.5 The Silicon Strip Detector

The silicon strip tracker (SCT) consists of 15912 single sided sensor modules that are divided into strips with $\sim 80 \mu\text{m}$ pitch in both the barrel and the end-cap. The sensors are paired back-to-back with a crossing angle of 40 mrad. This provides an accuracy of $17 \mu\text{m}$ in the $r-\phi$ and $580 \mu\text{m}$ in the z -direction.

The binary read-out electronics provide hit/no-hit information only, with no further level of detail. This was done in the interest of limiting bandwidth. For our analysis, this means that the SCT cannot be used except to provide precision momentum measurements.

5.6 The Transition Radiation Tracker

5.6.1 Layout

The transition radiation tracker (TRT) [47] is a gas tube detector. It consists of conducting tubes (or straws) of 4 mm diameter, built of carbon and aluminium, with a thin (31 μm) tungsten wire running down their centre. The straws are packed in modules and are aligned along the z -axis in the barrel. The end-caps consist of a set of wheels of several straw layers each. The straws in the end-cap wheels are aligned in the radial direction. The end-cap straws are instrumented on the outer edge of the wheel. The straws in the barrel are split in the centre (at $z = 0$) with a glass bead insulating the two wire-ends and are instrumented at both ends of the barrel. The innermost nine straw layers of the barrel are split into three parts where only the outer 31.2 cm on both sides are active. This reduces the occupancy in the straws closest to the interaction point. The space between the straws is filled with a fibrous radiator material in the barrel, while sheets of radiator are inserted between successive straw-layers in the end-cap wheels. The purpose of the radiator is to maximise the emission rate of transition radiation.

The tubes are filled with a gas-mixture consisting of 70% Xe, 27% CO₂ and 3% O₂. The xenon, with its high nuclear charge, maximises the interaction cross-section for TR which typically lies in the X-ray spectrum.

A negative high voltage (HV) is applied to the straw walls while the wire is kept at ground voltage. This creates a gas cascade effect which amplifies any primary ionisations by $\mathcal{O}(10^4)$. After this intrinsic amplification the signal is strong enough to be amplified further by standard semiconductor technology.

Each track has on average about 30 hits with a spacial precision of better than 130 μm allowing good track identification and momentum measurements. On top of this the TRT provides excellent electron identification by capturing transition radiation as explained below.

An illustration of a track passing through TRT straws is shown in figure 5.7. It illustrates how a track can have low threshold (LT) hits, high-threshold (HT) hits, dead straws and outliers, which are hits that are not crossed by the reconstructed track but are activated nonetheless.

5.6.2 Signal Reception

The electrons from any primary ionisations in the gas volume of a straw immediately drift towards the central wire at a fairly constant rate while the remaining ions drift towards the straw wall. A simulation of this process is shown in figure 5.8. Once the electrons arrive at the wire, they cascade to produce more and more secondary electrons. During this cascade, a charge will be induced in the wire. The signal from this charge travels in

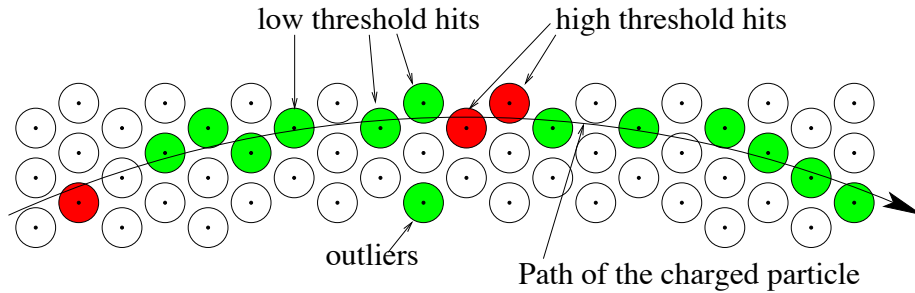


Figure 5.7: An illustration of terms when talking about a TRT track. A track contains LT and HT hits. Some straws may be dead and some hits may be deemed outliers by the tracking algorithm. Note, the straw diameters are not to scale.

both directions away from the ionisation. The signal going towards the instruments will be absorbed directly while the other signal will first be reflected at the insulated end of a straw before returning and also being absorbed by the instruments.

The signal is shaped at the front-end electronics so as to get rid of the long tail created by the positive ions which drift much slower than the electrons. After shaping, the signal is digitised. This is done by monitoring when the signal crosses each of two thresholds, the low threshold (LT) and the high threshold (HT). The LT is sampled every 3.125 ns or eight times per nominal bunch crossing (BC) of 25 ns. The HT is sampled once per BC. Following a trigger, three BC periods are read out as event information. Each sample is saved in a single bit giving a total of 27 bits per straw per event. The process of digitisation is illustrated in figure 5.9.

5.6.3 Aside on Electron Gas Drift

Looking at figure 5.8 one can see that the electrons drift in an arc that could roughly be described as circular. Drawing only on knowledge from elementary electrodynamics about motions of free charges one might assume that the observed clockwise curl of the electron paths requires a magnetic field that is pointing into the plane of the paper. The source from which I obtained the figure does not state the direction of the field, but from my own reasoning I can conclude that the magnetic field must in fact point in the opposite direction, namely out of the plane of the drawing.

The reason for this reversal lies in the physics of electron gas drift. A free charge placed with any initial velocity in crossed electric and magnetic fields will perform an oscillatory motion in the direction of the electric field and will steadily progress in the direction of the vector product of the two fields. In the presence of a gas, and if the charge is an electron, the direction of motion of the electron is frequently randomised through collisions with

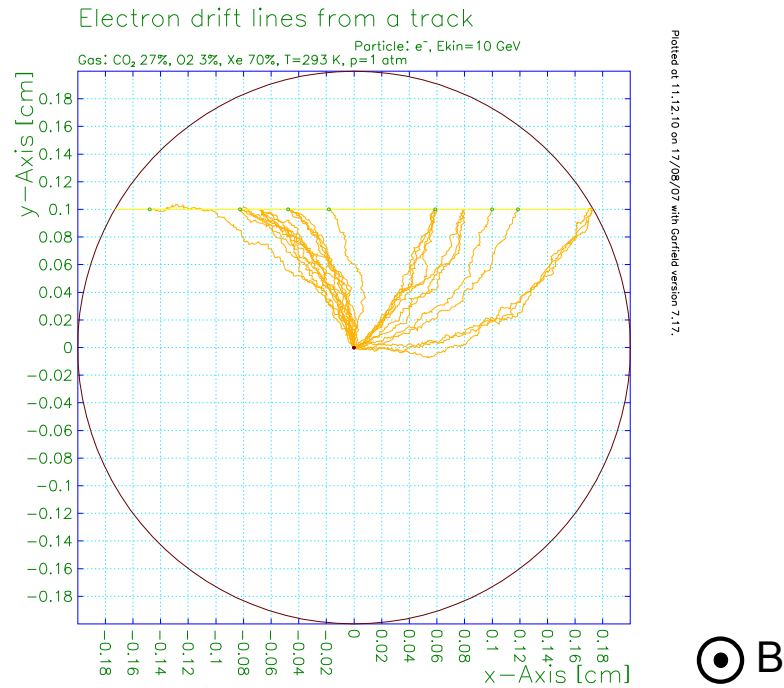


Figure 5.8: Simulation of the electron drift in a TRT straw with a 2 T magnetic field pointing out of the plane of the paper. Figure from [51]. For a discussion of the direction of the magnetic field, see section 5.6.3.

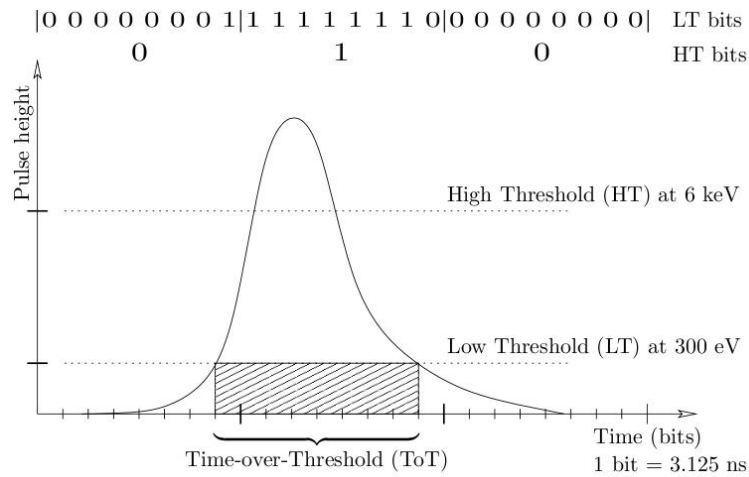


Figure 5.9: An illustration of how the TRT signals are digitised. The LT is sampled 8 times per bunch crossing (BC), the HT only once. Three BC are recorded for each hit. Figure from [52].

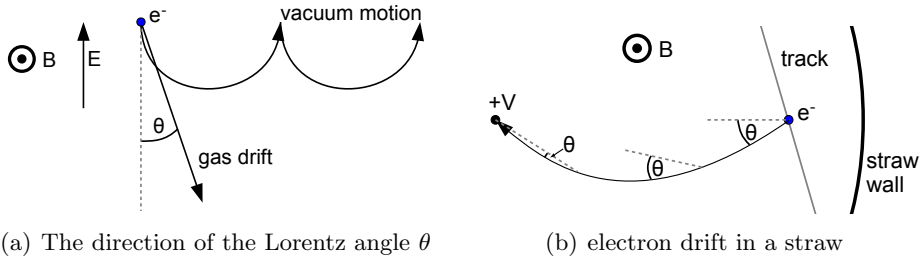


Figure 5.10: *The path of an electron in the TRT gas will be bent in a sense that is opposite to the curl expected from a free electron. The size of θ in figure (b) will vary, but its direction is never reversed.*

the gas. The net effect is that in this situation, the electron drifts in a direction that has a certain angle θ to the electric field. This angle is called the Lorentz angle [53]. The situation is illustrated in figure 5.10(a). The direction of this deviation from the electric field direction is in the same direction as the force acting on a free electron moving along this path. i.e. in the direction that is the negative of the vector product of the electric and magnetic fields. The size of θ will depend on several factors, one of which is the electric field strength which varies strongly along the path. The direction will be the same along the the drift path though, giving the appearance of an inverted arc as in figure 5.10(b).

The final confirmation about my view of the magnetic field direction will have to come from a direct inspection of a the Garfield simulation code that was used to produce figure 5.8. I would like to thank Werner Riegler (Werner.Riegler@cern.ch) for valuable discussions on this topic.

5.6.4 Tracking

The way that the TRT achieves a spacial resolution that is much better than the straw diameter is via the method of drift circles. The ionisations left by a track drift towards the wire at an approximately constant speed. Hence, the time after the collision at which the signal arrives at the wire is proportional to the distance of closest approach of the track to the wire. Using the time measurement from the LT sampling of the leading edge of the pulse peak, a circle, centred on the wire, can thus be defined for each straw to which the track must be tangential. A number of timing and alignment calibrations are needed to improve on this simplistic picture before an optimal spacial resolution can be achieved. Using this method, the TRT can contribute considerably to the total momentum resolution in the ID.

Figure 5.11 shows the distribution of measured track-wire distances, called r , as a function of the measured drift time t . It also shows the function for the $r - t$ relation that is used in tracking instead of a strict

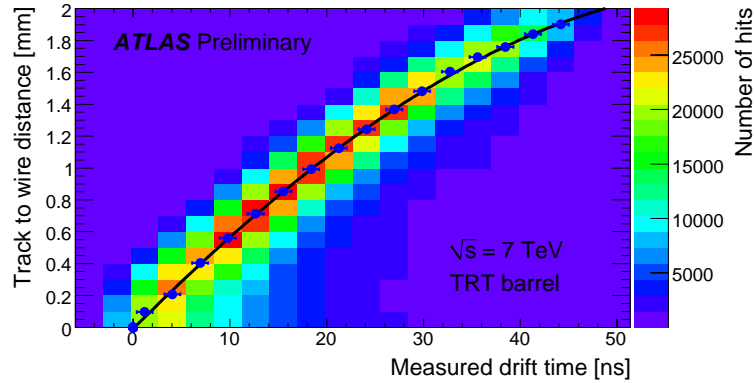


Figure 5.11: *The relation between track-wire distance and drift time. Also shown is the fit to the average drift times that is used for tracking. Figure from [54].*

proportionality.

5.6.5 Electron Identification

Principle

A charged particle traversing the TRT will create $\mathcal{O}(20)$ ionisation centres in the gas of a each straw (for a track passing through the wire). The negative charges from these ionisations first drift towards the wire and finally cascade as they encounter the large field gradient near the wire. The rate at which these primary ionisations are created is governed by the same dynamics as the ionisations in the pixel detector. It is a stochastic process with a certain probability of an ionisation occurring per unit material crossed. The actual energy deposited in a straw is thus randomly distributed and follows a Landau distribution. The long tail of this distribution means that the HT can sometimes be activated by random upwards fluctuations of the deposited ionisation. For pions this happens at a rate of about 3-5% of all hits. In fact the HT is regulated to ensure this low background rate.

The TRT gets its name from a second process by which ionisation can occur, namely transition radiation (TR). TR is generated when ultra-relativistic charged particles cross the boundary between two materials of different refractive indices. At each such crossing there is a chance for the emission of a collinear TR photon which lies in the X-ray spectrum. The TRT contains radiator material surrounding the straws that is meant to provide a large number of such transitions, thus maximising the rate of TR emission. A TR photon can be absorbed by the xenon in the straw gas and causes a large amount of ionisation. A TR detection like this will be registered by the HT.

The rate of TR emission is strongly coupled to the Lorentz gamma factor γ where only the highest values of γ provide appreciable rates. At the typical

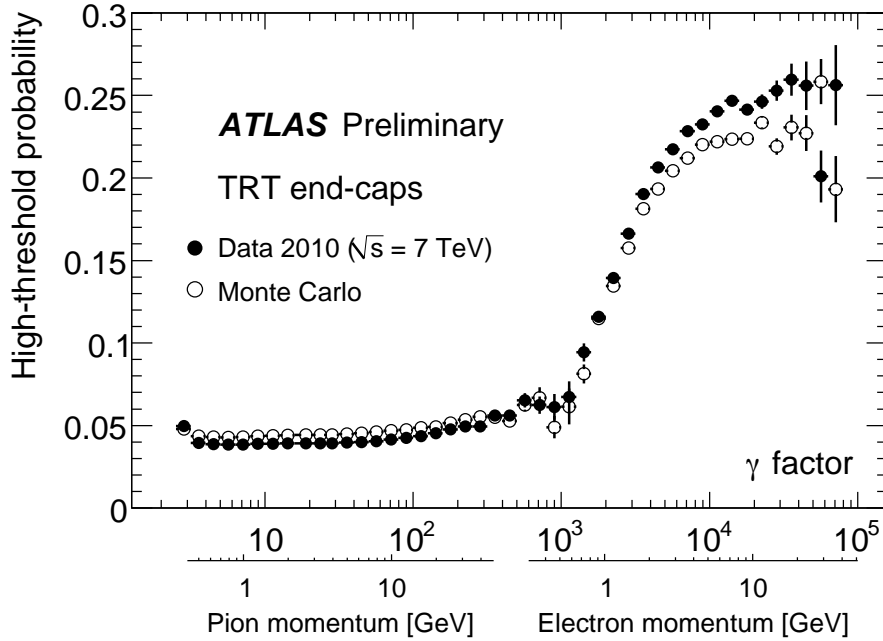


Figure 5.12: *The onset of transition radiation as a function of the γ factor is shown by samples of electrons and pions in the TRT end-cap in 2010 data. Figure from [54].*

energies of secondary particles in ATLAS only electrons have a γ -factor that is large enough to produce TR. The detection of high rates of HT hits on a track is thus a good indication of the track belonging to an electron. The dependence of TR emission as a function of γ is measured directly from data and used for the calculation of the electron likelihood of a track. Figure 5.12 shows such an onset curve as obtained for the TRT end-cap in 2010 data. For this plot electrons and pions are combined by calculating their respective γ as $\gamma = E/m$. Electrons are identified via a tag-and-probe method using photon conversions. For the pion sample, all tracks in an event are used and are assumed to have the pion mass, this gives very good purity. Figure 5.12 was in fact the first direct measurement of the HT onset curve carried out with 2010 data only.

Application

In practice most analyses work with cuts where a particle is decided to either be electron-like or not based on a certain statistic. Particles failing the cut are discarded. A simple statistic to cut on would be the fraction of HT hits on a track. This is the simplest discriminator on e vs. π rejection that can be obtained from the TRT and already contains the majority of

the information. It is often deemed good enough and used directly. Using a cut on this fraction, requiring a 90% efficiency for electrons in the range 1-200 GeV, the pion misidentification probability is about 5%.

If one is willing to use more advanced approaches however, some additional separating power can be gained. Within the ATLAS software there is a tool called `TRT_ElectronPidTool`, later ‘the tool’, that implements the following algorithm for a likelihood-ratio based discriminator.

Working on updating and maintaining this tool was part of the technical work that allowed me, the present author, to become a full signing member of the ATLAS collaboration.

The tool uses as input the onset curve as shown in figure 5.12. The curve was found to depend on a number of local factor, such as the radiator material and thickness, which is why it had to be found separately for the TRT barrel and the A and B wheels of each end-cap which have slightly different constructions.

For each hit on a given track the tool loops over the hits to compute the likelihood of the observed HT hit pattern for both an electron and a pion mass hypothesis:

$$L_\pi = \prod_i^{\text{hits}} P_{\text{HT/LT}}(i|p, m_\pi, \text{location}) \quad (5.1)$$

$$L_e = \prod_i^{\text{hits}} P_{\text{HT/LT}}(i|p, m_e, \text{location}) \quad (5.2)$$

where P is the probability of observing the given HT information on the given hit, p is the track momentum and m is a mass hypothesis. The resulting likelihood ratio L , defined as

$$L = \frac{L_e}{L_e + L_\pi} \quad (5.3)$$

is the optimal discriminator of the electron versus the pion hypothesis that can be obtained from the HT information alone under the assumption that all hits within a detector part are equivalent.

5.6.6 Double Binomial Fit Method

As stated above, the way that the onset curves as in figure 5.12 were arrived at was by separating the tracks into electron-like and pion-like tracks, and then use this species assumption to convert the measured momentum to a gamma factor.

In fact there is a considerable more powerful way of arriving at the same information. If one assumes that the HT-probability for the hits along a single track is approximately constant, then the number of HT hits will be a random number chose according to a binomial distribution. In the case that $p_{\text{HT}} \ll 1$ this distribution can be approximated by a poisson distribution. When grouping together a sample of tracks that are very similar, it should

be possible to fit a binomial distribution to the distribution of HT hits on these tracks.

This picture needs to be expanded somewhat before it becomes useful. In practice, tracks can be binned in η and momentum as well as N_{hit} , the number of TRT hits on track. A narrow momentum bin will make sure that all tracks have approximately the same γ factor and therefore the same p_{HT} , provided they come from the same particle mass. If, as we assume, the sample consists of two species, electrons and pions, the distribution of N_{HT} should follow the sum of two binomial distributions.

Within a single bin in η and momentum, tracks of different N_{hit} are expected to share the same $p_{\text{HT},e}$ and $p_{\text{HT},\pi}$ while the actual numbers of N_{HT} will naturally be different. Given a sample of tracks that have been binned like this, one therefore needs to carry out a combined fit of all slices of N_{hit} using a single set of the parameters $p_{\text{HT},e}$ and $p_{\text{HT},\pi}$. In practice, there are two other parameters needed to fully describe the sum of two binomial distributions, the normalisation N and the electron fraction f_e in each N_{hit} slice. The fitted expectation E is then:

$$E(N_{\text{HT}}|N_{\text{hit}}, p_{\text{HT},e}, p_{\text{HT},\pi}, f_e) = N(f_e P_{\text{Bino}}(N_{\text{HT}}|N_{\text{hit}}, p_{\text{HT},e}) + (1 - f_e) P_{\text{Bino}}(N_{\text{HT}}|N_{\text{hit}}, p_{\text{HT},\pi}))$$

where $P_{\text{Bino}}(n|N, p)$ is the normalised binomial probability for getting n successes out of N tries with an individual chance p .

In order to reduce the number of free parameters, the normalisation N can be fixed from the normalisation of each histogram. The electron fraction f_e can be fixed by using the histogram mean HT fraction f_{HT} and using the fact that if the data is correctly described, then

$$f_{\text{HT}} = f_e p_e + (1 - f_e) p_\pi. \quad (5.4)$$

This way only two parameters are used to fit $\mathcal{O}(20)$ histograms in each η and momentum bin, leading to very good fit convergence.

This method has been the subject of a Master's Thesis by Troels Schönfeldt [55] who worked with me in 2011. He approximated the binomial distributions as Poisson distributions and therefore called the method 'the double poisson method'.

Figure 5.13 shows an example slice of such a multi-histogram fit. It can be seen that the electron component of the sample can be reasonably well extracted.

Once the electron component in a given sample has been fitted by this method, a likelihood ratio estimator can again be used to assign an estimator or even a weight to each individual track.

The method has many strengths.

- Due to the very low number of free parameters, the fit converges very easily even for very low numbers of tracks per η /momentum bin. Down

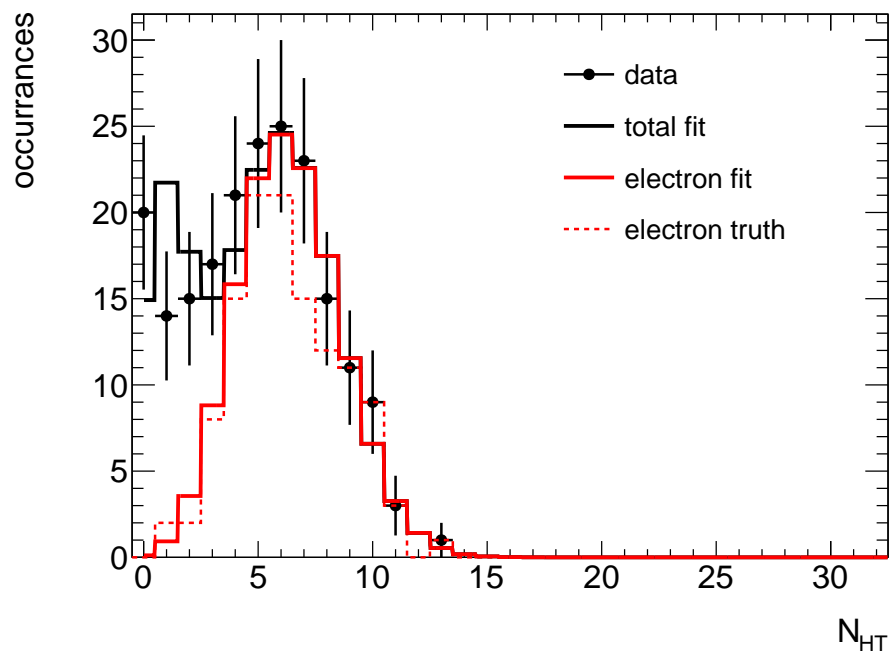


Figure 5.13: An example result of the double binomial fit in a slice of $|\eta| < 0.44$, $12.6 \text{ GeV} < p < 31.7 \text{ GeV}$ for $N_{\text{hit}} = 32$ using an MC sample of tracks that have passed loose electron identification cuts.

to 50 tracks spread across all N_{hit} slices the fit has been shown to converge well.

- The resulting $p_{\text{HT},e}$ is not biased by the admixture of other minimal ionising particles in the fit. The returned value is the true probability and not the the sample mean.
- Besides $p_{\text{HT},e}$ and $p_{\text{HT},\pi}$ the method is also able to extract an accurate value of f_e from samples with a wide range of compositions down to electron fractions of 1 % and lower while still giving good estimates of $p_{\text{HT},e}$.

There are however also a number of problems with this method:

- The fit relies on some degree of mixture between the species. Samples that are too homogenous can not be used.
- The fit relies on the existence of exactly two species. If a third species, such as protons, are in the sample, it would become necessary to include three binomial distributions in each slice. While this is not a problem in principle, it introduces a free parameter into each N_{hit} slice which can not easily be fixed. This leads to much worse convergence properties, spoiling the robustness of the method.
- The fit converges better when the range of true p_{HT} in each species is narrow. This can be difficult to achieve when one tries to recover the onset region of the HT onset curve.
- Momentum slices where both species lie above or below the onset can be difficult to fit because both p_{HT} values are very similar.
- The method can only be employed if the HT fraction has not previously been cut on in a given sample.
- Because the method uses the total HT count on a track, the difference in HT probabilities between different detector parts can not easily be taken into account for tracks that cross several of the parts.

In summary, this method shows many promising features, but much more work would be required to address a number of issues that are still problematic. The final gain from this method is quite small since only minor gains in electron identification can be expected compared to the potential work-load.

5.6.7 Specific Energy Loss Measurement

Efforts have been made to use information from the TRT to measure the specific energy loss of particle tracks. This measurement is based on the

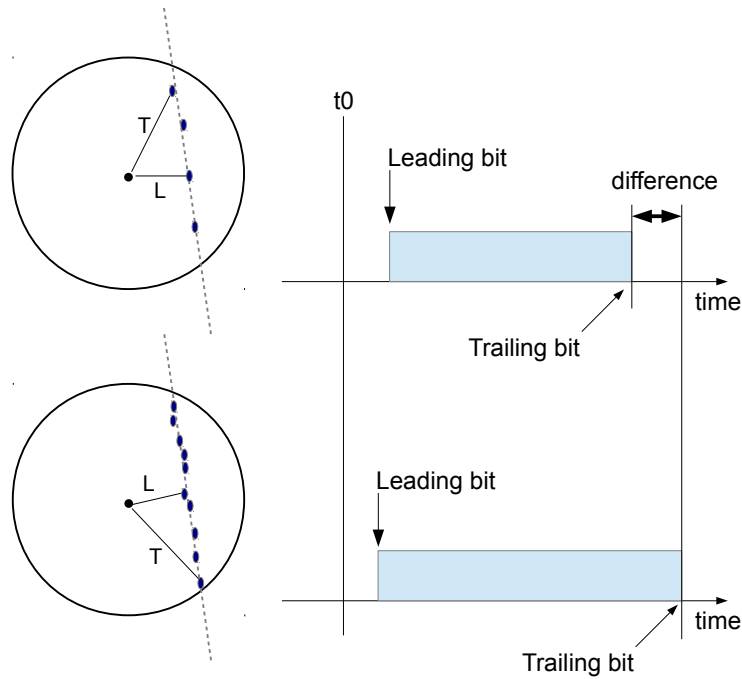


Figure 5.14: *The situation in the TRT straw for a minimum ionising (top) and a highly ionising track (bottom). The furthest cluster will have a larger distance from the straw wall in lower ionising tracks.*

time-over-threshold (ToT), i.e. the time number of time bins for which the LT bit is active. A particle with a larger specific energy loss will typically have a larger ToT. This is explained in figure 5.14. At constant drift speed the leading edge (LE) of the LT signal is highly correlated with the distance of closest approach while the trailing edge (TE) comes from the straw wall. In practice, this situation only correspond to the maximum achievable ToT because the discrete ionisations may cause the actual ToT to be less as illustrated in figure 5.14. Longer ToT will in general correspond to larger dE/dx although the actual relationship has a number of other influencing facts and needs to be calibrated on data.

The best estimate for dE/dx using this approach is shown as a function of momentum in figure 5.15. Proton and Kaon bands can be discerned.

This method of measuring the specific ionisation was not used in our search. It is far less sensitive than the pixel dE/dx when the quantity of interest is $\beta\gamma$. Hence not much sensitivity could have been gained by including it. More importantly though, this dE/dx value was found to have a strong dependence on particle momentum. Taking this into account would have made our data based background estimation method much more complicated.

One aspect in which this method has advantages over the pixel dE/dx

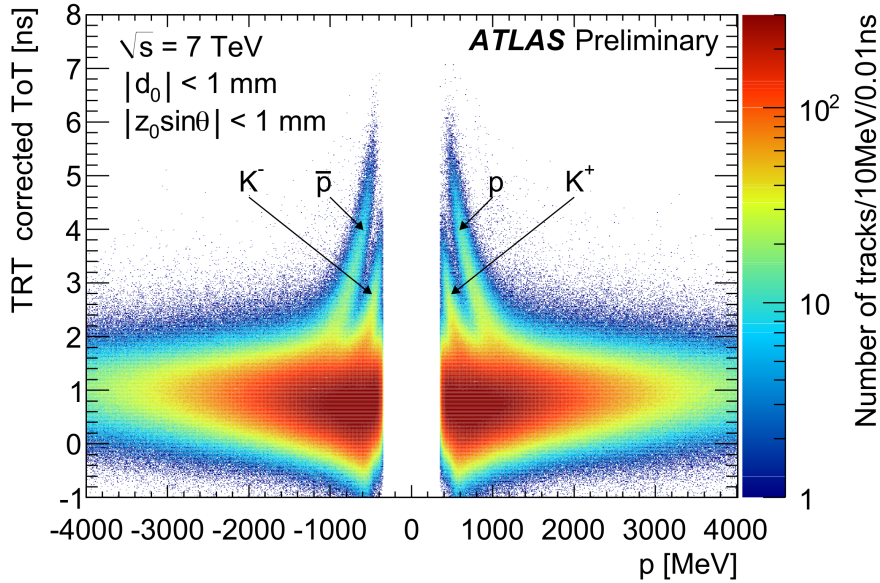


Figure 5.15: The best corrected estimator of the specific ionisation of tracks in the TRT as formed from the signal time over threshold of all TRT hits. Figure taken from public TRT results [54].

measurement is that it does not saturate. The pixel detector is quite noisy which makes it necessary to reject single pixel energy deposits that exceed ~ 8 MIPS*. Extremely high energy deposits will thus never be detected by the pixel detector. Such large ionisation energy deposits are not expected from any SM particle, but can be a strong signal for multiply charged, highly ionising stable particles predicted by some models. In the TRT there is no limit to the amount of energy deposition that will still lead to a signal, which is why it was used in a search for such particles published by ATLAS [6].

5.6.8 Time of Flight Measurement

From figure 5.4 one can see that the distance from the interaction point to the TRT sampling volume is between 563 and 2890 mm. At typical β values of 0.5 or 0.7 this corresponds to time delays between 3.8 and 19.3 ns or 2.7 and 13.8 ns respectively. The TRT has a time resolution of 3.125 ns on individual LT samples. Seeing as the large end of these times correspond to several LT bins and using information from several hits, a ToF measurement might be feasible.

There are several restrictions that make this measurement very difficult to carry out in practice. The short flight distance make this measurement only useful for the lowest β values. At these speeds, the ionisation is signific-

*A MIPS is the expected energy deposit from minimum ionising particles.

antly larger than average. According to section 5.6.7 this effect counteracts the effect of delayed arrival. To differentiate these two effects, detailed calibration studies would be necessary. Unfortunately there are no SM particles that are suitable as calibration probes. Slow protons, which were used to calibrate the pixel response, are not able to penetrate to the outer edges of the TRT. Monte Carlo studies alone are not adequate to calibrate this measurement.

Partly because of the mentioned difficulties, to date no time-of-flight measurement has been carried out in ATLAS using the TRT. We therefore did not include it in our analysis.

5.7 The Calorimeters

A full overview of the calorimeter assembly is shown in figure 5.16. Calorimeters stop incoming particles and measure the energy of the produced shower. Calorimeters are normally divided into electromagnetic and hadronic types. The electromagnetic calorimeters consist of the Liquid Argon (LAr) barrel and the electromagnetic end-caps (EMEC) which use the same technology as the the LAr barrel. The hadronic calorimeters consist of the tile barrel and extended barrel, the LAr hadronic end-cap (HEC), and the LAr forward (FCal). For the purpose of our analysis it is more suitable, however, to distinguish mainly between LAr and tile calorimeters due to their different timing resolution.

LAr calorimeters use liquid argon gas as the active medium. Ionisation charges that are created in this active medium by the passage of charged particles are collected on electrodes and counted electronically. The active medium is interleaved with a denser heavier metal, called the radiator material. The radiator provides a high interaction cross-section for the creation of secondary particles. This causes incoming high particles to repeatedly cascade in to secondaries leading to what is called showers.

In the LAr barrel and the EMEC, lead and steel is used as the radiator and an accordion folding of the radiator-active medium sandwich structure allows for full ϕ -coverage combined with quick readout. The HEC uses copper as radiator material. The FCal uses copper and tungsten. Copper was chosen for better heat removal from the areas with highest particle flux.

The size of the LAr gap varies throughout the LAr calorimeters leading to very different timing resolutions.

The tile calorimeter is composed of stacks of tiles of alternating materials, steel radiator tiles and plastic scintillator tiles. The steel radiators again provide a high interaction cross section to produce showers. The scintillator tiles lie in the x-y plane and are read out by Photon multiplier tubes at the outer edge of the calorimeters via wavelength-shifting fibres.

All calorimeters are segmented into cells of roughly constant steps in $\Delta\eta$

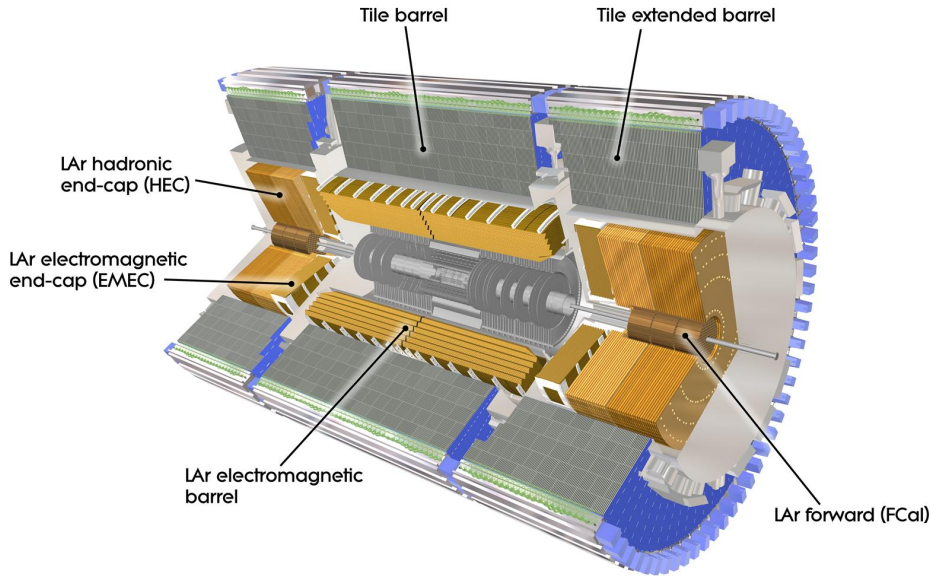


Figure 5.16: An overview of the calorimeters in the ATLAS detector. Figure from [47].

and $\Delta\phi$ and also in layers in the radial direction. The reason for the transverse segmentation is to be able to measure η and ϕ of the particle that caused the shower. This is of course important for physics measurements, but also needs to be known in order to match the shower to a possible track for the full reconstruction of a particle. The reason for the radial segmentation is to be able to recognise shower shapes. This shape recognition makes it possible to discern electromagnetic showers from hadronic showers. The sizes and thicknesses of the cells vary considerably as they were chosen to optimise shower shape identification capabilities while keeping the number of channels low.

The signals from the LAr electrodes are amplified, shaped and digitised in the front end electronics situated close to the calorimeter. After shaping, the signal is sampled at 40 MHz as shown in figure 5.17. The resulting samples are used to reconstruct the pulse energy and thereby the calorimeter energy deposit.

In the tile calorimeter the light signal generated in the scintillating tiles is transported to photo multiplier tubes (PMTs) at the outer edge of the detector by wavelength shifting fibres. The PMT output is also sampled every 25 ns and peaks are reconstructed from a number of samples.

The timing resolution of the tile calorimeter is better than that of the LAr calorimeter.

All calorimeter cells have an inherent noise level and a lower cut on the

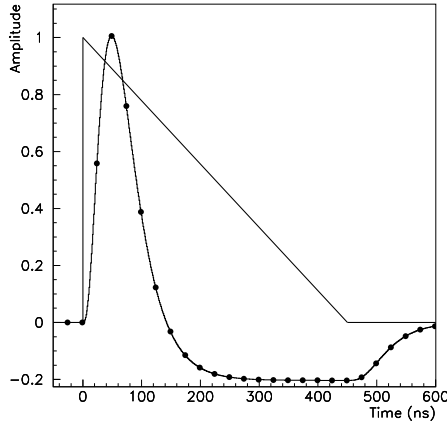


Figure 5.17: Amplitude versus time for a triangular pulse of the current in a LAr barrel electromagnetic cell and of the front end board output after shaping. The sampling points every 25 ns are indicated. [47]

cell energy deposit is imposed before a cell hit is used in our analysis.

5.8 The Muon Spectrometer

The ATLAS muon spectrometer [47] consists of four different detector technologies. Precision measurements are obtained from Monitored Drift Tube chambers (MDT) except in the innermost tracking layer of the forward region ($2 < |\eta| < 2.7$) where cathode strip chambers (CSC) (a type of multi wire proportional chamber) are used due to their higher rate capability and time resolution. To provide fast triggering signals, resistive plate chambers (RPC) are used in the barrel region up to $|\eta| < 1.05$ while in the end-cap thin gap chambers (TGC) are used in $1.05 < |\eta| < 2.4$.

An overview over how the detectors are arranged is shown in figure 5.18. In the barrel region the detectors lie in three concentric cylinders at radii of approximately 5 m, 7.5 m and 10 m. The end-cap is constructed as large wheels in the transverse beam plane at distances of $|z| = 7.4$ m, 10.8 m, 14 m and 21.5 m from the interaction point.

The MDTs are gas tube detectors somewhat similar to the TRT straws. MDT tubes have a diameter of 3 cm and each chamber consists of bundles of tubes with 3 to 5 layers per chamber. The MDT tubes are read out with a high time precision with an RMS of 0.78 ns.

The RPC chambers are gaseous parallel electrode plate detectors. They have perpendicular layers of strips, one measuring the η direction, one measuring the ϕ direction of a passing track. Both are sampled with 3.125 ns granularity. The strip propagation times can be subtracted. The reason for

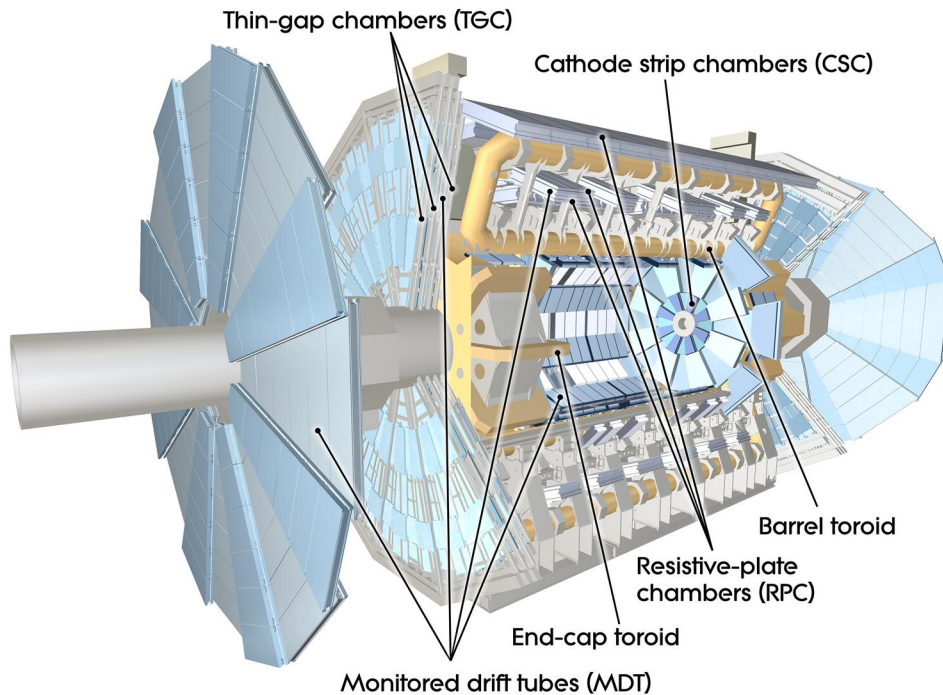


Figure 5.18: A cut-away view of the ATLAS muon spectrometer. The toroid magnets are shown in yellow while the detection elements are coloured in shades of blue. Figure from [47].

the good time resolution of the RPC chambers is that ionisation clusters from tracks form avalanches directly instead of first having to drift to a wire as in the TRT and MDT tubes.

5.9 The Trigger System

The rate of collisions in the ATLAS detector far exceeds the rate at which it is practical to store events permanently. The trigger is therefore designed to select interesting events on the fly and only store the most interesting ones.

The trigger system is divided into three levels called level 1 (L1), level 2 (L2), and event filter (EF). The three levels are arranged in a pipeline where every event needs to be accepted by each level before it is recorded to tape. An overview of the layout of the trigger pipeline is provided in figure 5.19. The levels represent increasing sophistication and levels of detail in the decision making.

L1 is a hardware based trigger that is located inside the detector itself. It is able to make decisions based on regions within any one sub-detector only. It has access to a reduced resolution version of the full calorimeters

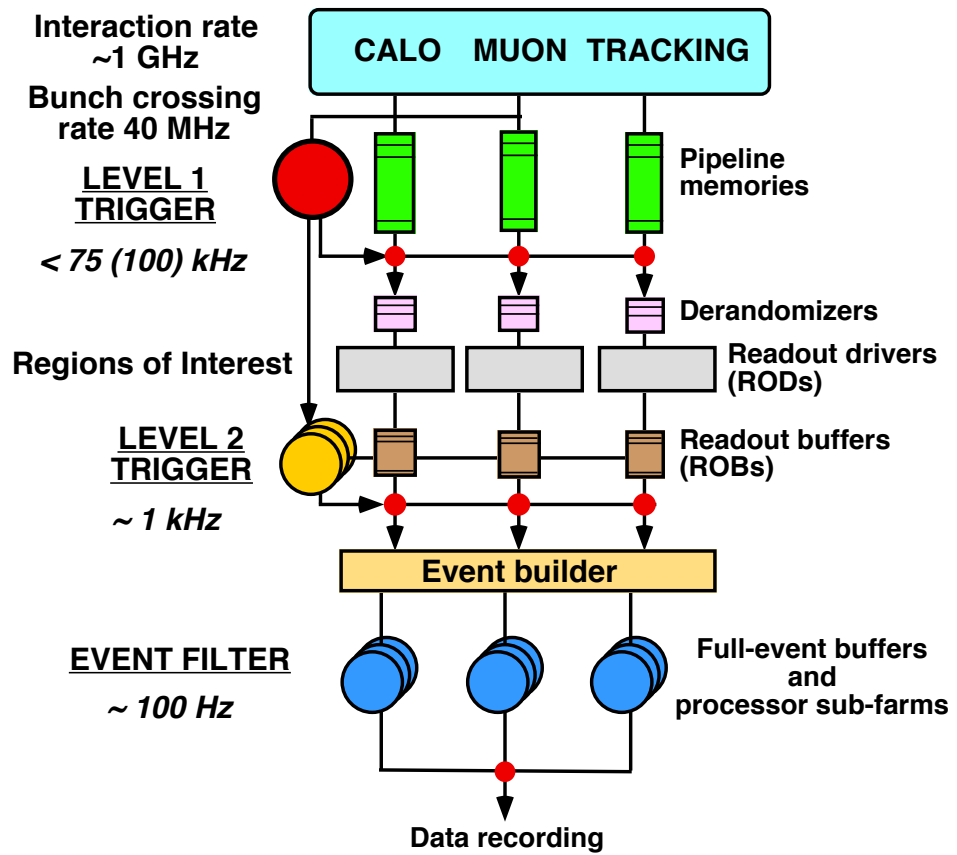


Figure 5.19: Trigger flow. Figure from [56].

and the muon spectrometers. Track reconstruction is not carried out at this stage because of the time required to reconstruct tracks. The L1 decision is made within $2.5\ \mu\text{s}$ and the event rate is reduced from a bunch crossing frequency of 20 MHz to 75 kHz. The L1 trigger is able to recognise rough calorimeter cluster shapes and pass those on to the L2 trigger.

The L2 trigger is run on a computer farm that is located underground next to the ATLAS cavern. The physical proximity reduces delays. L2 is seeded by regions of interest that were identified by the L1 trigger. Around these regions full detector information is accessed and tracks are searched that match with the calorimeter clusters. This enables the L2 to refine the measurement of the object and thereby make a better judgement with tighter cuts. This stage takes 40 ms to complete and reduces the rate further to 3.5 kHz.

At the EF the full event is reconstructed using a slightly optimised version of the standard ATLAS event reconstruction software, called ATHENA. At this level all event information is available including tracking, identification of electrons, muons, and jets, and missing transverse energy measurements. The EF further reduces the event rate to the 100 Hz that are written to tape.

The triggers are controlled via a set of trigger menus that are short descriptions of possible pathways that an event can pass through the pipeline. Thus there are menus for accepting events with muons where the L1 is seeded by a muon chamber until the EF confirms a good hard muon in the event, and there are menus for triggering electrons where an L1 EMCal cluster gets matched to a track at L2 and the event is accepted at the EF, just to mention two examples. The menus are designed to keep the acceptance rates of each trigger level at roughly the rate that was mentioned above. Some run conditions, such as the pile-up (PU) of events within a single bunch crossing, have a large effect on the acceptance rates. Therefore, as run conditions change along a run period or even within a single run, adjustment of the trigger menus becomes necessary. Adjustments are made by applying pre-scaling factors to certain trigger menus such that, say, only every third good EM cluster above 20 GeV gets accepted at a pre-scaling factor of 3. Pre-scaling quickly makes a menu item useless as it essentially reduces the collected data in that channel by the pre-scale factor.

5.9.1 Trigger Pre-scaling

The event rate that each of the L2 and EF trigger farms and the recording system can accept is limited by the computing power available, i.e. the size of the computer farm running the trigger, for the triggers and the number of tape systems for the recording part. As the run conditions change with time the rate of events that are accepted by a trigger level may rise beyond what the next step of the chain can accept as input. This can happen

because of deteriorating detector performance leading to mismeasurement, but mostly it is the result of the ever increasing instantaneous luminosity of the LHC mentioned in section 4.4 and the increasing pile-up associated with this. Pile-Up (PU) is the occurrence of several pp collisions in a single bunch crossing. The relationship between PU and rates of a trigger menu is complex, but is generally an increasing function.

When the acceptance threshold of any step in the trigger chain is met, one risks losing important events. This needs to be prevented. At these times there are two simple options that could be chosen

1. changing the trigger levels
2. pre-scaling a some trigger menus.

It is generally easier to estimate trigger efficiencies when trigger levels are constant with time which is why the first option is not chosen. The pre-scaling of a trigger menu means that at a pre-scaling factor of n , only every n^{th} event that was triggered is actually passed on. High pre-scaling factors are essentially equivalent to turning a trigger menu off. In practice, for every type of trigger menu there is a series of trigger menus with increasing threshold levels. Since pre-scaling is done independently for each menu, pre-scaling the lowest menus is nearly equivalent to changing the levels. The major difference from the point of view of the analysis is that this method makes signal efficiency estimation easier.

5.9.2 Luminosity Counting

When carrying out an analysis where one intends to measure (or set a limit on) a cross-section, it is important to know the total integrated luminosity that was used. This is because while cross-sections are normally thought of as interaction probabilities, at colliders they are measured as event rates per integrated luminosity. The measurement of the instantaneous luminosity delivered by the LHC inside ATLAS is in itself a difficult analysis [57] which is carried out by a special luminosity working group inside the collaboration. This group provides the information in the form of a software tool that is able to calculate the integrated luminosity if given a set of runs and lumi-blocks.

We used only non-pre-scaled triggers in our analysis, which facilitated the luminosity determination considerably. The maximum number of runs and lumi-blocks that we could use in our analysis was restricted by the good-runs list (GRL) that we used (see section 9.1.2). In practice, some computing problems in data preparation restricted us to not use all possible data. We therefore had to form a list that was the intersection between the data that was allowed by the GRL and the data that was actually available to us. The resulting list could be passed to the luminosity counting tool,

providing us with the total luminosity against which our observed counting limits had to be measured.

5.9.3 Data Storage

The data that is recorded by the ATLAS detector is divided into several data-streams based on which triggers were activated by the event. The streams are intended as a first level of event selection based on what type of triggers one is interested in. They are also a book-keeping mechanism as not all streams are equally available for analysis.

There are streams for

- Muon triggers
- e/γ triggers
- E_T^{miss} /jet triggers (calorimeter based, aka. JetTauEtmiss stream)
- debug information

... several others.

Thus an event will be recorded in the muon stream if any of the muon triggers were activated, in the e/γ stream if any electromagnetic triggers were activated etc. If an event has activated triggers of more than one kind, it will be recorded to more than one stream. The debug stream is used to record events that took up too much time to be reconstructed in the EF phase to see what went wrong, what caused them to take so long. This stream is not normally included in the routine reprocessing and is not distributed as widely since it is not normally of interest to analyses.

5.10 Timing in ATLAS

The timing systems of ATLAS had one central design goal: to be able to distinguish which of several subsequent bunch-crossings a hit belongs to. At a design bunch spacing of 25 ns, this set the minimum required time resolution of all detector technologies in ATLAS. Any timing accuracy beyond this elementary requirement was not a priority in the design of the detector. This is the main reason why the timing systems are not at the limit of technological feasibility.

All ATLAS timing is ultimately controlled by beam information from the LHC Radio Frequency (RF) systems. A clock signal which is generated from the RF signal is sent through 14 km of optical fibres to the ATLAS central trigger processor (CTP) where small phase corrections may be applied derived from observed phase differences from a beam pickup 175 m upstream of ATLAS. From the CTP, the timing signal is distributed out to

the local trigger processors of each sub-detector and from there on to the front-end electronics.

Time dependent variations in timing bias can generally be expected to follow this hierarchy. The largest variations are expected to affect all ATLAS systems equally. These offsets could be associated with the ATLAS-LHC interface and could show a bunch-to-bunch variability that is otherwise constant with time, or a gradual drift in time associated to slowly varying quantities such as temperature. Timing offsets within a run may be expected to depend on the bunch ID as a synchronisation signal is received once per beam orbit in addition to the single-bunch signals (see sec. 8.2.3.2 in ref. [47]).

Time-dependent variations between different sub-detectors, the next step of the hierarchy, are expected to be much smaller because of the similar technology and physical environments of the timing distribution systems of different sub-detectors.

5.11 Detector Operation

The data from ATLAS is structured on several levels:

- events
- lumi-blocks
- runs
- run-periods

All data that is associated to the crossing of a pair of proton bunches inside the ATLAS detector is called an event. An event can contain several $p - p$ interactions.

A lumi-block (LB) is the smallest unit of data for which the instantaneous luminosity inside ATLAS can be independently determined at a level of precision where systematic effects outweigh statistical uncertainty. The length of a LB in atlas is of the order of minutes. Lumi blocks are generally the smallest unit of data on which the goodness for analysis is judged.

As already introduced in section 4.4 a run in ATLAS is the same length as a fill of the LHC beams. This can last from a few hours to over 12 hours. During a fill the instantaneous luminosity drops continuously as the individual bunches are blown up by coulomb interactions between colliding bunches. This raises the internal bunch temperature which the LHC has no means of cooling. More spread out bunches lead to lower collision rates as the number density falls. The actual number of protons per bunch is of the order of 10^{11} . Particle losses due to collisions are negligible and do not contribute to the decline of luminosity.

run-period	start date	end date
D	Apr. 14 2011	Apr. 29 2011
E	Apr. 30 2011	May. 3 2011
F	May. 15 2011	May. 25 2011
G	May. 27 2011	Jun. 14 2011
H	Jun. 16 2011	Jun. 28 2011
I	Jul. 13 2011	Jul. 29 2011
J	Jul. 30 2011	Aug. 4 2011
K	Aug. 4 2011	Aug. 22 2011
L	Sep. 7 2011	Oct. 5 2011
M	Oct. 6 2011	Oct. 30 2011

Table 5.1: *The run periods that were used for our analysis.*

Runs are numbered continuously and are identified by their run number. ATLAS also carries out runs in the absence of collisions for the purpose of calibration and checking. This is the reason why the run numbers used in this analysis are not consecutive.

At regular intervals, some features of data-taking change dramatically. This can be the changing of LHC parameters, such as the beam structure, or the changing of ATLAS conditions, such as changing from one TRT gas mixture to another. At these times a new run-period is started to mark the fact that the data conditions can in general be expected to be different.

Run-periods are counted as letters of the alphabet, starting from A each year. The periods that were used for our search are shown in table 5.1. Data taken earlier than Apr. 14 was not used for our analysis because of different detector conditions before this date that made the data less useful for our analysis.

The most notable change from one run-period to another is the event pile-up (PU). PU is the name given to the number of interactions that occur within a single bunch crossing. Increasing PU is a consequence of the increase in instantaneous luminosity delivered by the LHC. Event features that depend on PU are

- E_T^{miss} trigger rates - larger calorimeter occupancy leads to wider E_T^{miss} fluctuations and larger trigger rates even in the absence of real E_T^{miss} .
- candidate isolation - in our search we wanted candidate tracks to be alone in their detector element in order to allow clean measurements. A larger number of tracks in an event reduces the average distance to the next track or jet.

Chapter 6

Techniques

In this chapter I will introduce several of the tools and methods that were used in the main analysis. They are not in themselves part of the physics of the central theme but are nonetheless necessary as background material.

6.1 ATLAS Full Chain

From the point where a particle has struck a detector element in one or several parts of the ATLAS detector to the point where this event can enter into a search, a lot of processing has to be carried out to make the data usable. In this section I will outline the chain of processes that are applied to data before the final distributions can be produced. All software that is used for these steps is collected in a ATLAS's own software package called ATHENA [58]. All the processing steps from reconstruction to analysis objects as well as all the simulation steps involved in MC productions are collectively called the Full Chain.

Chapter 5.9 already described the conditions that have to be met for an event to be recorded to long-term storage. At this point all data streams from all parts of the detector as well as some exterior data on run conditions and timing are written into a data format called Raw Data Object (RDO). The information from the various detectors is at this point organised into C++ objects that are easier to access than the raw streams. The RDOs still do not contain any derived information that can be calculated or reconstructed from the rest of the raw data. This keeps the size of this data format low and means that RDOs do not need to be reprocessed at later times when new versions of the reconstruction software become available.

The next step in the chain is reconstruction. During reconstruction all the hits in the various detectors are read, matched to each other, and combined into physics objects. Tracker hits are combined to tracks and calorimeter hits are combined into clusters. Tracks are matched to clusters to identify certain species of particles such as electrons. Especially the recon-

struction of tracks from the three dimensional tracker hit coordinates is very expensive in terms of computing power.

The fully reconstructed data is stored in a file format called event summary data (ESD). This data format contain all the original hit information of all hits that are associated with physics objects. Hits that are not found to be associated with any physics object are discarded at this stage.

Further refinement steps are available in ATHENA to arrive at so called Analysis Object Data (AOD) format data. This was not used in our analysis. For our purposes we proceeded to produce Derived Physics Data (D3PD) from ESDs. This was needed because we needed access to individual hit information for timing calculations.

6.2 From Collisions to Plots

After we had condensed the data into D3PDs our further analysis was carried out outside ATHENA. D3PDs are in the n-tuple format readable by the ROOT software package [59]. We used distributed analysis methods using PROOF [60] to speed up the considerable computational workload of the final analysis steps.

6.3 Data Samples

Figure 6.1 shows the development of the luminosity delivered by the LHC and recorded by ATLAS as a function of date in 2011. The strong concave form stems from the fact that the accelerator was still being tuned and so instantaneous luminosity was constantly increasing. Since the number of bunches in the accelerator was approximately constant, increased luminosity meant an increasing number of interactions per bunch-crossing, the so-called pile-up (PU). With increasing PU, trigger menus fire at a larger rate. Since the total trigger bandwidth is limited, this increased firing rate needs to be balanced by pre-scaling the lowest trigger menus.

Also for our analysis this meant that we had to use different triggers for different data-periods if we wanted to always use the most efficient, i.e. lowest, available un-pre-scaled trigger. This can be seen in table 6.1.

6.4 Triggering

All events that enter our analysis will necessarily have passed at least one trigger since otherwise they would not be recorded and available to us. Understanding trigger effects on signal was an important part of our analysis. It allows us to determine the efficiency of the trigger, i.e. the chance that an event will be triggered if a signal was present. This is in turn necessary in

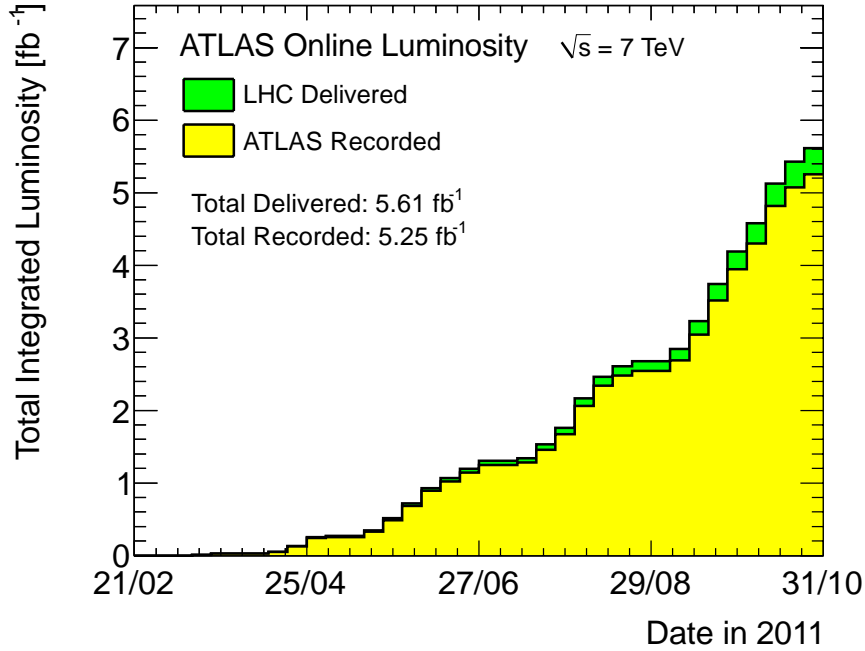


Figure 6.1: The integrated collected luminosity as a function of date in 2011. The high data taking efficiency of ATLAS is apparent from the smallness of the green band.

Trigger by period	D	E	F	G	H	I	J	K	L	M
EF_xe60_noMu	x	x	x	x	x	x				
EF_xe60_tight_noMu							x	x		
EF_xe60_verytight_noMu									x	x
EF_xe70_noMu	x	x	x	x	x	x	x	x	x	-
EF_mu18	x	x	x	x	x	x				
EF_mu18_MG	x	x	x	x	x	x				
EF_mu18_medium							x	x	x	x
EF_mu18_MG_medium							x	x	x	x

Table 6.1: Trigger menus utilised in this analysis along with an indication in which data taking periods they were used.

order to quantify the discovery potential and to set cross-section limits in the absence of signal.

In order to be able to detect any kind of signal, we first need to make sure that the events that contain the signal are not being discarded already at the triggering stage. As described in section 5.9, the trigger is constructed in three layers of increasing sophistication and each level, Level 1 (L1), Level 2 (L2) and the event filter (EF) need to accept an event for it to be recorded to permanent storage. Because of the speed requirements, only limited local object information is available at L1, detailed object local information is available at L2 and full reconstruction is only carried out at the EF. In order to detect SMPs, two different triggering strategies were utilised. One of them relied on missing transverse energy (E_T^{miss}), the other relied on triggering on muon like objects.

6.4.1 E_T^{miss} Trigger

As mentioned in section 4.3 the longitudinal boost of the collision centre of mass is not fixed at hadron colliders. The total transverse momentum (p_T) of the incoming beams however is known to be very small. If any imbalance is detected in the sum of all secondary particle momenta, this is therefore a strong indicator that something has been missed. This may indicate the presence of neutrinos or DM candidates in an event and is therefore used at the LHC as a trigger in other searches. Since tracks are not reconstructed at L1, only the calorimeter information is summed to arrive at a first measure of E_T^{miss} . The amount of energy that is deposited in the calorimeters by a charged SMP has been studied with the help of MC samples and been found to not exceed 40 GeV. Hence the E_T sum from which E_T^{miss} is calculated at L1 would not include the majority of the SMPs energy. A single SMP would therefore lead to a clear E_T^{miss} signal that could easily be triggered on. There is a further complication though. As described in section 3.2, SMPs are expected to be produced in pairs. In an ordinary 2 to 2 process, the final particles will be back-to-back in the centre of mass frame of the collision. This completely removes any E_T^{miss} signal unless the centre of mass has a transverse boost. Once the effects of ISR have been included however, transverse boosts of the hard collision frame are observed as the collision frame recoils against the partons emitted from the incoming particles. This feature makes it possible to use the E_T^{miss} trigger for R -hadron searches.

How well the E_T^{miss} trigger matches between data and MC was evaluated using the calibration sample. Muons from $Z \rightarrow \mu\mu$ are invisible to the calorimeter based E_T^{miss} trigger and thus these events display many of the same characteristics as R -hadron events. Figure 6.2 shows the turn-on curve of the E_T^{miss} trigger as a function of the offline reconstructed E_T^{miss} . The good match between data and MC shows the quality of the simulation.

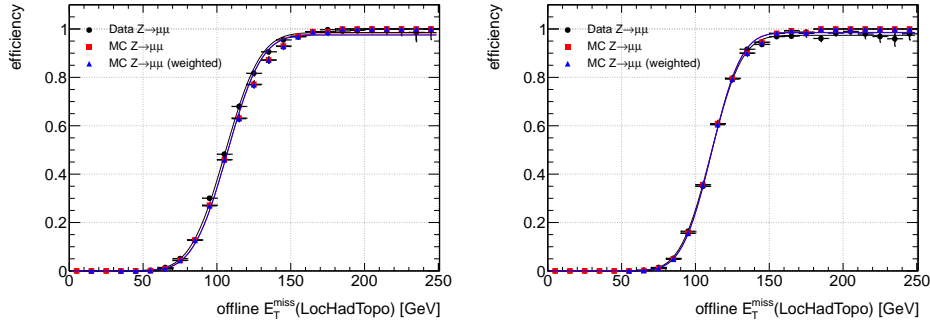


Figure 6.2: Turn-on curve for the *xe60_verytight_noMu* (left) and *xe70_noMu* (right) trigger chain in $Z \rightarrow \mu\mu$ data (black dots) and in MC, before (red squares) and after (blue triangles) pile-up re-weighting.

6.4.2 Muon Trigger

The other triggering strategy relied directly on the presence of a muon-like object. As mentioned in section 5.8 the muon spectrometer is equipped with fast trigger detectors in the form of RPCs and TGCs that are able to provide a signal in time for the L1 trigger. The challenge in this trigger is that the L1 trigger needs to make a decision within 100 bunch crossing times, i.e. $2.5 \mu\text{s}$. The slowest SMPs will at this point not even have reached the RPCs and can thus never trigger an event. This provides a cutoff in β values below which SMPs cannot reach the trigger chambers in time to cause an event to be accepted by the L1 trigger. This cutoff was found to be at about $\beta = 0.63$. SMPs below this speed can still be reconstructed, since the readout window of the MDTs is much longer. Figure 6.3 shows the trigger acceptance of the muon trigger on simulated samples of stau sleptons.

There is ongoing development of a low level slow muon trigger that would provide a much higher trigger efficiency than the present trigger options available to our search. Unfortunately this work was not yet mature enough to be included in our analysis.

6.5 Monte Carlo Simulation

The data that is obtained from the ATLAS detector is the result of a multitude of different effects. Some effects are related to the underlying physics of the collision process that we are trying to study, while others are merely the effect of the detector. Through limited acceptance or varying sensitivity these detector effects can significantly skew or even cover underlying physical effects. It is often not possible to measure every detector effect directly or to disentangle it from the data to expose the underlying physics. Because of this, analyses in high energy physics often rely on simulations.

Simulations are intended to model all effects that affect the data, thus

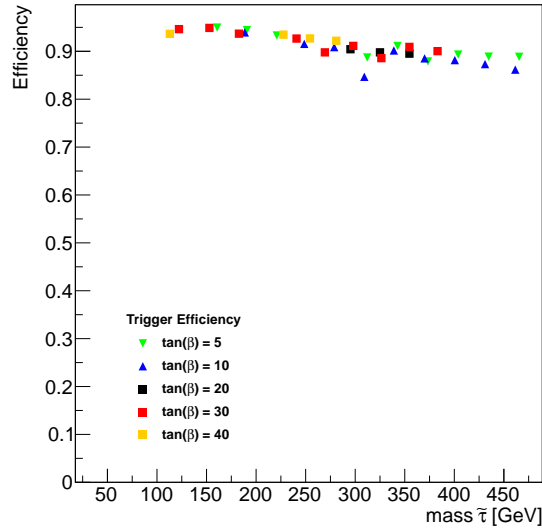


Figure 6.3: Efficiency of the muon trigger for GMSB events as a function of $\tilde{\tau}$ mass

allowing a direct comparison of simulated and real data. Any discrepancies between the two are signs of unaccounted effects which may be rooted in inaccuracies in the detector simulation, or may be caused by new physics.

One essential mathematical tool in these simulations is the Monte Carlo (MC) method. This method allows the generation of random numbers, that follow distributions for which no analytical form is known, by repeatedly drawing uniform random numbers on the interval $[0, 1)$ and applying certain operations on them. This method gives the name for all simulations and simulated data in particle physics, both of which are often simply referred to as MC.

In the case of LHC collisions at ATLAS the simulation process is split up into several stages:

1. A generator (in our case PYTHIA [15]) is used to select which hard process will take place in the primary collision. The identity and kinetic properties of the products of the hard interaction are chosen as random variables by the Monte Carlo method. PYTHIA makes sure that the collision products behave as predicted by the specific model, be it the SM, SUSY or otherwise.
2. Any coloured products are hadronised into showers of colourless states. This process is also simulated by PYTHIA according to the Lund String Model [14].
3. The resulting products are now considered to emerge from the inter-

action point and begin their passage through the detector. This stage is handled by GEANT4 [61, 62]. Each particle is propagated through a detailed model of the ATLAS detector where after every small step a decision is made via the MC method about which possible process the particle should undergo next. Possibilities include spontaneous decay, ionisation, nuclear interactions or free propagation. In this way higher features, such as showers, are seen to emerge from the underlying mechanics.

4. After all particles' paths have been determined, the response of the detector electronics to the resulting signals is modelled. It is at this stage that effects like timing errors or offsets are introduced. The magnitudes of such errors are chosen to match observations.

Once all these steps have been completed, the resulting MC data is stored in the same format as recorded data. From there the MC data can be processed by the same software suite as is used for real data. In addition to all reconstructed variables, such as particle energies etc. MC samples also carry along information from the simulated parton level interaction. This information, called “truth”, can later be used to verify the reconstruction algorithms by checking, for example reconstructed energy against truth energy of a particle.

We did not have any truth information about processes that happened outside the interaction region, i.e. from the GEANT4 stage where R -hadron interaction types, charge-flip etc. are determined. Because of this, we were not able to investigate the use of charge-flip as a signal discriminator. This lack in our simulation software would enable new searches if it were addressed.

6.5.1 MC samples

The generation of MC events requires a lot of computing power. The number of MC events that can be generated for an analysis is limited mainly by the available computing resources. This has many consequences.

Background

As described in section 4.3.2 the total cross-section of proton interactions is many orders of magnitude larger than the cross-section of interesting physics. Most of the cross-section will immediately be rejected by the trigger. When producing MC samples it would be very wasteful to generate many events that have no chance of passing the trigger. Because of this MC samples are typically created with only a few processes enabled, and with certain cuts on the parton level collision products before the full event simulation is carried out. Great care is taken at this stage to choose cuts that affect the final distributions as little as possible.

SMP	interaction model	production channel	masses
\tilde{g}	generic	gg	100 to 1500 GeV
\tilde{g}	generic	$f\bar{f}$	100 to 1500 GeV
\tilde{g}	Regge	gg	100, 300, 500, 700 & 1100 to 1500 GeV
\tilde{g}	interm.	gg	100, 300, 500, 700 & 1100 to 1500 GeV
\tilde{t}	generic	all	100 to 500 GeV
\tilde{t}	Regge	all	100 to 1000 GeV
\tilde{b}	Regge	all	100 to 1000 GeV

Table 6.2: *The available R-hadron signal samples in our analysis. The samples differ in the supersymmetric species contained in the R-hadrons (SMP). Effects of the the interaction model (generic, Regge or intermediate) were not investigated as they were previously found to be small [7]. The production channel determines the η distribution. All mass ranges are in steps of 100 GeV.*

In our analysis we were hunting for rare outliers and mismeasurements. Given the very good efficiency at rejecting background, we would have had to generate very large samples of MC events to get good estimates of the background in our signal region. Generator level cuts would be of no help in this endeavour since the mismeasurements only occur at the detection stage after the particles are generated and propagated through the detector. This is why we relied on a data-driven background estimation method as explained in later sections.

We did attempt to use MC background to verify data driven approach that is described below. What we found though, was that MC background is entirely unable to describe real data even in a signal free sideband region. The idea of using MC to generate background was thus discarded.

Signal

In order to train our search cuts and to evaluate the efficiency for selecting signal events we needed samples of MC simulated signal events. In these events only the pair production of coloured heavy particles of various masses was allowed as a possible interaction in the simulation of the primary interaction so that every event contained a pair of R -hadrons. After production and hadronisation of the R -hadrons, their detector interactions were simulated according to several different models in different samples. The samples that were available to us are presented in table 6.2.

At the time of our analysis truth information was passed on from the event generator stage only (i.e. PYTHIA), and no truth information was available about the detector interactions. Especially charge-flipping inter-

data periods	fraction of MC	integrated luminosity	fraction of Data	correcting weight
B-D	3.2%	166.65 pb ⁻¹	3.5%	1.106
E-H	17.4%	948.576 pb ⁻¹	20.2%	1.158
I-K	25.8%	1154.3 pb ⁻¹	24.6%	0.950
L-M	53.5%	2431.74 pb ⁻¹	51.7%	0.965

Table 6.3: *Fraction of data and corresponding MC for each run period group.*

actions, as mentioned in section 3.4.2, would be important to know about. Extending the event generation process to include this information is one of the possible ways of extending this analysis.

The production of signal samples was carried out in parallel with the development of our analysis. The range of masses and interaction models that were chosen for the samples were based on experiences from earlier publications.

6.5.2 Pile-up Re-weighting

In section 5.11 we introduced the concept of pile-up and changing detector conditions. When simulating data with the MC method, these conditions as well as their history of change should form part of the input to the simulations. In practice, the MC simulations were carried out some time before the end of the data taking period, and thus the full set of conditions were not yet known. It was possible however to estimate how much data could be expected to be taken with each set of conditions. The MC simulations were thus carried out with these estimated conditions as input.

All MC samples were split up into four run period groups as shown in table 6.3. The fraction of events simulated for each run period group did not match precisely the fraction of data collected in the period. In order to make all conditions match as precisely as possible between MC and data, the available MC events were weighted as shown in table 6.3 so that the total fraction coming from each run period group was correct between MC and data.

The triggering is the major factor that is being influenced by PU for our analysis. Since MC was not split up further than by run period group, it was at this granularity that the triggers were chosen. This is reflected in table 6.1.

6.6 Calibration Samples

For the calibration procedures that formed part of our analysis we needed clean particle tracks that passed through the calorimeters and muon spectrometers. The calorimeters are designed to stop all particles except muons. Therefore muons are the obvious choice as calibration particles.

While secondary muons can be created by a range of processes, such as decays of tauons or pions, hard primary muons are mostly created by Drell-Yan production and Z^0 mediated production. To identify muons, all MS tracks can be used if they can be matched to an ID track segment, so-called combined muons. The purity can further be refined by requiring a pair of muons whose invariant mass is close to the know Z^0 -mass.

For our calibration we used the recommendations from the ATLAS muon combined performance group to select good, clean muons. This includes requirements on the number of good hits in the inner detector and goodness of the combined fit. In addition, we required the following

- that the track not share any pixel hits with other tracks,
- the ΔR to any other track be at least 0.25,
- the ΔR to any found jet be at least 0.3,
- the invariant mass with the highest p_T muon of opposite charge had to be within 5 GeV of the known Z^0 mass. This other muon also had to pass a number of rudimentary cuts such as $p_T > 10$ GeV.
- the impact parameters had to be small, the track had to pass within 10 mm in z and 2 mm in r from the primary vertex.

The additional isolation requirements meant that the cells hit by the track were not also hit by any other identified particles, giving a cleaner signal. The impact parameter cuts remove cosmic muons which can arrive at random times and skew the timing distribution.

We applied these selection cuts to a pre-selected $Z \rightarrow \mu\mu$ data stream and obtained a sample of muons covering the same run-periods as used in our analysis. This sample of muons will be referred to as the calibration sample in chapter 7.

The detector interactions of R -hadrons may be different from muons, so in order to test the robustness of our calibration, we also selected a sample of hadron tracks from jets. These tracks had to pass similar quality requirements as the muons except that the selection was optimised to reject muons. This sample will later be referred to as the jet sample.

The calibration turned out to be very insensitive to the difference between muon and jet interactions. Figure 6.4 shows the calorimeter β distributions obtained from a sample of simulated 800 GeV R -hadrons using both muon and jet calibration. The distributions are in good agreement. The similarity between the two calibration samples is also reflected in the fact that the resulting calibration constants are largely similar.

The similarity in calibrations from jets and muons means that the precise value of the muon selection cuts is not critical as long as the muon purity can be said to be high.

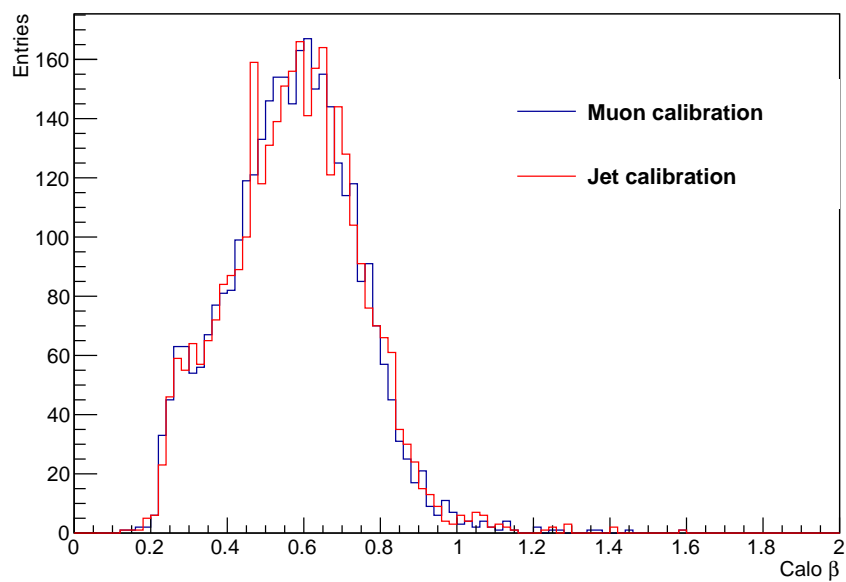


Figure 6.4: The β distribution for 800 GeV R-hadrons measured with the calorimeter using muons (blue) and jets (red) for the calibration. The distributions are in good agreement.

Chapter 7

Detector calibration

7.1 Motivation

The search for stable massive particles rests on mass measurements via two types of fundamentally different measurements of the particle speed. One of them is the direct measurement of the time of flight (ToF) of the particles from the interaction point to the detector elements. The other is a measurement of the $\beta\gamma$ via its known correlation with the specific ionisation loss of a track. Each of these speed measurements can be combined with the track momentum, measured by the track's magnetic deflection, to give a mass measurement.

Neither of these measurements are normally required in standard ATLAS analyses. Therefore centralised calibration is not carried out on these estimators as it is on many other aspects of ATLAS data such as geometric alignment and calorimeter energy resolution. In the case of the pixel detector, another group within our collaboration had previously carried out a detailed calibration of the curve that converts dE/dx to $\beta\gamma$ for an R -hadron search that was purely based on the pixel detector [4]. We were able to make use of their work, but still needed to apply it to data ourselves. An overview of this calibration procedure is given in section 7.2.

For the estimate of β from ToF measurements, no previous calibration existed in ATLAS and we had to devise our own calibration scheme. This is described in detail in section 7.3.

The reasons why timing calibration was necessary can be split into two parts. For one thing we needed to align MC timings with data, and secondly, we were hoping that by eliminating local biases the overall spread of the time measurements could be reduced. Both reasons are illustrated in figures 7.1, 7.2 and 7.3.

Shown are the distributions of the raw timings of all detector elements for the calorimeters and the muon spectrometer RPC and MDT chambers respectively. What can clearly be seen is that the timing distributions between

Calorimeter timings

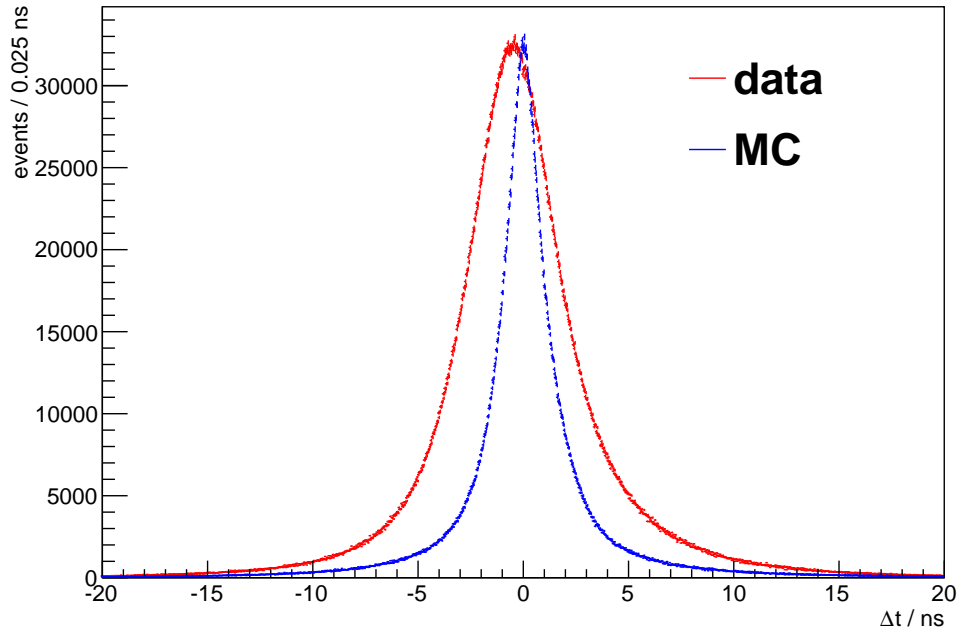


Figure 7.1: *The distribution of deviations from the expected hit time for all calorimeter cells for the calibration sample. The MC distribution has been scaled to have the same maximum as the data distribution. Error-bars are included.*

data and MC do not agree at all. Particularly in figure 7.2 structure can be seen which might be eliminated by suitable calibration.

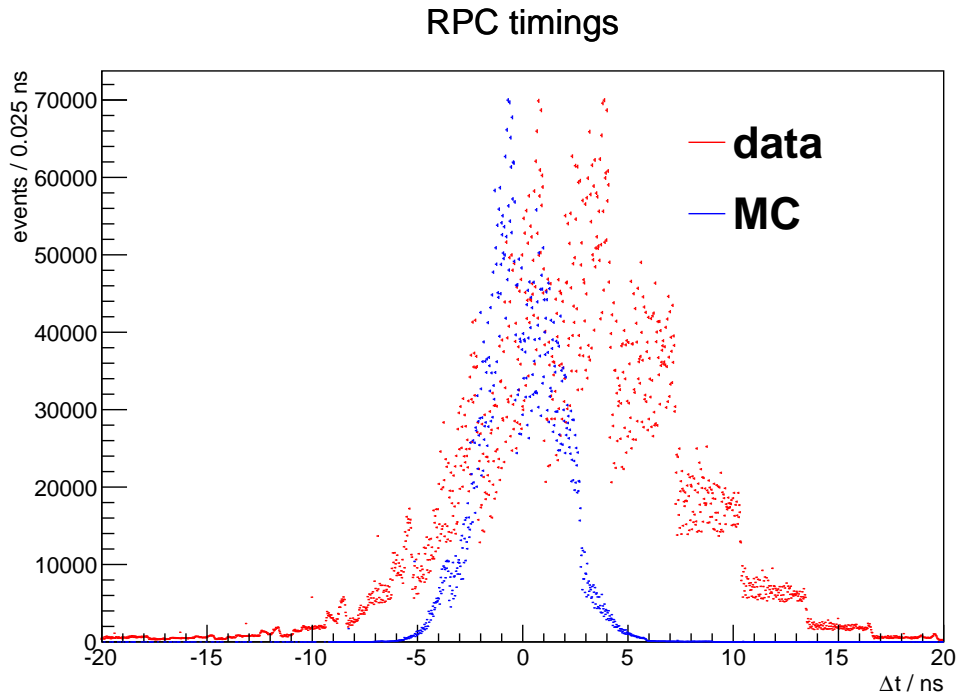


Figure 7.2: The distribution of deviations from the expected hit time for all RPC chambers for the calibration sample. Otherwise as in figure 7.1.

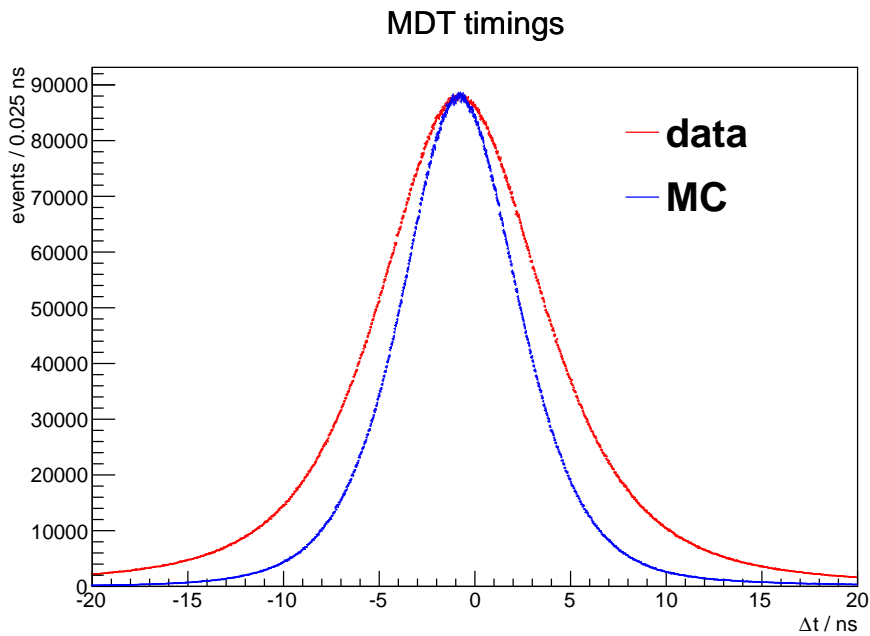


Figure 7.3: The distribution of deviations from the expected hit time for all MDT chambers for the calibration sample. Otherwise as in figure 7.1.

7.2 dE/dx to $\beta\gamma$ Calibration

The conversion between the measured pixel dE/dx and the particles $\beta\gamma$ values was carried out by numerically inverting an empirical Bethe-Bloch curve. The parametrisation used was

$$\mathcal{M}_{dE/dx}(\beta) = \frac{p_1}{\beta^{p_3}} \ln(1 + (p_2\beta\gamma)^{p_5}) - p_4 \quad (7.1)$$

where $\mathcal{M}_{dE/dx}(\beta)$ is the most probable value of dE/dx for a given β and p_i are five free parameters.

The values of the parameters were found separately for each number of available clusters on a track and for positive and negative momentum tracks. The values were found by carrying out a large fit of the data shown in figure 5.6. In each of several slices in momentum the data was assumed to consist of three species, protons, kaons and pions. The distribution of the measured dE/dx in each slice was fitted as the sum of three crystal ball¹ functions where the peaks of the crystal balls in all slices simultaneously had to adhere to equation 7.1.

The pixel dE/dx response to tracks was very well simulated in MC. Nonetheless there were small differences in the empirical Bethe-Bloch fit for data and MC. Therefore the fitting scheme above was carried out for data and MC separately.

The result of this calibration was monitored continuously by observing the reconstructed proton mass that was given by this method. Figure 7.4 shows the measured proton mass for the run-periods in 2011. The good agreement between the measurements and the known proton mass demonstrates the viability of this method.

7.3 Time-of-Flight to β Calibration

The goal of this calibration was to reduce the spread of reconstructed β for calibration muons as much as possible, as well as quantifying the precision of each timing measurement. Since our signal region is at low β , a narrower distribution from SM particles directly means less background at low β .

The primary observables of the Time-of Flight (ToF) measurement is the time tag on a specific detector element. Together with a known distance from the interaction point the time tag gives a particle speed, which can be combined with the measured momentum to obtain a mass measurement.

This seemingly simple measurement has a large number of complications that stem mostly from the fact that ToF measurements were not a primary concern in the construction of the ATLAS detector. The sources of error

¹A crystal ball function is a gaussian with a smooth transition to a power law tail first used by the Crystal Ball collaboration [63].

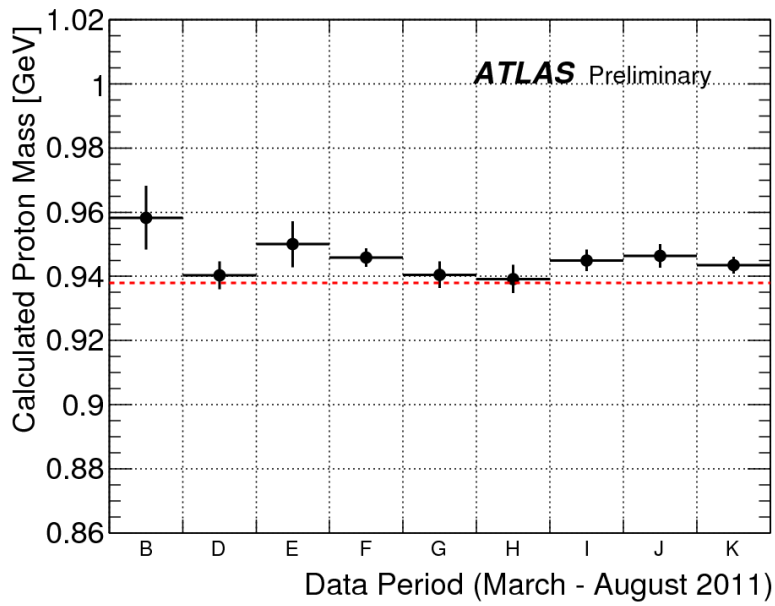


Figure 7.4: This plot shows the proton mass as measured via the dE/dx method by the pixel detector plotted as a function of run-period. The nominal proton mass is shown as the red dashed line. The stability demonstrates the viability of a mass measurement with the pixel detector. Figure from [4].

can be divided into those affecting the measurement of distance and those affecting the measured ToF.

The distance was taken as the Euclidian distance between the interaction point and the centre of the detector element in question. The approximations involved in this will be discussed in section 7.3.1. The geometry required no calibration as it is already thoroughly monitored and calibrated for tracking and momentum resolution.

The calibration of the measured times has two related aspects. One is the removal of measurement biases and the other is the determination of expected errors. The latter were needed as weights for creating the weighted average as a way of combining the individual hits into a single measure of β .

I will start this section by discussing the various sources of geometric and timing errors before proceeding to give a detailed account of the calibration procedures that we carried out.

7.3.1 Geometric Errors

The traversed distance starts at the interaction point, passes through the magnetic field and ends at the point at which the time measurement is taken. All of these have uncertainties associated with them.

The vertex

The point at which the SMP was formed is called a vertex. It is the position where two partons, each one coming from a proton from one of the beams interact to create two LLPs in a hard process. Other particles may also be created, such as, for example, initial state radiation (ISR) or final state radiation (FSR). As described in section 5.11, there will be a number of such collisions in a single bunch crossing, all of which are happening almost at the same time. The positions of the interaction vertices are obtained from the observed tracks as those loci where several tracks converge. Most reconstructed tracks can be uniquely identified as belonging to one of these vertices. Figure 7.5 shows how the vertices are distributed in an example collision.

The vertex that has the highest sum of the squared transverse momenta of all its tracks is called the primary vertex. Because of the very large difference between the total cross-section and the cross-section of hard processes, the primary vertex is virtually always also the one that the interesting particles in an event are associated to. Because of the geometry of the beams, the interaction vertices all occur along a line as in the example figure 7.5. The region where these vertices appear is called the beam crossing point. This point will generally be stable within a run, but can change from run to run as the accelerator magnets are tuned for collisions in each run. In

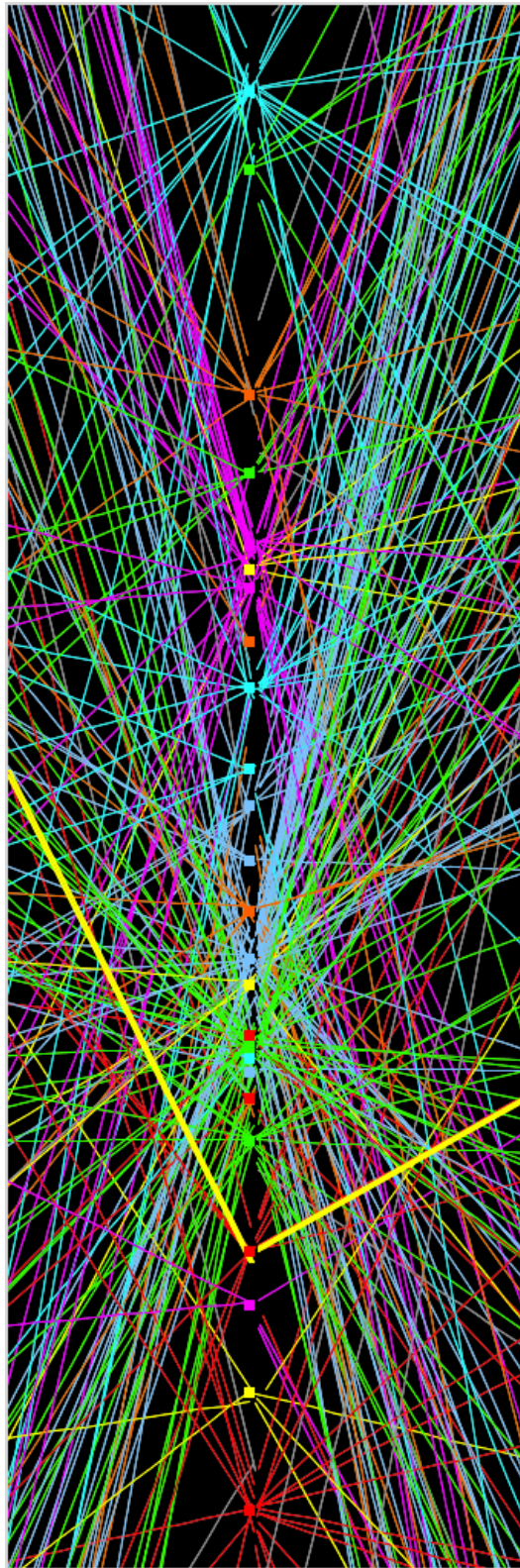


Figure 7.5: An example event with a high number of pile-up vertices viewed in the $y - z$ plane. Shown is the interaction region only. The horizontal size of the interaction region is about 7 cm

particular, it is not guaranteed to lie at the centre of the ATLAS detector, which is conventionally used as the origin of the coordinate system, although it is generally close to it.

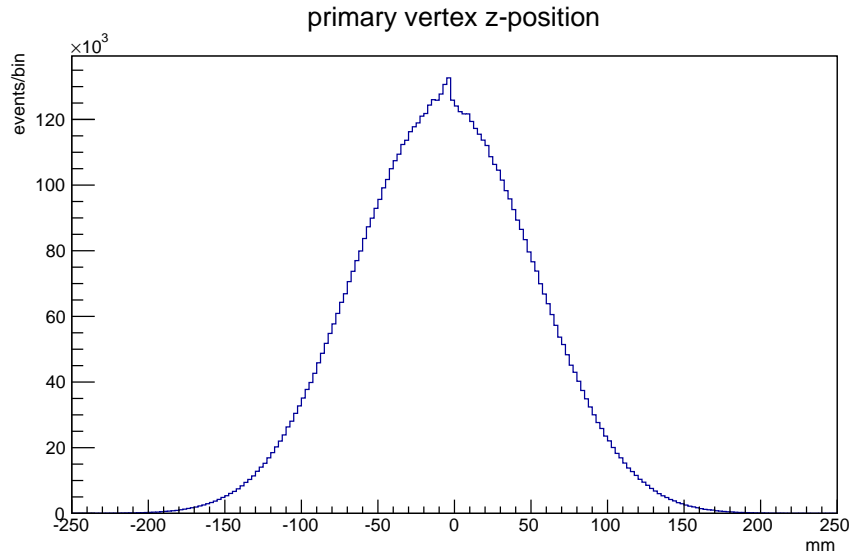


Figure 7.6: The z -positions of primary vertices in good events in the *JetTauEtMiss* stream.

The z -location of the primary vertex for all good events from the *JetTauEtMiss* is shown in figure 7.6. In the x and y directions the distribution is much narrower, with a width of just a few tens of micrometers. These plots can be seen in the appendix, figures A.1 and A.2. The z -location has a mean deviation from 0 of 56 mm. The typical arm-length of a ToF measurement is between the interaction point and the calorimeters of the muon spectrometers, where the time of arrival is measured. The shortest distance to the LAr calorimeter is 1400 mm at $\eta = 0$ (2280 mm to the tile calorimeter). This is thus the case for which uncertainties in the x and y location of the vertex have a maximal relative effect on the measurement. The largest effect of the z -uncertainty is reached at the edge of our measurement window at $\eta = 2.5$ where the distance between the origin and the calorimeters is about 6 m.

We can thus see that in the most extreme cases the assumption of the primary vertex at the origin leads to an error of about 1.7% in the forward region and less than 0.1% near $\eta = 0$. This error was expected to have a small effect on our measurement and was ignored for the sake of simplifying the calculations. The primary vertex position was taken to be at the origin for in all our analyses.

Flight path

In all our timing calibration and analysis code flight distances were taken to be the straight line path between the start and the end of the assumed path. This is of course not entirely valid since all particles that we studied are charged and their paths are therefore bent by the magnetic fields of the detector. As described in section 5.2 the magnetic field in ATLAS is solenoidal in the central tracker and toroidal in the outer muon spectrometer. The deflection of a relativistic particle in a magnetic field can be described by the following expression.

$$BR = \frac{p}{q} \quad (7.2)$$

where B is the strength of the magnetic field, p is the momentum of the particle, q is its charge and R is the radius of the circular path along which the particle moves. At a field strength of 2 T and a particle momentum of, say, 300 GeV this leads to a radius of curvature of about 500 m. At a distance to the calorimeters of about 1.5 m in the transverse plane the difference between the curved path and the straight line is about 6×10^{-7} m.

All particles used for calibration in our analysis were required to have a transverse momentum of at least 10 GeV of momentum. At this momentum the difference in path length is still at the 1 per mille level. Hence the straight line approximation is very good and was used throughout this analysis.

Geometry accuracy

The positions of all detector elements is known to very high accuracy. This is especially true of the tracker where displaced measurements directly translate to mis-measured curvatures, but also the positions of calorimeter elements are measured from data in a process called alignment. Hence the only geometric uncertainty that might be associated with the determination of the end point of a path is uncertainty about where in the detector element the measurement was taken.

Muon RPC and MDT the detector elements are a very constant distance away from the IP over their entire volume. Therefore the error made by using only the centre of the detector element as the end-point of the path is negligible when compared to other sources of uncertainty.

Calorimeter cells, on the other hand, are quite large. The difference in distance between the inner and outer edge of the second layer of the tile calorimeter is 32% of the mean distance. It is assumed that an ionising particle that traverses a cell will ionise along its entire path through the cell and will lead to the same average signal shape independent of the time offset. The absolute error made by using the cell centre is thus a constant bias which will be eliminated in the calibration procedure.

The detector element centre was therefore used as the track end-point throughout this analysis.

7.3.2 Timing Errors

There are two times that enter the measurement of the Time of Flight. The start time and the end time. The start time is naturally the time of the collision. The end time is when the electronic signal is registered against an electronic clock.

Collision Time

The entire LHC accelerator and all detectors were designed for a 25 ns bunch spacing, i.e. for 40 million collisions per second. In all 2011-data which was used for this analysis however, all bunch spacings were at least 50 ns.

Section 5.10 already explained the timing system in some detail. The time origin in each event is taken from a synchronising pulse from the LHC. In practice there may be biases associated with these pulses on several time scales:

- a constant offset may appear from run to run due to slow changes.
- a drifts in timing may be noticeable within a run.
- faster drifts may be observed within one beam revolution which is reset after each orbit by the additional synchronisation signal.

Figure 7.7 shows the variation of the average time delays in calorimeter hits from run to run. A significant variation can be seen. This variation is thought to be the result of drifts in the time alignment between ATLAS and LHC.

Figure 7.8 shows the calorimeter timing variations within run 189425. No clear trends were seen for timing within runs or as a function of the bunch index and we did not calibrate for such variations.

Detection Time

The time at which the arrival of the particle was detected in each part of the detector is the main quantity from which the beta measurement is derived. It is also the quantity to which we are applying all our corrections and calibrations. Its uncertainty stems from a number of factors such as the synchronisation of the detector part, signal delays, and sampling rate. These effects can all be local to the particular cell or common to a section or a whole sub-detector. Also, the effects can all be stable or vary from run to run.

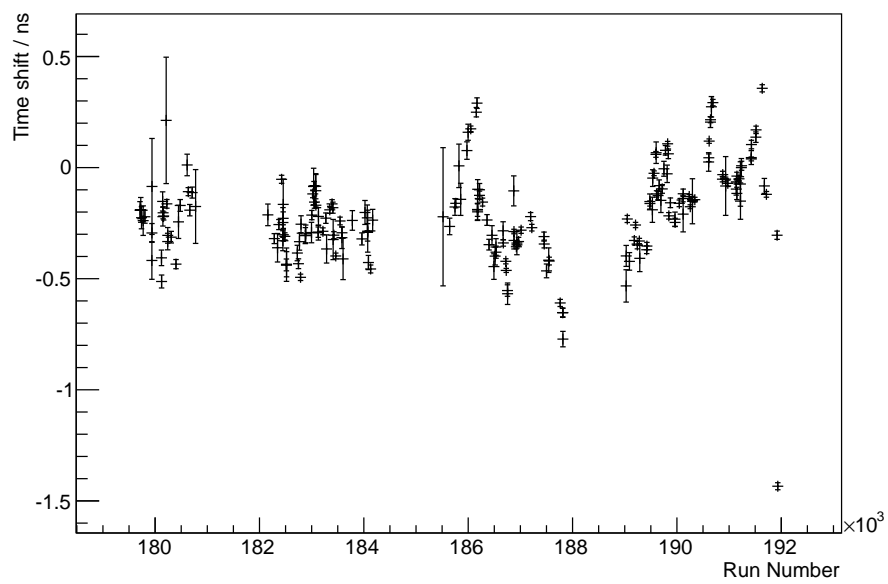


Figure 7.7: The run-average of all uncalibrated calorimeter Δt plotted as a function of run number in the calibration sample.

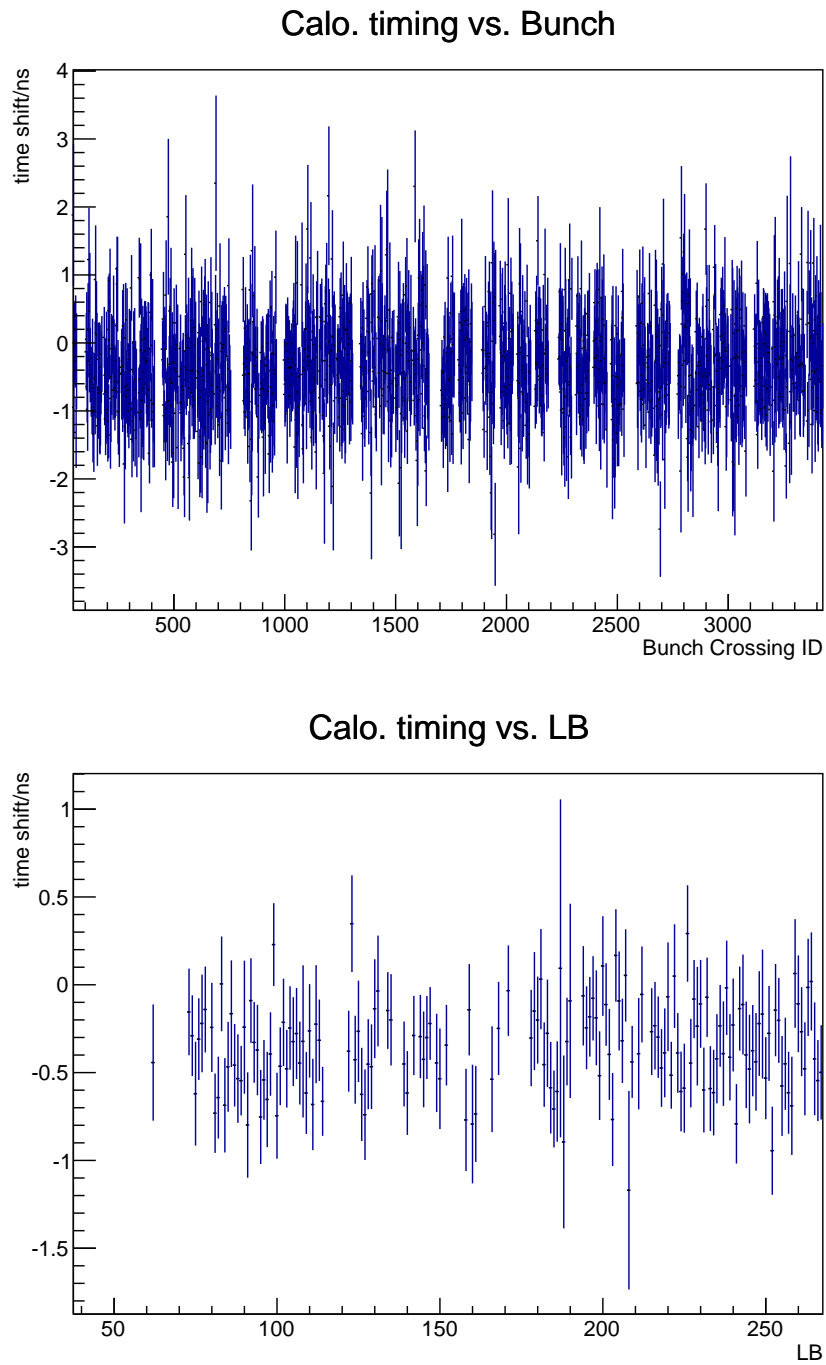


Figure 7.8: *The variation of all uncalibrated calorimeter detection Δt in run number 189425 in period L. No clear trend can be seen in either the variation between different bunches (top) or in change from one lumi-block to another (bottom). These two dimensions were not used in calibration.*

7.3.3 Calibration Overview

Calibration of the calorimeters was carried out in the following sequence which is also illustrated in the flow chart in figure 7.9. Each step will be motivated in the following sections.

1. For each run all hit time measurements were combined into a single distribution. The mean of this distribution was taken as the run-dependent time offset between LHC and ATLAS and was subtracted from the time measurements on a run-by-run basis. This step was completed before any other calibration distributions were created.
2. The calorimeter cell hits were binned by calorimeter layer and by cell energy deposit. At this stage times are measured relative to the expected arrival time of a speed-of-light particle. In each bin the time distribution was formed. The mean of this distribution was subsequently subtracted from the hits in the bin. This removed any detector layer or energy deposit dependent bias. Since hit times in MC were found to be less spread than in data, the MC spread was adjusted by adding additional smearing in the form of a normal distributed random variable with width $\sqrt{\text{width}_{\text{data}}^2 - \text{width}_{\text{MC}}^2}$. Finally the width of the distribution was assigned to each time in it as the expected error.
3. Next the combined calorimeter β measurement was formed. For this each hit was converted to a β^{-1} estimate as $\beta^{-1} = t/d$ where t and d are hit-time and distance respectively. (The hit-time has had the speed of light arrival time added again here.) The error on each estimate is calculated as $\sigma_{\beta^{-1}} = \text{width}_t/d$. The combination is done by weighting each contribution with the inverse square of its error. β is calculated as the inverse of this weighted average with an error of

$$\sigma_{\beta} = \frac{\sigma_{\beta^{-1}}}{(\beta^{-1})^2} \quad (7.3)$$

4. In the final step, the pull distribution of the β measurements was formed, i.e. the distribution of $(\beta - 1)/\sigma_{\beta}$, as a function of $|\eta|$ and β . Such a distribution should always have unit width if the error estimate is correct. Since the widths were not found to be unity, all σ_{β} were rescaled to make the pull distributions match.

All calibration distributions were formed by looping over the entire calibration data-set after all previous steps had been applied.

The calibration of the MS chambers proceeded in a similar sequence. The difference between the Muon spectrometer and calorimeter calibration are in the way that the hits are binned. For MS calibration approximately 1000 pairs of constants are used for the MDT and 34000 pairs of constants

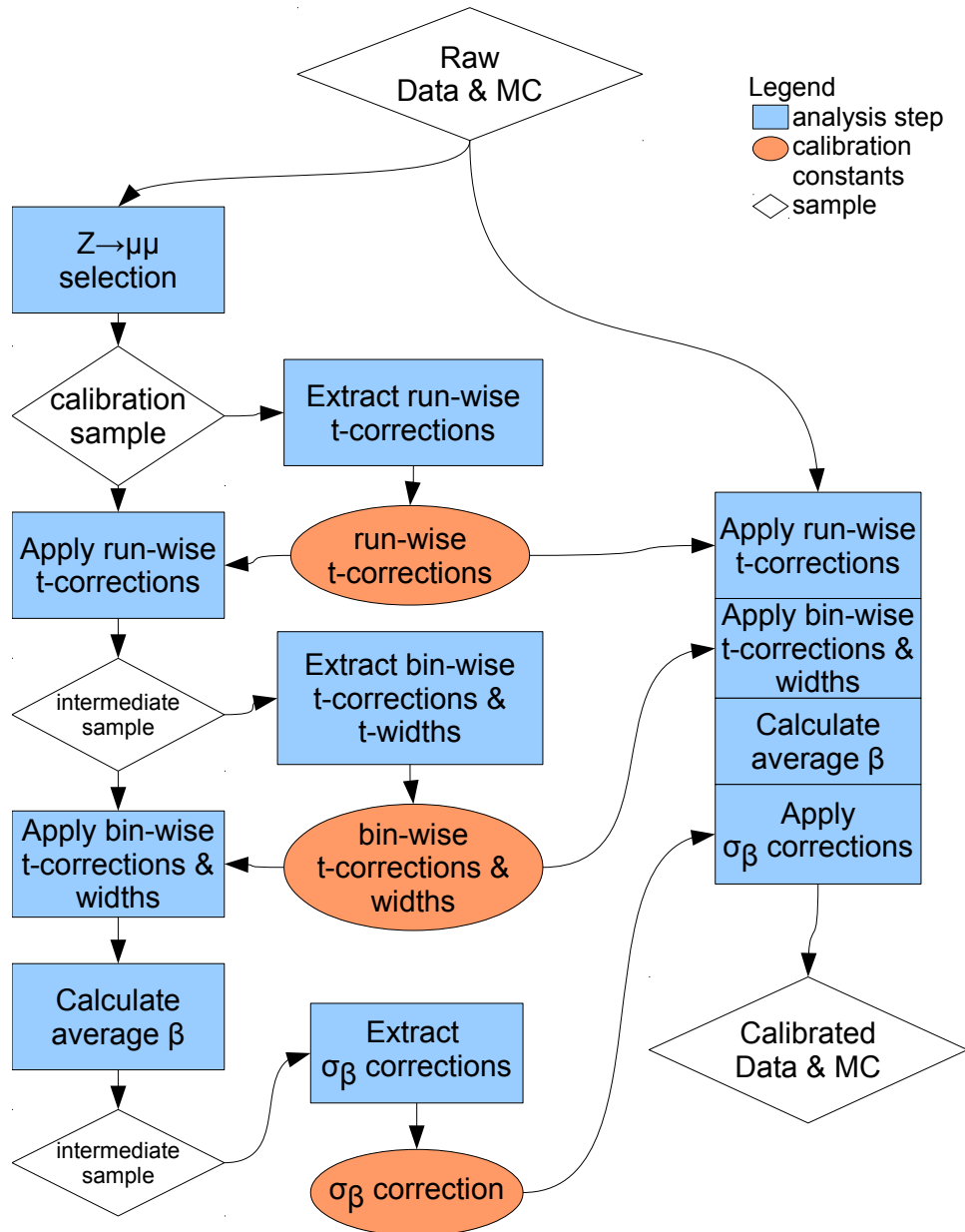


Figure 7.9: The outline of the calibration procedure. The procedure is tightly coupled with the β combination strategy described in section 8.3.

for the RPC detectors. The MS hits are not binned by hit energy deposit. MS calibration was also done based on a muon sample, however much looser selection cuts gave a considerably larger set of tracks that allowed for the higher calibration granularity.

7.3.4 Motivation

The general idea with calibration is to eliminate as many of the biasing effects as possible by using real signals with known physical properties that can be used as a reference point. To calibrate the timing, one therefore needs particles with known arrival times. Fortunately, obtaining a sample of particles travelling at the speed of light is very simple. Since the LHC operates at such high energies, all observable SM particles above a very affordable impulse cut are travelling at a speed that is experimentally indistinguishable from the speed of light. Such particles will therefore always arrive at the same time for a given detector element in all events. This time, the arrival time of light, is used as the time origin for each individual detector element. The choice and selection of the calibration data set is discussed in detail in section 6.6.

The plan is to collect the measured arrival times of the calibration particles. These arrival times will consist of the true arrival time (t_0), a bias, and a random error.

$$t_{\text{measured}} = t_0 + t_{\text{bias}} + t_{\text{error}} \quad (7.4)$$

The error is assumed to be random and follow a zero centred gaussian distribution by the central limit theorem. The width of this distribution is assumed to have the same degree of variability as the bias. The bias will depend on many factors, but is in general assumed to be a slowly varying function of all influences so that two similar hits in the same cell will in general have the same bias.

By plotting a histogram of the arrival times of many similar particles, we obtain a distribution with a certain width, and a mean, generally different from zero. This mean, later called t_c , can be used as a correction on the measured times that contributed to the distribution, leading to a bias-free measurement of arrival times.

This first type of calibration is carried out on signal-candidate particles using reference particles, both from real data. What we unfortunately cannot correct for using data is the scaling of the time measurement. Since there are no SM particles with true late arrival time, the time scale cannot be calibrated using data². We therefore use Monte Carlo samples with simulated slow particles to investigate our ability to measure late arrival times correctly. As mentioned before, correctness of timing issues was not a top

²For an exception, see the pixel $\beta\gamma$ calibration in section 7.2.

priority in the design of the outer detectors, and this is why also in the simulation, there are some effects that were not correctly modelled, leading to differences in timing measurements between MC and real data. To improve the quality of our MC samples we carried out a second type of calibration on these on top of the bias calibration that we also apply on data.

The distributions of the measured times were plotted in MC and were found to be narrower than their data counterparts in all cases. This means that the measurement error was underestimated in MC, leading to too precise time measurements. To correct for this, a smearing was carried a smearing was added to each MC measurement as described in point 2 on page 101.

In addition to making the MC widths match data, the widths are also used as an estimator of the accuracy when adding various measurements. This is described in section 8.3.

In the following sections I will discuss a range of issues that were found to be relevant in connection with this calibration.

Calibration granularity

When carrying out the calibrations described in this chapter, decisions needed to be made about how fine to split up the data sample. Ideally only hits that have identical t_{bias} and intrinsic spread t_{error} would be grouped together. This way all offsets could be eliminated and all errors would be perfectly known leading to optimal measurements. The factors that we used to group the hits for calibration were:

- the energy deposited in the hit
- the detector layer
- the detector element (MS only)
- the detector technology
- η of the track (for the calorimeter only barrel vs. end-cap)
- the run-period

Other factors that might have been worth investigating further were:

- the detector element for the calorimeters
- η of the track (finer binning)
- ϕ of the track
- the time of the hit:
 - location within the run

– which bunch of the beam

We found no influence of the particle species (muons versus jets) or the particle momentum on the timing (see section 6.6 and figure 6.4).

Some of these influences are strongly correlated with each other, for example, the position of the hit and the detector type, layer, etc. so not every one of these influences should become an independent splitting dimension. When choosing which characteristics to split by, it is important that the obtained values of t_{offset} and t_{error} should be at least as well defined as the expected overall timing accuracy. For this the number of entries in the distribution of measured times in each category should be large enough. In our analysis we chose to set the limit of 50 entries in a category. All hits in categories with fewer entries were simply discarded. This meant a loss of $< 0.1\%$ of hits.

The choice of how to bin the calibration track is thus a trade-off between only grouping tracks that are as similar as possible and getting enough statistics in the rarer bins.

There is one more way of grouping the calibration tracks that avoids the problems of low statistics. The influence of the time of the hits, i.e. which run, how late in the run etc., is believed to be caused by shifts in the overall detector synchronisation and should affect all detector elements equally. Timing effects can therefore be factored out. In practice this means that time dependencies should be apparent as, for example, run-by-run changes that affect the entire detector, even when the individual parts of the detector are still uncalibrated. In this way it is possible to first calibrate the run-wise variation using the whole detector as one, and then recombine the run-wise calibrated tracks from different runs for a calibration by detector element, momentum etc. as described above.

7.4 Results

The results of the calibration procedure are presented in figures 7.10, 7.11 and 7.12. It can be seen that the MC distributions have become much more similar to data than before calibration. The data distributions are now unbiased but have not become noticeably narrower than before for calorimeter and MDT measurements. For RPC measurements the data distribution has improved considerably.

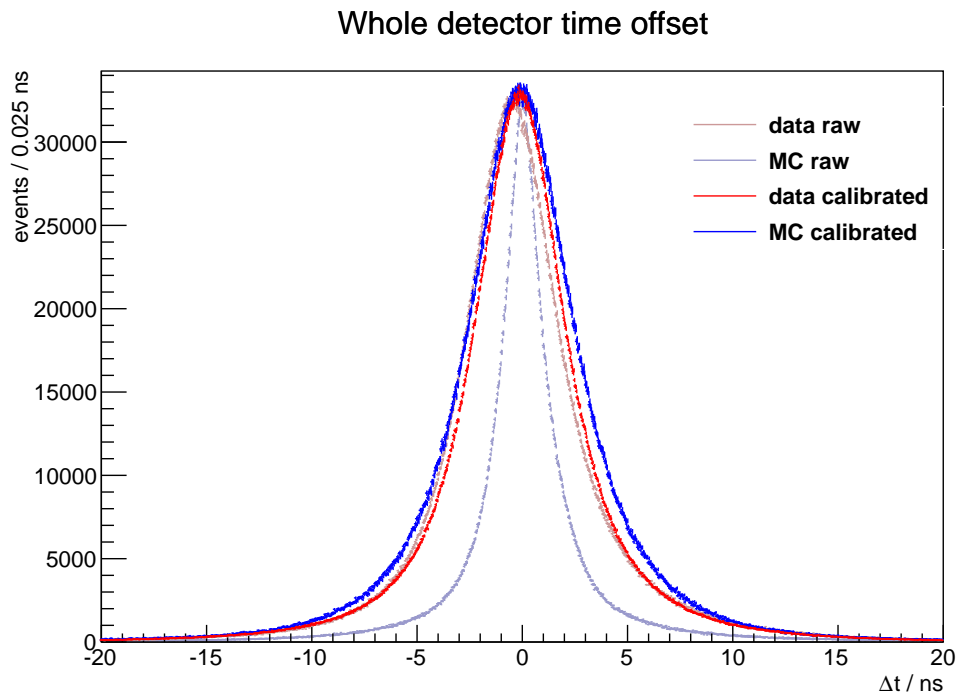


Figure 7.10: *The distribution of deviations from the expected hit time for all calorimeter cells for the calibration sample before and after the calibration procedure. The MC distributions have been scaled to have the same maximum as the corresponding data distribution. Error-bars are included.*

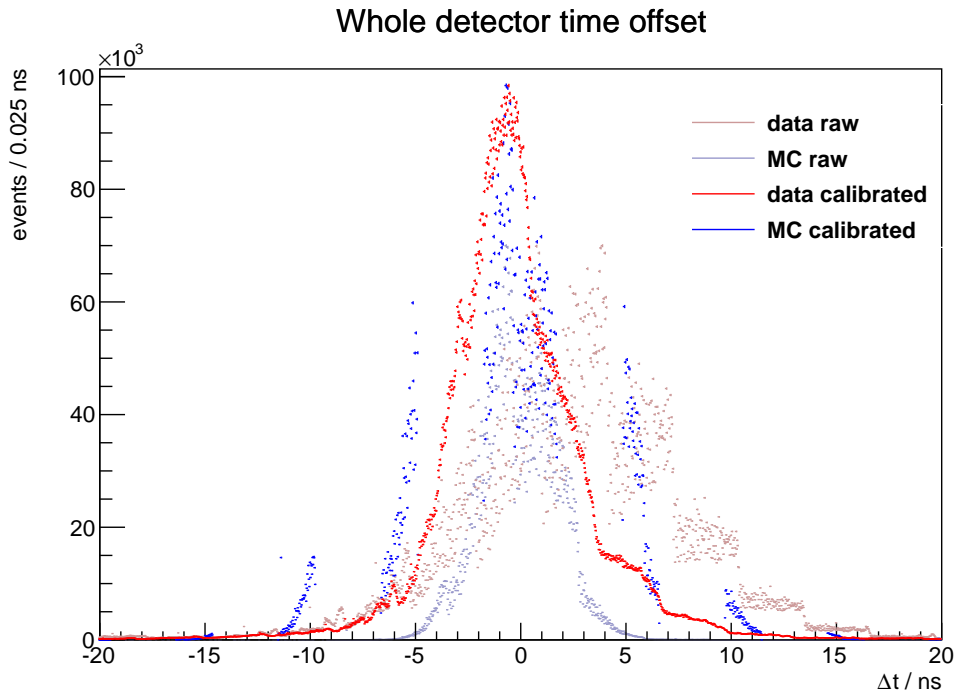


Figure 7.11: The distribution of deviations from the expected hit time for all RPC chambers for the calibration sample. Otherwise as in figure 7.10.

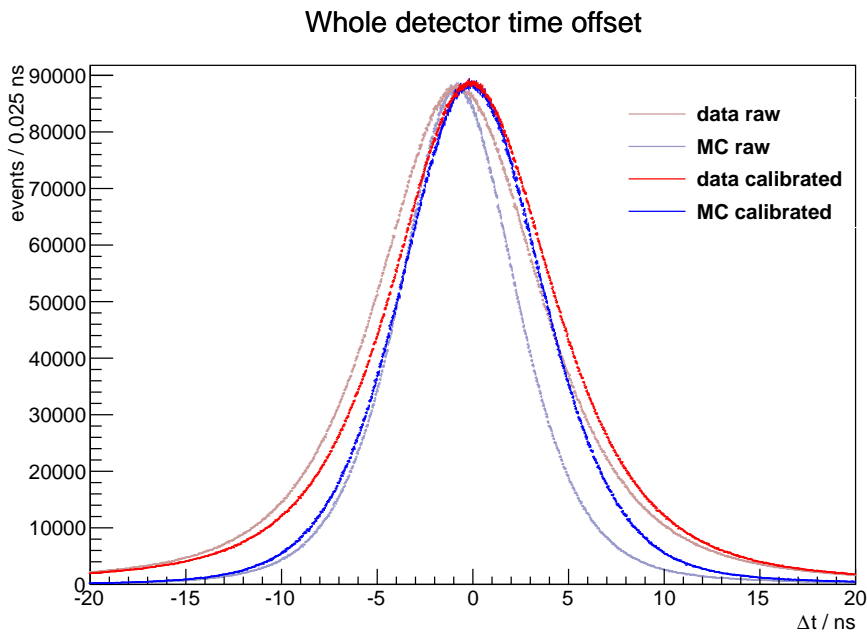


Figure 7.12: The distribution of deviations from the expected hit time for all MDT chambers for the calibration sample. Otherwise as in figure 7.10.

Chapter 8

Analysis Strategy

8.1 Goals

Our goal in this work was to search for stable massive coloured particles at the ATLAS detector by direct observation of a slow track. Alternative search strategies have also been considered and are the subject of different ATLAS publications:

- Kinked and disappearing tracks could be the result of stable new particles that decay into visible or invisible secondary particles mid-ways through the detector [64].
- Meta-stable new particles that are stopped in the calorimeter could lead to unexpected energy deposits when they decay at a later time [65].

These strategies are generally focussed on shorter and longer lifetimes respectively, than the particles that our search is sensitive to. Thus they are complimentary approaches.

In our search we were aiming for maximum sensitivity in order to be able to discover such particles, should they exist, or to set a new best limit on the production cross section if we do not find a signal. Earlier publications from the ATLAS collaboration had used only the inner detectors and calorimeters [7], only the pixel detector [4], or only the muon spectrometer [5]. Our goal was to now combine the entire detector into a single, more powerful analysis and use improved calibration techniques to further enhance our sensitivity. On top of this we used a larger dataset and therefore expected a greater discovery potential.

An analysis of this kind is quite atypical as compared to other ATLAS analyses. Nearly all analyses of LHC data are concerned with finding features in distributions of invariant masses, angular distributions or other quantities whose value is essentially fixed in the immediate vicinity of the hard collision. The propagation of particles to the outer layers of the detector and their various interactions with the detector material are interesting only

in so far as these particles communicate the information about the hard process from the interaction region out to a place where this information can be measured. It is the job of the detector to make as accurate as possible statements about the original 4-vectors and species of the particles emerging from the interaction point.

In this analysis however, the particles of interest actually leave the interaction region. The interesting physics is therefore also happening out in the detector, in the trackers, calorimeters and muon spectrometers. This really sets our analysis apart from the bulk of ATLAS analyses. It is because of this non-standard nature of our analysis that we had to develop our own calibration, and got little support from most of the ATLAS collaboration, something that made our job considerably harder.

The basic strategy to find SMPs was based on the high mass of these particles. The high mass m leads to a lower velocity for a given momentum p since

$$p = m\beta\gamma \quad (8.1)$$

where β is the velocity in units of the speed of light and the Lorentz gamma factor $\gamma = 1/\sqrt{1 - \beta^2}$. This reduced speed is a completely unique feature that no SM particle is able to reproduce in the absence of mismeasurement. This automatically sets the stage for our measurement, since a search for low velocity particles is a battle against measurement errors of all kinds through which SM particles can falsely appear to have a lower velocity, and therefore appear to be very massive. Errors in the momentum measurement do occur, but are of a much lower magnitude, making speed measurements by far our primary source of error.

We employed two distinct ways of measuring the particle speed. The first was a measurement of the time of flight (ToF) between the point of creation and the point of detection of a particle. The other was an indirect measurement where we measured the energy loss in the detector material. As mentioned in section 5.3.1 the energy loss through ionisation of a point charge moving through a material depends only on the speed of the charge. Thus, using a calibrated relationship between speed and specific ionisation we were able to convert this measurement back into a value of $\beta\gamma$.

8.2 Choice of Sub-detector

In principle both types of measurement can be carried out by all types of detectors, In practice however, there are a range of limitations that make some measurements inaccurate or impossible.

The pixel detector does a full analog-to-digital (A2D) conversion for every pixel. This makes it quite well suited for measuring ionisation. Just like the rest of the inner detector, it has a much too short arm length however to make ToF measurements feasible. Figure 5.6 shows the measured

value of dE/dx for low momentum reconstructed tracks. Different particle species can be seen as different bands since the different masses determine the relationship between $\beta\gamma$ and p .

Even though the SCT has a very similar mode of operation of the Pixel. Its channels are only read out as binary hit/no hit information. This makes ionisation measurements impossible. The SCT was not used in our analysis.

The time resolution of the TRT was low for a ToF measurement at the given arm-length. As described in section 5.6.7, the TRT is capable of specific ionisation measurements. There were however unresolved problems with this measurement that meant that the TRT dE/dx could not be included in our analysis.

The calorimeters use two different detector technologies, liquid argon (LAr) and scintillator tile (Tile). The tile calorimeter has considerably better time precision than the LAr. Both can be used to measure the ToF of particles, and because the calorimeters are sufficiently far from the interaction point, the particle speed can be reconstructed quite well. Since the calorimeters are built to measure energies, they can also be used to measure the energy loss of traversing particles in a dE/dx type measurement. Previous work that had been carried out in this direction [66] had not been sufficiently verified at the time of our analysis which is why the calorimeter dE/dx measurement was not included in our analysis.

The muon spectrometer (MS) is made up of four different technologies. There are thin-gap chambers (TGC), resistive-plate chambers (RPC), monitored drift tubes (MDT) and cathode strip chambers (CSC). They differ in spacial resolution and timing precision. The TGC and RPC are fast, low resolution detectors that allow triggering while the MDT and CSC are precision detectors. The muon spectrometer provided a good measurement of the ToF for particles that could be detected there. We did not use the muon spectrometer to measure ionisation loss although work in this direction is ongoing. Only the MDT and RPC chambers are useful for our analysis because of the limited coverage of the other technologies. The MDT and RPC systems are capable of quite independent measurements of particle arrival times. They are independent of each other and of the calorimeters as shown in figure 8.1.

8.3 Combination Strategy

The overall strategy is to measure the particle speed in as many ways as possible. Then we will use the correlations between measurements for signal and the lack of correlations in background candidates to select the signal.

After the choice of sub-detector had been made we were left with one dE/dx measurement from the pixel detector, and several time measurements, one from each hit in the calorimeters, and one from each muon

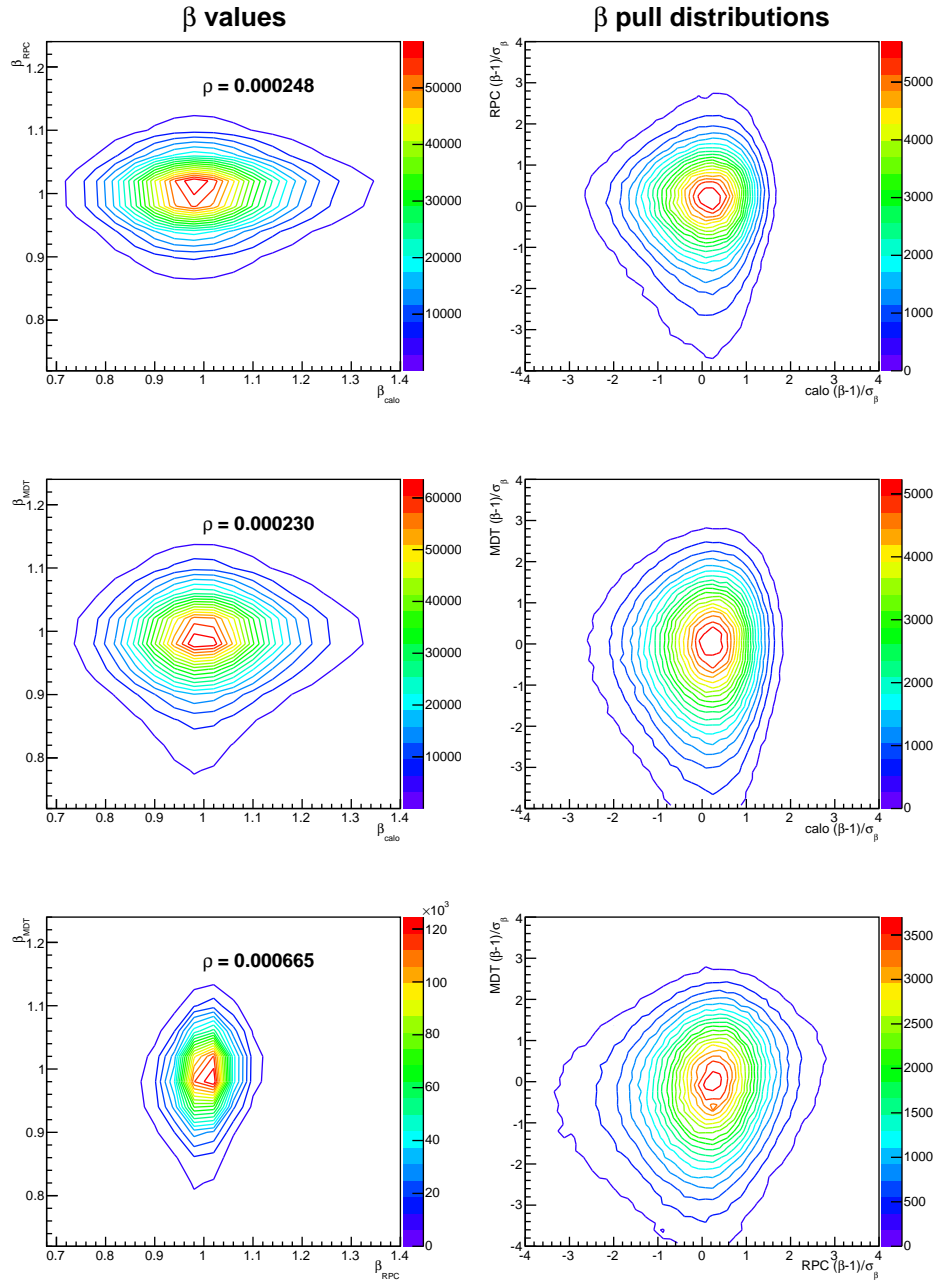


Figure 8.1: The correlation plots for β values from different sub-detectors for the calibration sample. All calibration muons have $\beta_{\text{true}} = 1$. Deviations from this are scaled with the estimated error giving the pull distributions. The low correlation coefficients confirm the assumption of independent estimators.

chamber hit. The task was thus to combine these measurements into a good discriminator of signal vs. background.

Three strategies have been discussed to achieve this, of which only one was chosen for the final publication. The three strategies are

- a single mass estimate from a global track fit,
- a likelihood based signal estimator,
- a weighted average of all speed measurements followed by a signal cut.

Each of these approaches has advantages and disadvantages as discussed in the following.

8.3.1 Global Track Fit

For this method all hits from both muon chambers, calorimeters and inner detector are combined and a single track is fitted to them. The track speed β is left open as a fit parameter and can therefore be obtained from the fit. An uncertainty on the returned value of β is also available. The fitting algorithm works by trying to find the track parameters (η , ϕ , p_T & β) that minimise the difference between observed and predicted location and arrival time at all hits.

Once this overall optimal estimate of β has been obtained, it can be combined with the particle momentum, also obtained from the fit, to give the particle mass. In a one-dimensional histogram of all track masses, all SM particle tracks will have low masses, whereas a peak around any higher mass would be an indication of a signal.

Advantages of this method are:

- Track fitting algorithms are a standard tool in ATLAS which have proven themselves reliable in momentum reconstruction and track finding.
- A varying number of hits can easily be accommodated.
- non-gaussian errors can be taken into account.

The method also has a number of drawbacks:

- Ionisation measurements can not easily be included in the fit. They need to be added to the analysis as a separate signal discriminator.
- Track fitting algorithms are computationally complex. The standard implementations in ATLAS were only accessible to us as part of the full reconstruction software package ATHENA. If we wanted to use them together with our custom calibration we would have had to

- implement all our calibration inside the ATHENA framework,
 - run the re-fitting algorithms on all ATLAS data at a large computational cost, particularly when several reruns are necessary in the course of analysis development.
- The optimal speed estimator is not necessarily also the best signal discriminator. Additional signal selection cuts need to be introduced based on the consistency between the time measurements of various sub-detectors. This is needed to reject cases where a large mismeasurement in a single sub-detector pulls the average speed measurement down. (This also leads to the problem of how to define the β estimate from one sub-detector vs. another if the estimates only come from a global track fit.)

8.3.2 Likelihood Method

This method is based on a fundamentally different philosophy from the above. Instead of trying to estimate the mass of all particles as precisely as possible in order to then identify high mass particles, this method mainly attempts to discriminate between particles that show high-mass like behaviour and those that do not.

The method is based on the principle of likelihood. It works by constructing the combined probability of a set of discriminators under the assumption that they are drawn from a background distribution. This is achieved by building a reference model of how each measurement should be distributed in the absence of signal by using the calibration sample. Afterwards each discriminator (timing or dE/dx) is compared to its cumulative reference distribution in order to assign a so called r -value for that estimator. The r -value has a range of $[0,1]$ and gives the relative height of the cumulative distribution at the given value. For values that are randomly drawn from the reference distribution the r -values will be uniformly distributed on $[0,1]$. The combined likelihood is then taken to be the product of the r -values from each estimator. In practice the logarithm of the r -values will be used which can be added instead of multiplied.

Drawing combinations of independent estimator values, and plotting the combined likelihood value, a cut value of the likelihood can be found that would pass a well known amount of background. A value of 0.1 background events could be selected, for example.

The estimator values of a signal track will generally originate from a different distribution than the reference. The direction of integration for the r -values can be chosen such that signal will generally have higher values than the reference. Hence, counting the number of tracks with a combined likelihood higher than the signal cut, chosen above, a signal can be identified as an excess above the expected background.

Advantages of this likelihood method are:

- All estimators can be combined including timings, dE/dx and momentum estimates.
- A signal region can be defined without reference to a particular simulated signal sample giving model independence. The signal region simply states how atypical a track is.
- Non-gaussian tails are trivially accounted for.

Problems of the method are:

- It is difficult to combine tracks with different numbers of hits since the sum of $\log(r)$ will have a different number of terms and therefore requires a different signal cut.
- Reference distributions with very high statistics are needed because it is the tails of the distributions where the largest discrimination power is gained.
- Signal contamination in the reference distributions can degrade the performance of the discriminator. This makes the selection of the reference sample more important than it was for the purpose of timing calibration.
- The method is a ‘black box’. This means that once estimators are converted to likelihoods, no further physical insight can be applied to them. This can make it difficult to identify errors in the implementation and the method itself, or spurious signals that originate from unforeseen detector effects.

A method to resolve the dependence on the number of available estimators was suggested by the present author as follows:

The product of n independent uniformly distributed random variables is itself a random variable U distributed as

$$P(u) = f_n(u) = \frac{(-1)^{n-1}}{(n-1)!} (\ln u)^{n-1} \quad (8.2)$$

where P is the probability density [67]. A new uniformly distributed random variable X can be found by numerically inverting the corresponding cumulative distribution function $F_n(u)$:

$$X = F_n^{-1}(U) \quad (8.3)$$

In the case of the above likelihood method this could be used to obtain a single discriminator X . The advantage of X would be that it is uniformly distributed for any number of contributing estimators n (dE/dx , timing etc.) and a single signal cut could be defined on it.

A clear disadvantage would be that it further confounds the problem of dealing with derived ‘black box’ discriminators.

8.3.3 Average + 2D Cut Method

At a meeting with our collaborators in Israel the above two methods were rejected in favour of the following.

This method consists of reducing all the estimators to two distinct measurements of the particle's mass. One based on timing (later m_β) and one based on specific ionisation ($m_{\beta\gamma}$). Each mass is arrived at by combining the best speed estimate with the measured momentum from curvature in the relationship

$$p = m\beta\gamma. \quad (8.4)$$

The $\beta\gamma$ estimate already relied on a single measurement only, coming from the pixel detector. Hence only the individual timings had to be combined to give a single best speed estimate. This was done as a weighted average of the individual measurements. This averaging was done using the inverse of the speed measurements in order to preserve the gaussianity of the timing errors.

To combine the speed measurements we used the method of weighted averages. If a number of measurements x_i of the same quantity exist and each has a different expected uncertainty σ_i , they can be combined to the overall best estimate \hat{x} as

$$\hat{x} = \frac{\sum \frac{x_i}{\sigma_i^2}}{\sum \frac{1}{\sigma_i^2}} \quad (8.5)$$

where the sums run over i . The uncertainty on the estimate is

$$\sigma_{\hat{x}} = \left(\sum \frac{1}{\sigma_i^2} \right)^{-1}. \quad (8.6)$$

In our case the individual timings t_i were actually measurements of the particle velocity β when combined with the cell's distance from the interaction point d_i where

$$\beta_i = \frac{d_i}{t_i}. \quad (8.7)$$

Since we decided to neglect uncertainties on the distance, the overall uncertainty on β_i could be calculated from the timing width $\sigma_{t,i}$ as

$$\sigma_{\beta,i} = \frac{\sigma_{t,i}}{t_i} \beta_i \quad (8.8)$$

For a correct weighted average, the individual errors need to be gaussian. Timing errors are generally gaussian as they are the result of many sources of error, and are thus following the central limit theorem. This was seen in figure 7.1. Converting them to estimates for β does not generally preserve this property though. This is why we chose to combine estimates

of β^{-1} as they preserve the gaussianity of the errors. Hence we converted the individual time measurements to β^{-1} measurements as

$$\beta_i^{-1} = \frac{t_i}{d_i} \quad (8.9)$$

$$\sigma_{\beta^{-1},i} = \frac{\sigma_{t,i}}{d_i} \quad (8.10)$$

and finally we combined the resulting values as

$$\widehat{\beta^{-1}} = \frac{\sum \frac{\beta_i^{-1}}{\sigma_{\beta^{-1},i}^2}}{\sum \frac{1}{\sigma_{\beta^{-1},i}^2}}. \quad (8.11)$$

Besides finding the calibrated time measurements, we therefore also needed to find the expected error of each measurement. These two parts were closely related. As described in detail in section 7.3, we had already grouped the various time measurements by a range of criteria related to the expected biases and errors for the purpose of calibration. The resulting distributions provided the widths that were assigned as errors to the time measurements.

8.4 *R*-hadron versus Slepton Search

Until this point the searches for *R*-hadron and slepton SMPs have required the same tools and prerequisites. There are however differences between these two types of particles justifying different approaches.

- *R*-hadrons have already been excluded to higher masses than sleptons. We therefore focus on higher mass regions when hunting for *R*-hadrons. Particles of these masses will have lower β , reaching the limits of what can be reconstructed with the MS spectrometer. Sleptons, with a lower mass window, will have higher β , making dE/dx discriminators less powerful.
- *R*-hadrons have a high chance to be neutral. Seeing both *R*-hadrons in an event is so rare that it is not worth considering. Hence we only consider the most energetic candidate in every event. Sleptons are always charged, and if the event is triggered, looking for both candidates is a good signal discriminator leading to a different set of cuts.

The quality cuts described in the following chapter apply equally to the slepton and *R*-hadron searches. The combination strategy is also used for both. The way that a signal is defined however differs between the two.

I, the present author, was exclusively focussed on the *R*-hadron search. Slepton search criteria will only be mentioned for completeness.

Chapter 9

Quality Selection

Event selection is the process of selecting events from the input data in order to improve the further analysis. The selection can be divided into two major parts. In the first part, called quality checking, we removed events and candidates where we had reason to suspect bad or noisy measurements. The primary discriminators were not looked at at this stage. The second part, called final selection (or just selection), was where the mass measurements were used to separate signal-like events from background-like events in order to be able to make statements about the signal strength. This second part will be covered in the next chapter.

In quality checking the focus is on obtaining events and candidates that are well measured, i.e. events where known sources of uncertainty and errors are avoided as far as possible. The event and candidate characteristics used for this are not the primary discriminators, like the impulse, or the measurements of β , but auxiliary variables that are correlated with the accuracy of those discriminators, like candidate isolation and the number of tracker hits. In reality, there will be some correlation between the signal purity and some of these cuts, which is why their effect was studied on the MC signal samples and the calibration sample to make sure that signal was not unnecessarily discarded.

Quality checks were applied to all samples used in our analysis, including the samples that were only used for timing calibration and on all MC samples. The cuts were checked to make sure that true muons coming from $Z \rightarrow \mu\mu$ would be accepted since they share many of the properties that we expect from R -hadrons.

In the final selection, after all detector calibrations were applied, we used the discriminators used to divide the sample into signal and background. This was done by combining the measured impulse once with the combined best estimate for the particle velocity β , and once with the estimate of $\beta\gamma$ obtained from the specific ionisation in the pixel detector. The resulting two mass measurements were each cut on for the final signal selection. This

method was first introduced in section 8.3.3 and will be further discussed in section 10.2.

9.1 Quality Check

Quality checking can be split up into two stages, event based checks and candidate based checks. The event quality checks consist of

1. data preparation (Stream overlap removal),
2. detector conditions checks (good-runs list),
3. trigger checks,
4. a basic tracking quality check.

Stream overlap removal and detector conditions checks are explained in the following sections. The choice of trigger has been explained in section 6.4.

Point 4 refers to the single physics cut that was imposed at the event level. This cut was that an event had to have at least one reconstructed collision vertex that had at least three tracks associated to it. There were a low number of events where this was not the case. It was deemed that such events likely either contained no interesting physics or had generally bad tracking. The events were therefore discarded. This cut was partially kept in the analysis for consistency with the work from [7].

After good events have been selected these events are searched for good quality candidates. This candidate based selection is described in section 9.2.

9.1.1 Stream Overlap Removal

Data streams were introduced in section 5.9.3. For our analysis we used the Muon and JetTauEtmiss streams. We would have liked to analyse also the debug stream. The unusual event topologies of interest to us might perhaps have caused reconstruction issues of the type that cause events to be pushed to this stream. Unfortunately, this stream was not available to us at the time and pursuing this data was not prioritised. The number of events in this stream is so low that it was decided not to pursue this route further.

Since some events can appear in multiple streams it is important to remove the overlap so that each event is counted once and only once in the analysis. A bug in this overlap removal caused quite an excess in the high mass region of our signal region until the bug was discovered. This is because events with very high p_T particles are more likely to trigger multiple triggers, and such events also feature prominently in our signal region since p_T is the major signal estimator.

9.1.2 Detector Conditions

A machine as complex as the ATLAS detector has many points of failure. Therefore the conditions of all parts of the detector are constantly monitored. Monitoring is carried out on many levels starting with hardware sensors checking that the electronics and mechanical parts are behaving as expected, but the final check is to see that known physics processes are correctly measured in the data.

These data quality checks are concluded at regular meetings of specialised data quality experts and data quality flags (good or bad) are assigned for each sub-detector system independently on time units down to luminosity blocks. These flags are stored in a central database.

Analyses that are only interested, say, in calibrating the calorimeters can then extract a list of runs and luminosity-blocks that are flagged as good for those sub-detectors only. For our analysis it was necessary that all parts of the detector should behave correctly and we therefore chose a very restrictive good-runs list. In order to be consistent with previous work, we chose to use the good-runs list that was also used for publications in Standard Model physics by the Standard Model working group within our collaboration.

9.2 Candidate Selection

After the events had been selected as good, they were searched for any suitable candidates. As mentioned in section 3.2.2 we carried out two different searches, one *muon agnostic* and one *full detector* search. The muon agnostic approach was to ignore all muon spectrometer information including trigger and identify candidates based solely on information coming from the ID and calorimeters. For the full detector approach all information was used. The muon agnostic approach is mostly motivated by the possibility of R -hadron charge-flips mentioned in section 3.4.2. A muon agnostic search using inner detector and calorimeter information only (MS agnostic) could thus be more independent of any assumptions on the interaction model.

The candidate quality selection cuts were designed to reject candidates where the estimators could be expected to be noisy. For the full detector search, different selection criteria were used based on whether a MS extension of the track had been found. If none was found, the candidate could still enter the analysis and timing information was taken from the calorimeters only. Candidates with a MS extension are called combined (CB) candidates, without a MS extension they are called inner detector (ID) candidates.

The cuts that were used to select suitable candidates for further analysis are shown in tables 9.1 and 9.2 for full detector and muon agnostic searches respectively.

The jet ΔR cut can be justified by the plots shown in figure 9.1 where

	$\tilde{g}_m=600$ GeV	$\tilde{g}_m=900$ GeV	$\tilde{g}_m=1200$ GeV	data
generated	100.0	100.0	100.0	-
triggered	27.1	21.3	16.0	100.0
CB candidate	17.0	11.9	8.3	29.5
$N_{\text{tracks}}^{\text{vertex}} > 3$	17.0	11.9	8.3	29.5
$N_{\text{SCT}}^{\text{hits}} + N_{\text{SCT}}^{\text{deadsensors}} > 5$	16.9	11.9	8.2	29.4
$z_0 < 10$ mm	16.9	11.8	8.2	29.3
$d_0 < 2$ mm	16.9	11.8	8.2	29.2
$N_{\text{PIX}}^{\text{shared hits}} = 0$	16.9	11.8	8.2	29.0
$p_T > 10$ GeV	16.9	11.8	8.2	28.9
$20 \text{ GeV} < p < 3.5\text{TeV}$	16.8	11.7	8.1	27.9
$\Delta R_{\text{track}, p_T > 10 \text{ GeV}} > 0.25$	16.7	11.6	8.1	15.4
$\Delta R_{\text{jet}, p_T > 40 \text{ GeV}} > 0.3$	16.6	11.5	8.0	14.6
$N_{\text{PIX}}^{\text{good dE/dx hits}} > 1$	15.7	10.9	7.5	14.0
$0 \text{ MeVg}^{-1}\text{cm}^2 < \text{dE/dx}_{\text{PIX}} < 20 \text{ MeVg}^{-1}\text{cm}^2$	15.7	10.9	7.5	14.0
$0 < \beta\gamma_{\text{PIX}} < 10$	15.4	10.8	7.5	8.9
$ \eta < 2.0$	14.3	10.1	7.2	8.4
associated (slow) muon track	14.3	10.1	7.2	8.4
cosmic-veto	13.8	9.7	6.9	8.3
$0 < \beta_{\text{CALO}} < 2$ or $0 < \beta_{\text{MDTT}} < 2$ or $0 < \beta_{\text{RPC}} < 2$	13.4	9.3	6.6	8.1
consistent β measurement(s)	12.6	8.7	6.3	7.0
ID candidate	6.4	6.0	4.9	77.8
$N_{\text{tracks}}^{\text{vertex}} > 3$	6.4	6.0	4.9	77.8
$N_{\text{SCT}}^{\text{hits}} + N_{\text{SCT}}^{\text{deadsensors}} > 5$	6.4	5.9	4.9	77.5
$N_{\text{TRT}}^{\text{hits}} + N_{\text{TRT}}^{\text{deadstraws}} > 5$	5.8	5.2	4.3	76.4
$z_0 < 10$ mm	5.8	5.2	4.3	75.3
$d_0 < 2$ mm	5.8	5.2	4.3	75.2
$N_{\text{PIX}}^{\text{shared hits}} = 0$	5.8	5.2	4.2	75.2
$p_T > 10$ GeV	5.8	5.2	4.2	67.6
$20 \text{ GeV} < p < 3.5\text{TeV}$	5.8	5.2	4.2	64.0
$\Delta R_{\text{track}, p_T > 10 \text{ GeV}} > 0.25$	5.6	5.1	4.1	11.6
$\Delta R_{\text{jet}, p_T > 40 \text{ GeV}} > 0.3$	5.6	5.1	4.1	4.3
$N_{\text{PIX}}^{\text{good dE/dx hits}} > 1$	5.2	4.7	3.8	4.0
$0 \text{ MeVg}^{-1}\text{cm}^2 < \text{dE/dx}_{\text{PIX}} < 20 \text{ MeVg}^{-1}\text{cm}^2$	5.2	4.7	3.8	4.0
$0 < \beta\gamma_{\text{PIX}} < 10$	5.1	4.6	3.5	2.7
$ \eta < 2.0$	4.4	4.2	3.2	2.0
consistent β measurement(s)	3.6	3.4	2.7	1.3
sensible β measurement	3.4	3.3	2.6	1.2
CB and ID+Calo	15.0	11.0	8.1	8.1

Table 9.1: Quality selection cut-flow table from the full detector search for three example \tilde{g} masses hypotheses. Both ID and CB selection are shown. All numbers are percentages of the total generated number. The cutflow is per event in each category. Some events have both types of candidates, and hence the individual number do not add up to the total.

	$\tilde{g}_m=600$ GeV	$\tilde{g}_m=900$ GeV	$\tilde{g}_m=1200$ GeV	data
generated	100.0	100.0	100.0	-
triggered	18.7	16.3	13.6	100.0
ID candidate	18.7	16.3	13.6	78.7
$N_{\text{tracks}}^{\text{vertex}} > 3$	18.7	16.3	13.6	78.7
$N_{\text{SCT}}^{\text{hits}} + N_{\text{SCT}}^{\text{dead sensors}} > 5$	12.7	10.9	9.3	77.4
$N_{\text{TRT}}^{\text{hits}} + N_{\text{TRT}}^{\text{deadstraws}} > 5$	12.1	10.2	8.6	76.4
$z_0 < 10$ mm	12.1	10.2	8.6	75.7
$d_0 < 2$ mm	12.1	10.2	8.6	75.7
$N_{\text{PIX}}^{\text{shared hits}} = 0$	12.1	10.2	8.6	75.6
$p_T > 10$ GeV	12.1	10.2	8.6	72.5
$20 \text{ GeV} < p < 3.5 \text{ TeV}$	12.1	10.1	8.6	71.1
$\Delta R_{\text{track}, p_T > 10 \text{ GeV}} > 0.25$	11.9	10.0	8.5	14.5
$\Delta R_{\text{jet}, p_T > 40 \text{ GeV}} > 0.3$	11.9	10.0	8.4	6.5
$N_{\text{PIX}}^{\text{good dE/dx hits}} > 1$	11.2	9.4	7.9	6.1
$0 \text{ MeVg}^{-1} \text{cm}^2 < dE/dx_{\text{PIX}} < 20 \text{ MeVg}^{-1} \text{cm}^2$	11.2	9.4	7.9	6.1
$0 < \beta\gamma_{\text{PIX}} < 10$	11.0	9.2	7.7	4.0
$ \eta < 2.0$	10.4	8.8	7.4	3.2
consistent β measurement(s)	9.1	7.7	6.2	2.0
sensible β measurement	8.9	7.4	6.1	1.8
Final ID+Calo	8.9	7.4	6.1	1.8

Table 9.2: Quality selection cut-flow table from the MS agnostic search for three example \tilde{g} masses hypotheses. All numbers are percentages of the total generated number.

900 GeV R -hadrons are used as a representative example. It is desirable to remove track candidates that are parts of a jet because the large energy deposit and the chance of secondary muons makes this tracks unreliable. The calorimeter energy deposit of an R -hadron track can itself be identified as a jet. The calorimeter energy deposit from R -hadron tracks is shown in the bottom right part of figure 9.1 and can be seen to be well below 40 GeV. The jet finding algorithms can however associate surrounding energy deposits to create jets of higher energy than this. We therefore plotted the distribution of ΔR to the nearest jet for several cuts on the jet's transverse energy. These are shown in figure 9.1. The spike at low ΔR can be identified as the jet that is centred around the R -hadron's own energy deposit. At a jet cut of 40 GeV this spike has disappeared. This allows us to conclude that all jets above 40 GeV are independent of the R -hadron. If one assumes that the kind of jet that could fake and R -hadron is similar to the jets caused by R -hadrons then one can see from the first plot in the figure that $\Delta R = 0.3$ marks a point at which one is decidedly outside the jet. With this reasoning it was decided to use the jet cut shown in the tables:

$$\Delta R_{\text{jet}, p_T > 40 \text{ GeV}} > 0.3 \quad (9.1)$$

During our analysis it was realised that there existed in our data sample a handful of tracks with unphysical high transverse momenta of several TeV and with very bad track fit quality. At these momenta even an expected

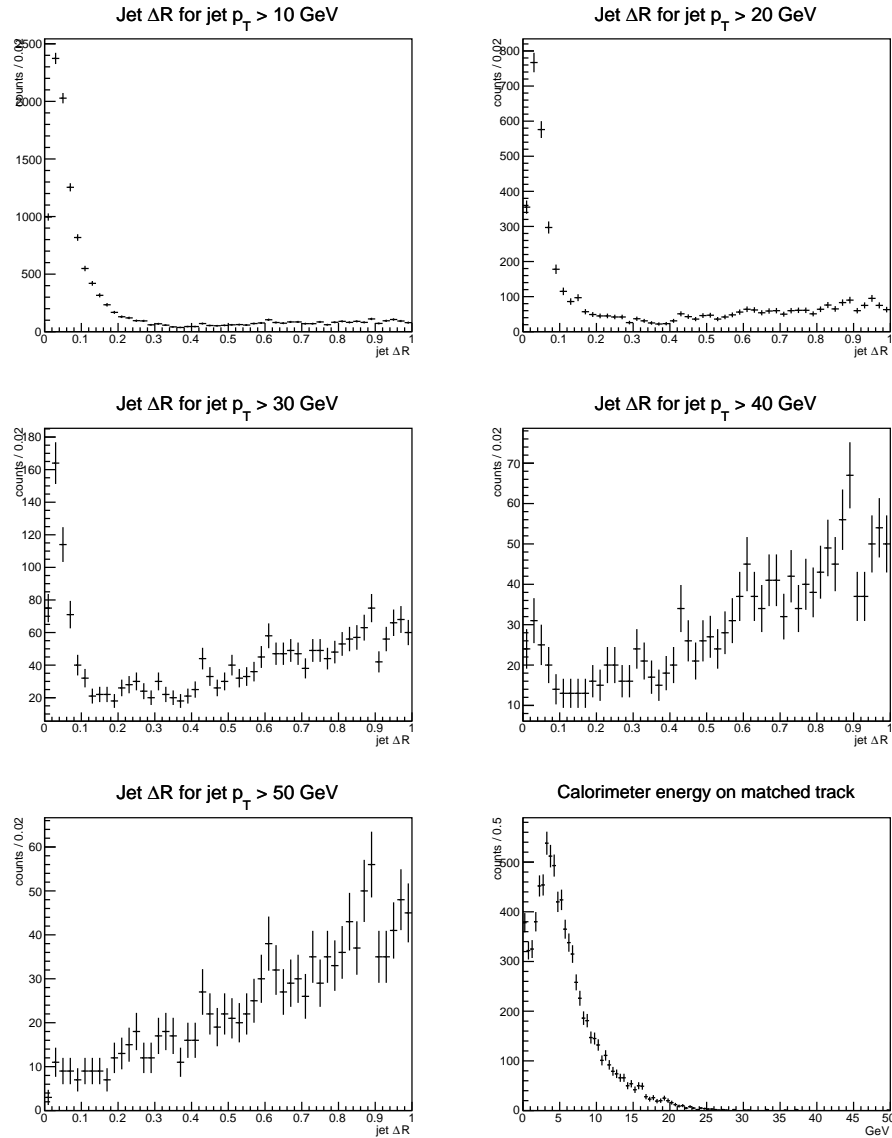


Figure 9.1: The ΔR separation of 900 GeV R-hadrons from the nearest jet. An R-hadron's calorimeter energy deposit can itself be identified as a jet. Hence the jet energy cut of 40 GeV is needed before the distance to the nearest real jet can be found.

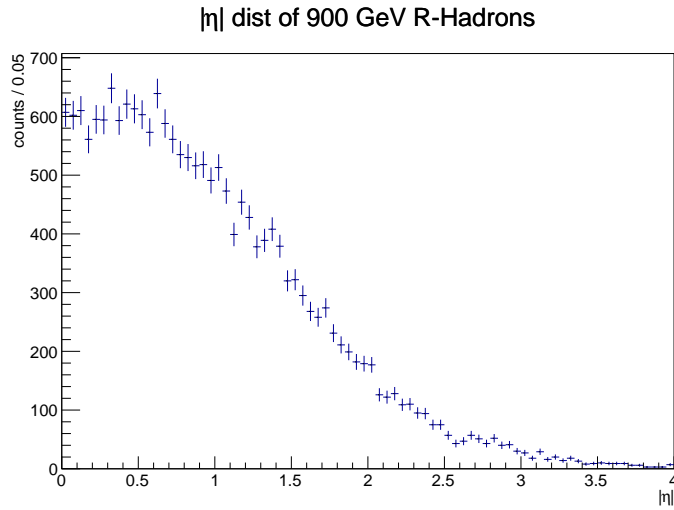


Figure 9.2: *The distribution of true absolute pseudorapidity for 900 GeV R-hadrons.*

variation in the speed measurement can lead to a very substantial reconstructed mass and lead to a fake signal. It was realised that these tracks only occurred at high pseudo-rapidities above $|\eta| = 2$. Figure 9.3 shows the relative momentum error as a function of the track $|\eta|$. Especially for high momentum particles the precision degrades considerable beyond $\eta = 2$. A reason for this is that tracks of this pseudorapidity do not traverse the whole bending plane before exiting the end of the ID tracking volume. This considerably reduces the lever arm for track momentum reconstruction and degrades performance. Figure 9.2 shows the η -distribution of generated R -hadrons. It can be seen that restricting the analysis to $|\eta| < 2$ does not significantly reduce the signal acceptance, while it does cut away all of the spurious tracks. Hence, this cut was used.

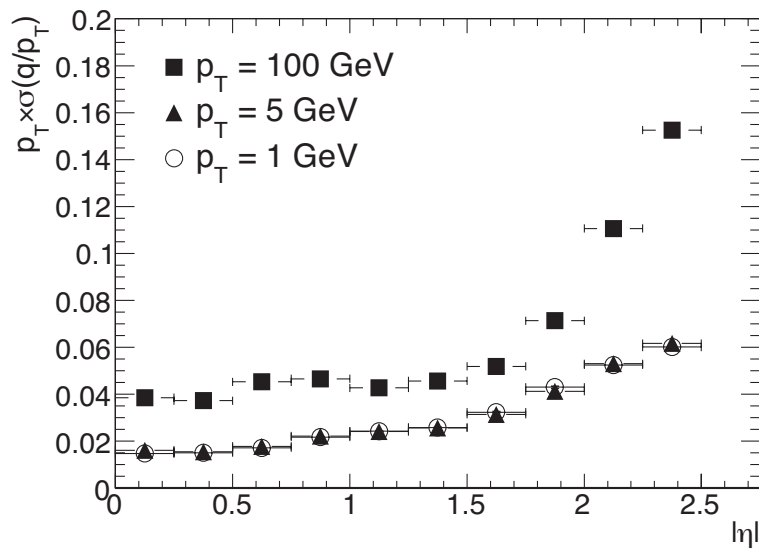


Figure 9.3: The relative tracking resolution versus η for muons of various momenta. Figure from [47].

Chapter 10

Final Selection & Background

10.1 Goals

The goal of the final selection is to define a signal region that optimises our ability to discriminate between signal and background. For this, we need to determine a set of cuts on the available estimators.

Our search was focussed not on one signal, but on many different mass hypotheses and SMP species. For each type of SMP, the signal strengths could be expected to be different, warranting different cuts. This is why those cut values that were optimised automatically, were found separately for each signal hypothesis.

10.1.1 Motivation for Data-Driven Background

After the analysis has been carried out, all events have been selected to either be part of the signal region or not. This number will contain some remnant of mismeasured SM particles that we have not been able to remove, but might also include a signal of true SMPs. In order to quantify our best estimate of the amount of true signal, we need a good estimate of the expected SM remnant, the so-called background.

There are several ways that such a background estimate can be obtained. The most direct way is to simulate a large number of SM events and count the number of those that fall into the signal region. This MC approach has a number of disadvantages:

- a heavy reliance on the correctness of all simulation steps
- a large computational cost

As we have emphasised several times in chapter 7 the speed measurements were not a priority in the design of ATLAS, hence the necessity for

custom calibration. This is also true for the design of all MC methods. Chapter 7 also highlighted numerous discrepancies between MC and data, particularly in the tails of distributions. The kind of measurement error that can lead to an SM particle being miscategorised into the signal region is precisely such a rare large error in the tails of the speed distributions where the agreement between MC and data is worst. This fact alone is enough to disqualify MC simulation as the sole estimate for background rates.

The second reason, large computational cost, is equally fatal for this approach. The number of background events in our signal regions are very low ($\mathcal{O}(1)$). The error of a statistical estimate goes as the square root of the number, hence

$$\text{relative error} = \frac{\sqrt{N}}{N}. \quad (10.1)$$

Thus to get, say, a 10% uncertainty on an expected background of 1 one would have to simulate 100 times the amount of available data.

Full MC event generation is computationally very expensive at about 30 min per event on a standard modern PC. Simulating the required number of events might be possible if all ATLAS computing resources were reserved for this analysis alone but is otherwise completely unfeasible.

Given these reasons, a data-driven background estimate had to be developed. In the remainder of this chapter I will describe the method that was used for our analysis.

10.2 Final Selection

After the end of the quality control checks there are only four variables per candidate that remain, these are

- the momentum, p
- the pseudorapidity, η
- the speed estimate from timing, β
- the speed estimate from ionisation, $\beta\gamma$.

The final selection is carried out in two different steps and is tightly coupled to the data driven background generation. The steps are

I cuts on the primary estimators p , β , $\beta\gamma$

II cuts on the derived estimators m_β , $m_{\beta\gamma}$.

10.2.1 Primary Estimator Cuts

The cut on momentum was chosen at a fixed value of 140 GeV. This value was found suitable as it allows good statistics for both the sideband method and background generation, both described below. The cuts on β and $\beta\gamma$ were selected based on a significance optimisation.

From an overview of all available signal hypotheses we knew that no signal should be present in any tracks with a momentum under 140 GeV. We selected all such candidates in data in the so-called sideband sample. We then plotted the 2D distribution of β vs. $\beta\gamma$ once for the entire sideband sample and once for the signal sample under study. Comparing these two distributions we were able to find the optimal combined cut on β and $\beta\gamma$ that optimised the signal significance.

The significance expression that was optimised was

$$\text{Sig} = \sqrt{2 \left((s + b) \log \left(1 + \frac{s}{b} \right) - s \right)} \quad (10.2)$$

where s and b are the total number of events that fall below a given set of cuts on β and $\beta\gamma$ for signal and background respectively [68]. They are thus both functions of those cuts. The optimal cut was found by looping over all bins in the above distributions and calculating the significance for each. The set of cuts that gave the highest significance could then be selected.

The set of cuts that was thus found defines the first part of the signal cuts. These are applied as

- $\beta\gamma < \text{Cut}_{\beta\gamma}$,
- $\beta < \text{Cut}_{\beta}$,
- $140 \text{ GeV} < p < 3.5 \text{ TeV}$.

These cuts together make up the cut set **I**. These cuts are mutually exclusive to the selection cuts for the sideband method.

10.2.2 Derived Estimator Cuts

If at this point an event contains more than one candidate, a random candidate is chosen and the rest are discarded. Since this is very rare for R -hadron signal samples and never occurs in data, which candidate is chosen does not affect the limit setting at all. We had to choose a candidate since the final result was intended to be a cross section on the number of events, not the number of candidates. The random selection was chosen because all non-random selections would introduce a bias to the sample.

At this point the primary estimators are combined into the derived estimators. Besides carrying individual information, the estimators β , $\beta\gamma$ &

p also carry information between each other since each set of β & p and $\beta\gamma$ & p is also an estimate of the mass through

$$m = \frac{p}{\beta\gamma} \quad (10.3)$$

where γ can be calculated as $1/\sqrt{1-\beta^2}$ for the β estimator.

After the mass estimates are thus formed from the primary estimators, the signal region had to be defined for them. This meant finding a suitable set of cuts. In order to retain most of the signal for maximal sensitivity, the following method was used separately for both m_β and $m_{\beta\gamma}$:

- using the signal sample, the distribution of the estimator was plotted
- this distribution was fitted with a gaussian covering the entire range from 100 to 3000 GeV.
- from this fit we obtained the mean μ and width σ of the reconstructed mass spread
- the cut was defined at $\mu - 1.28\sigma$.

The single-sided cut that is defined in this way makes sure that 95% of the mass distribution is passed by the cut. Examples of the distributions of m_β and $m_{\beta\gamma}$ that are generated this way are shown in figures 10.2 and 10.3 respectively. The final signal region is then defined as in figure 10.1.

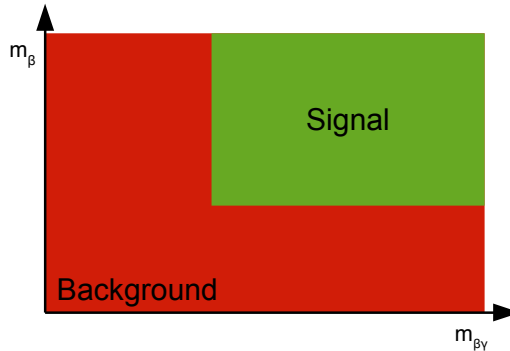


Figure 10.1: An illustration of how the signal region will be defined in the m_β vs $m_{\beta\gamma}$ plot.

10.3 Background Generation

The background was generated by sampling the distributions of β , $\beta\gamma$ and p . Random combinations of these values will not show the same correlations as the signal since they are not correlated via a true mass.

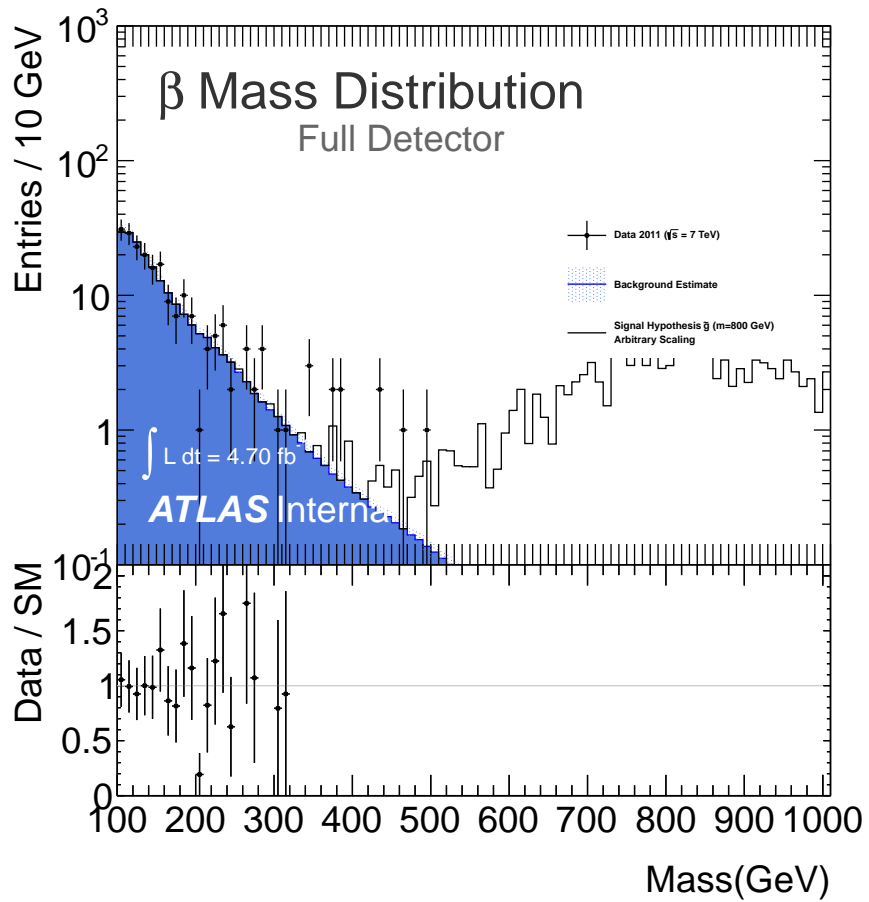


Figure 10.2: Data versus estimated background for the β -mass distributions of 800 GeV gluino R-hadrons.

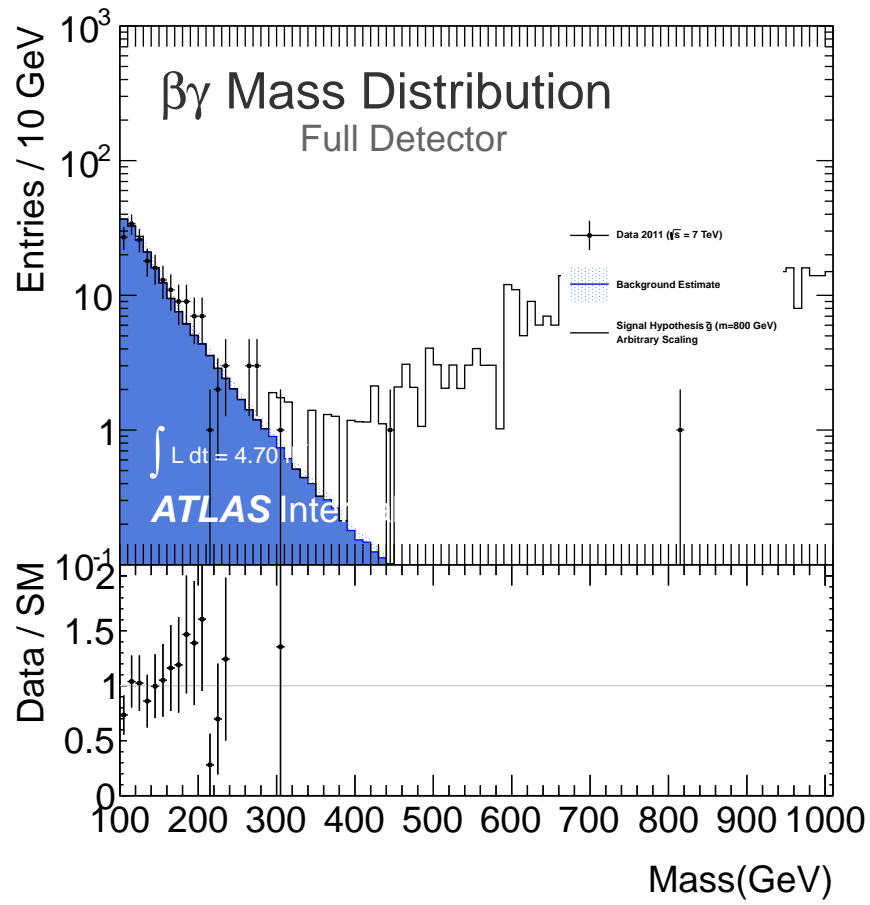


Figure 10.3: Data versus estimated background for the $\beta\gamma$ -mass distributions of 800 GeV *gluino R-hadrons*.

The input to the background generation were all data candidates that passed cut set **I** from above. At this stage there was still so many candidates, that an admixture of true signal would be very small and irrelevant for the validity of this method. A straight sampling from the data distributions of the three estimators did not work since they were all strongly correlated with η . This correlation was taken care of via a binning in η .

Using the data candidates, three 2D histograms were filled with the distributions of

1. β vs. η
2. $\beta\gamma$ vs. η
3. p vs. η .

In all three histograms the η binning consisted of 17 equal bins spanning the range $[-3, 3]$. A pair of random values of p and η were then generated from the distribution in histogram 3. The slices from histograms 1 and 2 that corresponded to this value of η were then used to generate random values of β and $\beta\gamma$ respectively. This method of oversampling was used to generate the distribution of m_β and $m_{\beta\gamma}$ that could be expected if the estimators were indeed independent of each other. Figure 10.4 shows an example of the β , $\beta\gamma$ and p distributions vs. η that were used for background generation in the case of a 500 GeV gluino R -hadron.

In order to get a precise estimate of the number of events that could be expected pass cut set **II** above, the number of background events generated in this way had to be larger than the number of data events. This oversampling could be allowed since the number of possible distinct new combinations of the three generators was $n^3 - n$ where n is the number of candidates that went into the filling of the 2D histograms.

If a true signal is present in the set of input candidates, the method can still be expected to work. If the input set contains a fraction f of true signal, then after the random sampling only f^3 combinations will correspond to recombinations of sets of values coming from signal while $(1 - f)^3$ will come from recombinations of sets of values coming from background (the rest will be a mixture). Given our previous results [7] we knew that the admixture of signal had to be small ($\ll 1\%$). This meant that the amount of background that was falsely generated to be signal-like would also be small ($\ll 10^{-4}\%$).

For our analysis we oversampled the histograms millions of times to obtain a smooth distribution of background mass pairs. In order to compare this background to real data, it had to be scaled down. Merely scaling down by the oversampling factor did not work well in practice which is why a sideband method was employed. The integral of the background distribution that fell inside the cuts $0 < m_{\beta\gamma} < 200$ GeV and $0 < m_\beta < 200$ GeV was

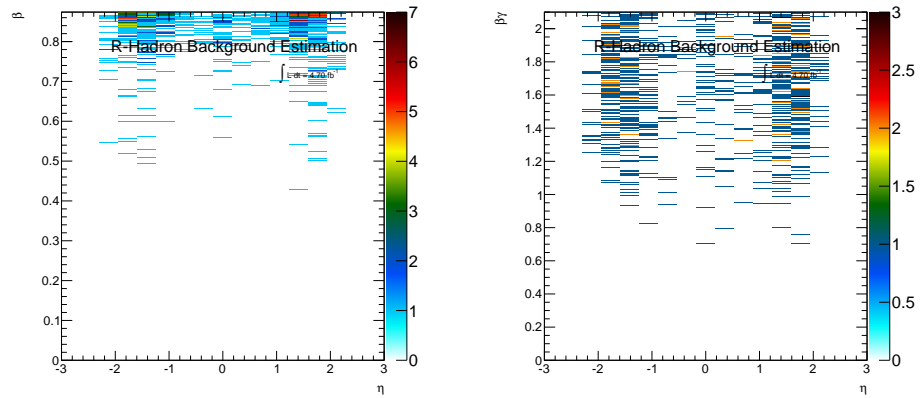
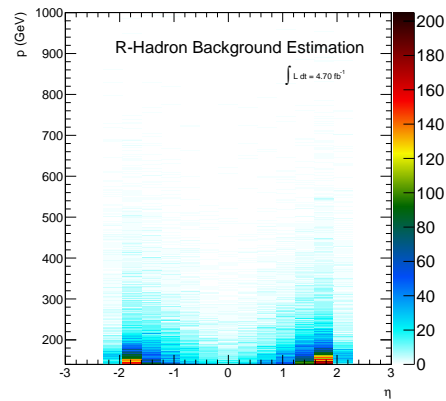
(a) η vs. β (b) η vs. $\beta\gamma$ (c) η vs momentum

Figure 10.4: Input histograms for background estimation. (Example for 500 GeV gluino R-hadron).

compared to the number of data events that fell in the same range. The background distribution was then scaled down to make the integrals match.

After this oversampling and rescaling was done, cut-set **II** was applied to the background distribution to find the expected background count in the signal region.

10.4 Limit Setting

In the exciting hunt for new theories one is quickly reminded that most theories do not in fact reveal new or revolutionary truths about nature. In most analyses, no signal is found.

Far from being uninteresting, these null-results in themselves are important observations. They constrain theories and can guide the direction of new theoretical efforts. One wishes to quantify the degree of importance¹ of a result not least to be able to compare it to earlier studies. What is typically done is to set a limit on the production cross-section of the signal that was searched for. What this limit states is that if the signal does exist and has a production cross-section below this limit, it might simply have evaded detection by being too rare. A signal with a production cross-section above the limit however can be excluded with a stated degree of certainty.

The correct way to set such a limit has been the subject of many debates and a lot of literature exists on the subject. In high energy physics the CL_s [69] limit setting method has been used in practice in most publications from the experiments at LEP and at the Tevatron. In order to produce results that can easily be compared with earlier results from those experiments, it has been decided that ATLAS publications also use the CL_s method.

10.4.1 Derivation of CL_s

The CL_s method gives a frequentist likelihood limit with a degree of certainty that is usually chosen at 95%. This means that at a limit value of x , a signal that has this cross section x evades detection in 5% of all cases. A case can here be taken to be an identical repetition of the experiment at hand where the only things that changes from repetition to repetition are those factors that are influenced by chance. Signals with a cross section larger than x would have a smaller chance of randomly evading detection. The fact that no signal was detected is then seen as unnatural, and the signal is deemed excluded. If the signal has a strength below x , it will have a greater chance of evading detection. The fact that no signal was seen can then be called unlucky, but not unexpected. The signal is in the allowed region.

The inputs to the CL_s method are, in our case, the results of a counting experiment. For data, we observe the number of events that pass all cuts

¹The term ‘significance’ is not used here as it has a special statistical meaning.

and land in the signal region. This is called the observed number. From the generation of background described above, we get, after rescaling, a number that is the expectation for the background in the signal region. From the signal sample we get the efficiency, i.e the chance that a true signal event will be observed in the signal region. This efficiency is used to rescale the signal rate limit found by the CL_s method.

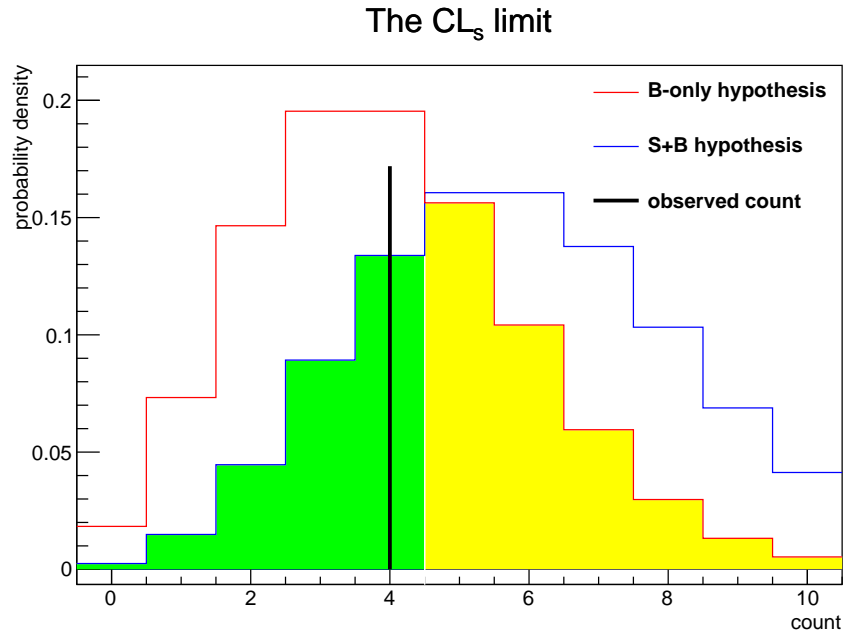


Figure 10.5: The CL_s limit in a counting experiment. Yellow is $1 - L_b$, green is L_{s+b} . In this example $\lambda_b = 4$ and $\lambda_{s+b} = 6$.

CL_s uses the likelihood ratio of two hypotheses. H_0 is the hypothesis that the observed count stems from a distribution that only consists of background (b -only). H_1 is the hypothesis that a certain amount of signal is present ($b + s$). In the case of counting experiments, each hypothesis is described by a poisson distribution with a single parameter, the expected count. One can construct the likelihood of H_0 as the probability that an observation would have produced a signal as low as the observed one or lower by integrating the distribution from 0 up to the observed count. This likelihood is called L_b . Figure 10.5 contains a yellow shading which marks $1 - L_b$. Similarly one can define the likelihood of H_1 as the probability that its distribution would produce an observation this low or lower. Called L_{s+b} this quantity is coloured green in figure 10.5. Using s for the expected number of signal and b for the expected number of background, the confidence limit on s with a given confidence level α is defined as the value of s for which the ratio L_{s+b}/L_b equals α .

The value of the limit is thus defined by the values of b and the observed

count as well as the shape of the probability distribution functions.

In our experiment there are a number of uncertainties that influence the background expectations. Statistical effects arise because the background estimate is based on data. Systematic effects are included to describe the uncertainty of in how far our data driven estimate reflects reality. One therefore wishes to know what kind of limit one would expect in the absence of any signal, but given these uncertainties.

To solve this problem, pseudo-experiments are employed. In a given pseudo-experiment a random value of the true background rate is chosen based on the given uncertainties on the background rate, then an actual number of background events is generated based on this presumed true mean. This actual number of events is then used as an observation and is combined with the nominal background expectation to give the CL_s limit value of the pseudo-experiment. Using many tens of thousands of such pseudo-experiments a distribution of limit values is built up. The central value of this distribution is taken as the expected value. The width of this distribution is used to assess the significance of the actual observed limit value. Other systematic effects, such as uncertainty on the signal efficiency, are also included in the pseudo-experiments.

10.4.2 Implementation

In our search, we had one counting experiment per signal hypothesis. For each such experiment the observed CL_s limit, the expected limit and the spread on the expected limit was determined. We used an existing implementation of the CL_s method in ROOSTATS [70] which already contained the machinery for the generation of pseudo-experiments. The value of α was set at 5% giving 95% limits. The number of pseudo-experiments was set high enough so that any sampling effects were insignificant.

Chapter 11

Results

No indication of signal was found in the signal region of any of our search strategies. We thus proceeded to set cross section limits using the procedure described in section 10.4. The results are shown in figure 11.1 for the full detector search and figure 11.2 for the MS agnostic search. The cross section limit is shown as an expected limit with uncertainties and an observed upper limit. In addition to these experimental results, the figures also contain the cross section predictions with uncertainty for the various models.

The cross section limits are a purely experimental result since we took care in our analysis not to bias our cuts by basing them on any single model. In order to constrain theoretical models however, a lower mass limit on the SMP masses is more useful. A mass limit is set by finding the intersection point between the observed limit curve and the curve of the theoretical prediction minus one sigma. This crossing point is taken as the upper limit of the mass that can be excluded with these results. It should be noted that this limit is entirely dependent on the model that was used for the theoretical cross section calculation. Different models will yield different mass limits. The resulting mass exclusion limits for the cross sections in figures 11.1 and 11.2 are presented in table 11.1.

One reason why our results have a significant impact on a wide group of theories, that all predict some sort of long lived stable charged particle, is that we tried at every step to base our cuts and assumptions on physical intuition wherever possible. We took care not to overtrain our cuts on MC samples by, for example, using neural networks, boosted decision trees or likelihood estimators to guide our selection of cuts as one otherwise might have done.

11.1 Interpretation of Limits

The observed limit can both lie above or below the expected limit. Deviations from the observed from the expected limit within a few standard

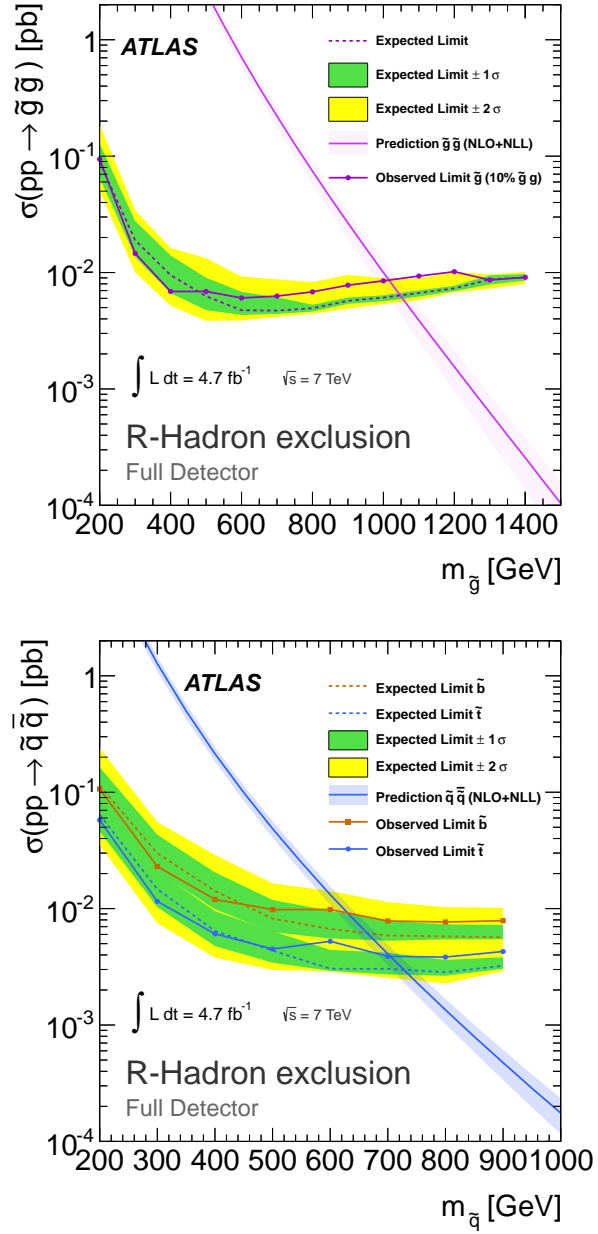


Figure 11.1: Cross-section exclusion limits for both gluino and squark R-hadrons using the full detector reconstruction are shown as the expected limit (dashed line) with ± 1 and $\pm 2\sigma$ uncertainty bands (green and yellow bands respectively) and the observed upper limit (solid line with markers). In the squark plot sbottom limits are drawn in red while stop limits are blue. The solid, rapidly sloping line is the theoretical prediction for the production cross-section.

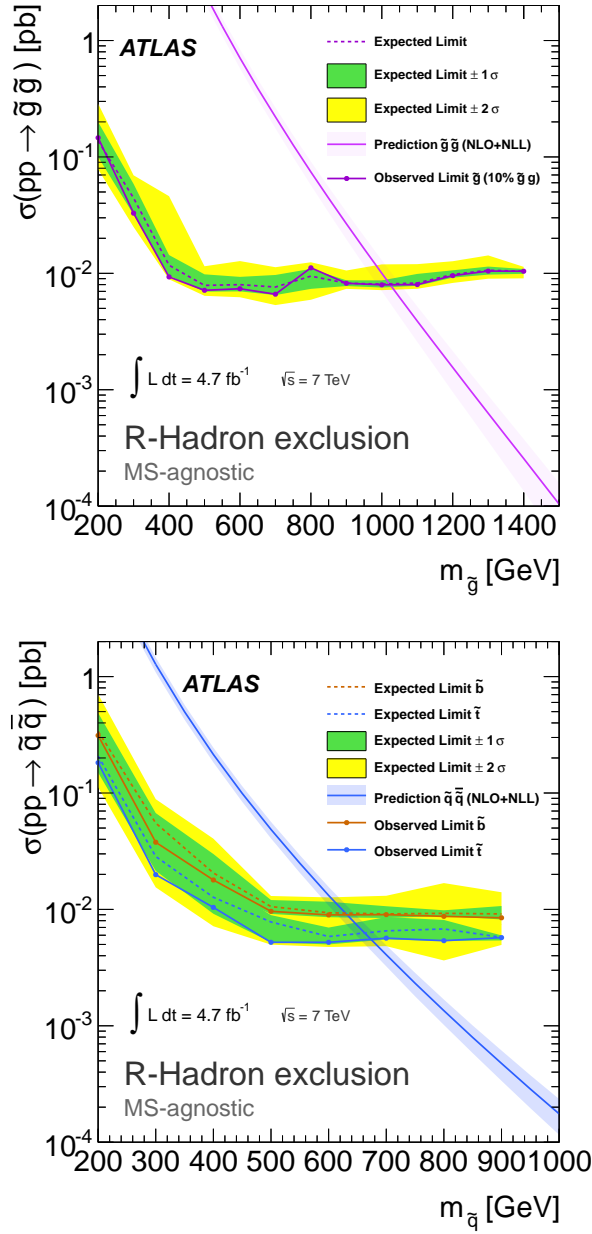


Figure 11.2: Cross-section exclusion limits for both gluino and squark R-hadrons which are neutral in the muon spectrometer. Colours and lines are as in figure 11.1.

SMP	inter. model	full det. limit	MS agnostic limit
gluino \tilde{g}	gener.	985 GeV	989 GeV
stop \tilde{t}	Regge	683 GeV	657 GeV
sbottom \tilde{b}	Regge	612 GeV	618 GeV

Table 11.1: *The mass exclusion limits for the models tested in our search.*

deviations are generally expected and attributed to statistical fluctuations. This is the case in all our limit plots. The closeness of the two means that the background was very well described.

If the observed limit lies significantly below the expected one, this means that the background-only hypothesis does not describe the data very well. If this occurs anywhere on a limit plot, it casts some doubt on the entire limit result, since the background distribution used in this hypothesis also enters in the signal + background distribution of which one is trying to quantify the signal part.

If the fluctuation goes upward, this can indicate the presence of a signal or at least of some signal-like events. Such an upward fluctuation is not sufficient in itself to accept the signal hypothesis, since bad background modelling may also in this case be the cause of the deviation. An upward fluctuation therefore requires a careful attention before one can claim a signal discovery. Since no such indication of signal was found in any of our experiments, we will not now discuss this situation further.

11.2 Comparison to Competing Experiments

ATLAS's competition, the CMS collaboration has also published their findings on a similar search [9]. They found exclusion limits on gluino (scalar top quarks) at 1098 (737) GeV in a full detector search and a limit of 928 (626) GeV if the R -hadrons become neutral before they reach the muon spectrometer. The higher limits set by CMS can be attributed to their ability to trigger on slow muon-like particles, an option that is sadly lacking in ATLAS. Also, the limits by CMS are based on a different calculation of the theoretical cross section. Differences are therefore expected.

11.3 Systematic Uncertainties

This section will give an overview of systematic effects that have partly been touched on in the relevant sections. A summary of the total systematic effects that have been included in our analysis is shown in table 11.2. All systematic uncertainties have been included in the limit setting procedure and are taken into account in the final limits in table 11.1.

Systematic Uncertainties	R -hadrons
Theoretical uncertainty on signal acceptance	15 – 30
Signal efficiency contributions:	
Signal trigger efficiency	4.5
QCD uncertainties (ISR, FSR)	8.5
Signal pre-selection efficiency	1.5
Momentum resolution	1.3
Pixel dE/dx calibration	5
Calorimeter β timing calibration	1.0
MS β timing calibration	3.6
Total uncertainty on signal efficiency	11.6
Luminosity	3.9
Experimental uncertainty on background estimate	15

Table 11.2: Summary of systematic uncertainties (given in percent). Ranges indicate a mass dependence for the given uncertainty (low mass – high mass). From [8].

11.3.1 Theoretical Cross Section

The expected signal cross-sections are calculated at next to leading order (NLO) in the strong coupling constant and soft gluon emission resummation is carried out at next to leading logarithm (NLL) accuracy [71–77]. Uncertainties are obtained as the maximum deviation from the nominal value when using a set of different parton distribution functions, factorisation and renormalisation scales as in reference [78]. For the limit setting the expectation was taken to be the lower edge of the 1σ envelope around the nominal expectation. Depending on the R -hadron mass, the uncertainties involved in this method were found to range between 15 and 30%, increasing with mass.

11.3.2 Expected Signal

The systematic effects associated with signal selection were studied in some detail as specified in table 11.2.

Signal trigger efficiencies were studied using the $Z \rightarrow \mu\mu$ calibration sample. Since the calorimeter E_T sum is blind to muon energy, boosted Z , triggered by muon triggers, can be used to construct the trigger turn on curve as shown in figure 6.2. The signal efficiency is obtained by multiplying the true generated E_T^{miss} by the turn-on curve bin by bin. To obtain the uncertainty, the fitted turn-on curve is varied by varying every fit parameter within $\pm 1\sigma$. The resulting variations revealed a 4.5% systematic uncertainty on the signal trigger efficiency.

Effects of uncertainties in the amount of initial state radiation (ISR) and

final state radiation (FSR) on the final signal selection were studied. This was done by simulating samples of gluino R -hadron with higher and lower amounts of QCD radiation than expected. The effect contributed 8.5 %.

The effect of momentum resolution uncertainties was estimated to be up to 1.3 %. The pixel dE/dx uncertainty was estimated by comparing the dE/dx values for high p_T muons from $Z \rightarrow \mu\mu$ in data and MC. The value of 5 % was used as a conservative upper limit on the uncertainty.

Effects on the β measurements were investigated by smearing all timings by an amount equal to the width of the timing distribution. This resulted in the given systematic effect for calorimeter and MS β values.

11.3.3 Background Estimation

The uncertainty on the background estimate was found by varying the cuts and binning that were used to select the sideband regions in chapter 10. It was found to be 15 %.

Chapter 12

Outlook & Discussion

Checking for the existence of long-lived stable massive particles is an important part of the ongoing search for Supersymmetry as discussed in chapter 3. As long as there is new data available to ATLAS there will always be searches for new stable particles. Future analyses will have the opportunity to revisit some of the assumptions that we have had to make in our analysis, but will also have to face a range of new challenges.

12.1 Looking Back

There are several parts of our analysis that I would like to revisit given the knowledge that I have gained through this work.

12.1.1 Calibration

The timing calibration of the calorimeters and muon chambers can probably still be substantially improved. The calibration granularity for the calorimeters was in large parts determined by the availability of a clean sample of muons. The choice of muons from $Z \rightarrow \mu\mu$ decays has severely limited the available statistics. Since we realised that the timing is not substantially affected by the particle nature underlying the calibration tracks, it could be possible to use all muon candidates, or even all available tracks to calibrate the timing biases and widths. The step to using all muon candidates for the MS calibration was a late development and which is why it was not used for the calorimeters.

With an increased calibration sample it will be possible to calibrate in several new dimensions such as

- within runs as a function of bunch-crossing / Lumi-block
- with respect to ϕ
- a much finer binning in η

- or alternatively to the last two points, calibrating every single cell of the calorimeters separately.

The advantage of better timing resolution is to be able to set limits on much lower mass hypotheses. Also, it may be possible to lower some of the quality cuts that we used in our analysis and thus get a better signal efficiency.

12.1.2 Trigger

The choice of trigger menu should be revisited. Throughout our analysis we shied away from using pre-scaled trigger menus because of the enormous additional complexity in evaluating the total luminosity when setting a limit. The additional complexity may be large, but the possible gains would be

- a better discovery potential/better signal limits
- additional knowledge of the trigger acceptance on SMPs that could guide future efforts to develop more specific triggers.

Once the additional challenges have been mastered, all available triggers menus could be included, resulting in possibly significant increases of the signal acceptance.

12.1.3 MC Charge-Flip Truth

At the moment the structure of our simulation software does not allow us to pass on truth information about the interactions of particles in the outer parts of the detectors. If such information were available to us, analyses could be developed and tuned to look for such events specifically. Since charge-flips should happen mostly in the calorimeters, a charge-flip might be apparent by a reversed charge of a track in the muon spectrometer with respect to the inner detector. This will of course need to be checked once the relevant MC samples are available.

12.1.4 Flight Path Length

In retrospect it would have been trivial to take the path length in the ToF measurement to start at the primary vertex instead of the detector origin. The systematic effect of 1.7% from this, as given in section 7.3.1, could then have been avoided.

It might also be worth investigating if using the inner edge of a cell instead of the cell centre as the end point could give better results.

12.2 Looking Ahead

There are a range of issues that will need to be addressed before the full $\sqrt{s} = 8$ TeV data set collected in 2012 can be included in this analysis, such as pile-up and rising trigger levels. An even greater challenge will be to move forward to after the long LHC shutdown (foreseen to end in 2015) when event rates and energies will be much higher.

12.2.1 LHC Schedule

The current schedule for the immediate future of LHC running foresees an end of proton-proton physics at the end of this year 2012. After a few months with proton-ion collisions, a long shutdown of the LHC is foreseen from February 2013 until November 2014. During this period extensive overhauls of the LHC magnets are foreseen as well as maintenance and/or upgrades of almost all other areas of the accelerator and detectors. After this long shutdown it is expected that the LHC will be able to produce collisions at, or close to, the design energy of 14 TeV. In addition, the bunch spacing is expected to be reduced to the design value of 25 ns from the current value of 50 ns.

12.2.2 Mass Reach

One of the immediate consequence of the increased collision energy will be the possibility of creating particles of higher mass. Because of this, a new R -hadron search will necessarily have to be launched to find such particles or to extend the current mass limit.

12.2.3 Pile-Up

The overlap of several collisions in a single bunch crossing, called pile-up (PU), will cause problems in several ways:

- larger rates of jets and other trigger objects will cause trigger levels to be raised
- during selection we currently reject candidate that lie too close to a reconstructed jet or where cells in the inner detector are known to be shared with another track. This cut may need to be revisited.

12.2.4 Trigger

With ever increasing levels of the missing transverse energy triggers it becomes ever more important to look at including the pre-scaled trigger menus to maximise the signal acceptance.

With respect to the long shutdown of the LHC which is expected to last almost two years one frequently hears that this will be a time to thoroughly examine the data without the pressure of constantly new data. For the search of R -hadrons though I believe that it would be important to carry out a number of full pile-up trigger studies early on to see what kind of trigger efficiency can be expected.

It may well be necessary to look at alternative triggering strategies if R -hadron searches are to be competitive after the shutdown. With 25 ns bunch spacing, slow muon triggers may not be feasible, but it might be possible to pursue other strategies.

12.2.5 Time of Flight

It will be very challenging to determine the effect of the lower bunch spacing after the long shutdown (expected to be 25 ns). The effects may range from mis-timed triggers, SMPs appearing in unrelated events, detector effects etc. Certainly all timing calibration methods will need to be revisited.

To truly assess the impact of the event rate it may be necessary to carry out full simulations of R -hadron events embedded in trains of several consecutive bunch-crossings. This will presumably be an extremely computation intensive task.

Appendix A

Additional Figures

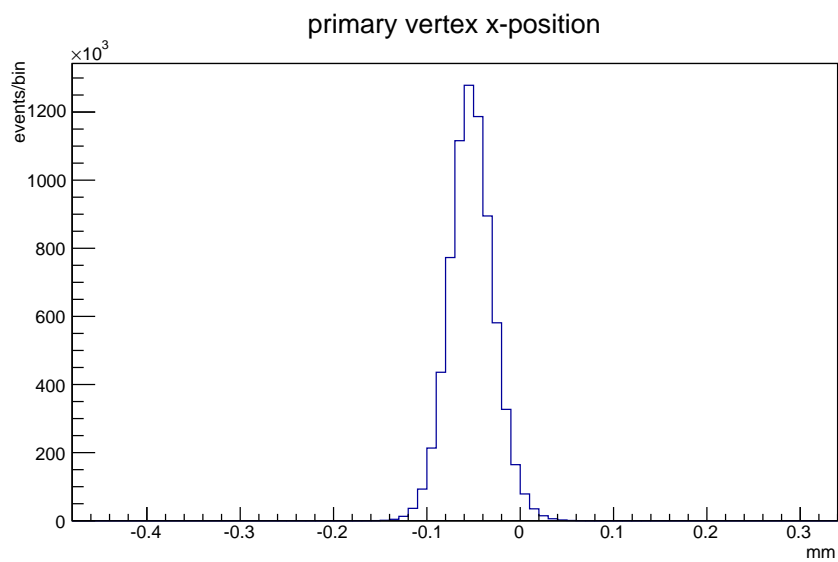


Figure A.1: *The x-positions of primary vertices in good events in the JetTauEt-Miss stream.*

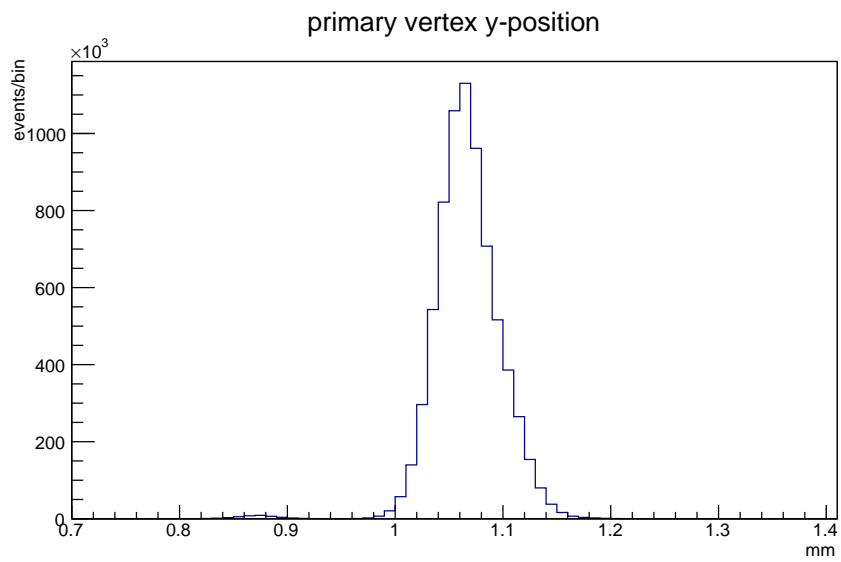


Figure A.2: *The y-positions of primary vertices in good events in the JetTauEt-Miss stream.*

List of Figures

2.1	The higgs free propagator is not protected from picking up arbitrarily large mass corrections from fermion or boson loops like this.	24
2.2	The present energy content of the universe as obtained from cosmological models.	25
3.1	<i>R</i> -hadron-proton scattering processes. (a) Elastic scattering, (b) Inelastic scattering leading to baryon and charge exchange, (c) Inelastic scattering leading to charge exchange, (d) Resonance formation. Figure taken from [24]	38
4.1	quadrupole cell	40
4.2	dipole magnet effect	41
4.3	The layout of the CERN accelerator complex [42].	41
4.4	The CTEQ6M parton distribution function at $Q^2 = 2$ and 100 GeV^2 . Provided by [45].	43
4.5	The cross-sections and expected rates of various processes against the collision energy. For comparison, the cross-section limit that was set with our analysis has been added. Figure from [46].	45
5.1	A cutaway of the ATLAS detector shows the layout of the sub-detectors. The total height 25 m, the length is 44 m. Figure from [47].	48
5.2	The atlas magnet system consists of a solenoid and three toroid systems. Figure from [47].	49
5.3	An overview of the ATLAS inner detector from [48].	50
5.4	A detailed view of the layout of the inner detector. Tracking is possible out to $ \eta < 2.5$. Figure from ATLAS detector paper [47].	51
5.5	The graph of the Bethe-Bloch formula for the special case of muons impacting on copper. The monotonously falling region between $0.25 < \beta\gamma < 1$ will be used to convert the measured specific ionisation to $\beta\gamma$. Figure from [49].	52

5.6	Distribution of dE/dx versus signed momentum for minimum bias collisions and in the case of three good cluster tracks. In this data sample from 2010 collisions, tracks are reconstructed down to 100 MeV of transverse momentum. The distribution of the most probable value for the fitted probability density functions of pions (black), kaons (grey) and protons (blue) are superimposed. Figure taken from [8].	53
5.7	An illustration of terms when talking about a TRT track. A track contains LT and HT hits. Some straws may be dead and some hits may be deemed outliers by the tracking algorithm. Note, the straw diameters are not to scale.	55
5.8	Simulation of the electron drift in a TRT straw with a 2 T magnetic field pointing out of the plane of the paper. Figure from [51]. For a discussion of the direction of the magnetic field, see section 5.6.3.	56
5.9	An illustration of how the TRT signals are digitised. The LT is sampled 8 times per bunch crossing (BC), the HT only once. Three BC are recorded for each hit. Figure from [52].	56
5.10	The path of an electron in the TRT gas will be bent in a sense that is opposite to the curl expected from a free electron. The size of θ in figure (b) will vary, but its direction is never reversed.	57
5.11	The relation between track-wire distance and drift time. Also shown is the fit to the average drift times that is used for tracking. Figure from [54].	58
5.12	The onset of transition radiation as a function of the γ factor is shown by samples of electrons and pions in the TRT end-cap in 2010 data. Figure from [54].	59
5.13	An example result of the double binomial fit in a slice of $ \eta < 0.44$, $12.6 \text{ GeV} < p < 31.7 \text{ GeV}$ for $N_{\text{hit}} = 32$ using an MC sample of tracks that have passed loose electron identification cuts.	62
5.14	The situation in the TRT straw for a minimum ionising (top) and a highly ionising track (bottom). The furthest cluster will have a larger distance from the straw wall in lower ionising tracks.	64
5.15	The best corrected estimator of the specific ionisation of tracks in the TRT as formed from the signal time over threshold of all TRT hits. Figure taken from public TRT results [54].	65
5.16	An overview of the calorimeters in the ATLAS detector. Figure from [47].	67
5.17	Amplitude versus time for a triangular pulse of the current in a LAr barrel electromagnetic cell and of the front end board output after shaping. The sampling points every 25 ns are indicated. [47]	68

5.18	A cut-away view of the ATLAS muon spectrometer. The toroid magnets are shown in yellow while the detection elements are coloured in shades of blue. Figure from [47].	69
5.19	Trigger flow. Figure from [56].	70
6.1	The integrated collected luminosity as a function of date in 2011. The high data taking efficiency of ATLAS is apparent from the smallness of the green band.	79
6.2	Turn-on curve for the xe60_verytight_noMu (left) and xe70_noMu (right) trigger chain in $Z \rightarrow \mu\mu$ data (black dots) and in MC, before (red squares) and after (blue triangles) pile-up re-weighting.	81
6.3	Efficiency of the muon trigger for GMSB events as a function of $\tilde{\tau}$ mass	82
6.4	The β distribution for 800 GeV R -hadrons measured with the calorimeter using muons (blue) and jets (red) for the calibration. The distributions are in good agreement.	87
7.1	The distribution of deviations from the expected hit time for all calorimeter cells for the calibration sample. The MC distribution has been scaled to have the same maximum as the data distribution. Error-bars are included.	90
7.2	The distribution of deviations from the expected hit time for all RPC chambers for the calibration sample. Otherwise as in figure 7.1.	91
7.3	The distribution of deviations from the expected hit time for all MDT chambers for the calibration sample. Otherwise as in figure 7.1.	91
7.4	This plot shows the proton mass as measured via the dE/dx method by the pixel detector plotted as a function of run-period. The nominal proton mass is shown as the red dashed line. The stability demonstrates the viability of a mass measurement with the pixel detector. Figure from [4].	93
7.5	An example event with a high number of pile-up vertices viewed in the $y - z$ plane. Shown is the interaction region only. The horizontal size of the interaction region is about 7 cm	95
7.6	The z -positions of primary vertices in good events in the JetTauEtMiss stream.	96
7.7	The run-average of all uncalibrated calorimeter Δt plotted as a function of run number in the calibration sample.	99

7.8	The variation of all uncalibrated calorimeter detection Δt in run number 189425 in period L. No clear trend can be seen in either the variation between different bunches (top) or in change from one lumi-block to another (bottom). These two dimensions were not used in calibration.	100
7.9	The outline of the calibration procedure. The procedure is tightly coupled with the β combination strategy described in section 8.3.	102
7.10	The distribution of deviations from the expected hit time for all calorimeter cells for the calibration sample before and after the calibration procedure. The MC distributions have been scaled to have the same maximum as the corresponding data distribution. Error-bars are included.	106
7.11	The distribution of deviations from the expected hit time for all RPC chambers for the calibration sample. Otherwise as in figure 7.10.	107
7.12	The distribution of deviations from the expected hit time for all MDT chambers for the calibration sample. Otherwise as in figure 7.10.	107
8.1	The correlation plots for β values from different sub-detectors for the calibration sample. All calibration muons have $\beta_{\text{true}} = 1$. Deviations from this are scaled with the estimated error giving the pull distributions. The low correlation coefficients confirm the assumption of independent estimators.	112
9.1	The ΔR separation of 900 GeV R -hadrons from the nearest jet. An R -hadron's calorimeter energy deposit can itself be identified as a jet. Hence the jet energy cut of 40 GeV is needed before the distance to the nearest real jet can be found.	124
9.2	The distribution of true absolute pseudorapidity for 900 GeV R -hadrons.	125
9.3	The relative tracking resolution versus η for muons of various momenta. Figure from [47].	126
10.1	An illustration of how the signal region will be defined in the m_β vs $m_{\beta\gamma}$ plot.	130
10.2	Data versus estimated background for the β -mass distributions of 800 GeV gluino R -hadrons.	131
10.3	Data versus estimated background for the $\beta\gamma$ -mass distributions of 800 GeV gluino R -hadrons.	132
10.4	Input histograms for background estimation. (Example for 500 GeV gluino R -hadron).	134

10.5	The CL_s limit in a counting experiment. Yellow is $1 - L_b$, green is L_{s+b} . In this example $\lambda_b = 4$ and $\lambda_{s+b} = 6$	136
11.1	Cross-section exclusion limits for both gluino and squark R -hadrons using the full detector reconstruction are shown as the expected limit (dashed line) with ± 1 and $\pm 2\sigma$ uncertainty bands (green and yellow bands respectively) and the observed upper limit (solid line with markers). In the squark plot sbottom limits are drawn in red while stop limits are blue. The solid, rapidly sloping line is the theoretical prediction for the production cross-section.	140
11.2	Cross-section exclusion limits for both gluino and squark R -hadrons which are neutral in the muon spectrometer. Colours and lines are as in figure 11.1.	141
A.1	The x-positions of primary vertices in good events in the JetTauEtMiss stream.	149
A.2	The y-positions of primary vertices in good events in the JetTauEtMiss stream.	150

List of Tables

2.1	Summary of elementary fermions	20
2.2	Summary of elementary bosons	20
2.3	Particles that appear as stable products at collisions at the LHC. Notice that the largest distance of an ATLAS sub-detector from the interaction point is about 25 m, the closest distance of the calorimeters to the collisions is about 1.5 m. In this analysis particles down to 5 GeV were used, so 10 GeV is a representative particle energy. All of these particles can be detected directly by ATLAS before they decay. Anti-partners are not listed separately.	21
3.1	Brief overview of possible SUSY SMP states considered in the literature. Classified by SMP,LSP,scenario, and typical conditions for this case to materialise in the given scenario. Table from [24].	32
3.2	Predictions from PYTHIA of the fractions of different species of R -hadrons following the hadronisation of a gluino (left) and a stop (right) of mass 500 GeV produced at the LHC. The HERWIG gluino predictions are for a 2000 GeV mass, but almost identical for 50 GeV. (Taken from [24])	37
5.1	The run periods that were used for our analysis.	75
6.1	Trigger menus utilised in this analysis along with an indication in which data taking periods they were used.	79
6.2	The available R -hadron signal samples in our analysis. The samples differ in the supersymmetric species contained in the R -hadrons (SMP). Effects of the the interaction model (generic, Regge or intermediate) were not investigated as they were previously found to be small [7]. The production channel determines the η distribution. All mass ranges are in steps of 100 GeV.	84
6.3	Fraction of data and corresponding MC for each run period group.	85

9.1	Quality selection cut-flow table from the full detector search for three example \tilde{g} masses hypotheses. Both ID and CB selection are shown. All numbers are percentages of the total generated number. The cutflow is per event in each category. Some events have both types of candidates, and hence the individual number do not add up to the total.	122
9.2	Quality selection cut-flow table from the MS agnostic search for three example \tilde{g} masses hypotheses. All numbers are percentages of the total generated number.	123
11.1	The mass exclusion limits for the models tested in our search.	142
11.2	Summary of systematic uncertainties (given in percent). Ranges indicate a mass dependence for the given uncertainty (low mass – high mass). From [8].	143

Bibliography

- [1] R. Mackeprang and J. R. Hansen, *Stable Heavy Hadrons in ATLAS*. *oai:cds.cern.ch:1385016*. PhD thesis, Copenhagen U., Copenhagen, 2007. Presented 05 Oct 2007.
- [2] A. C. Kraan, *Interactions and Detection of R-hadrons*. PhD thesis, Niels Bohr Institute, University of Copenhagen, Nov, 2004.
- [3] C. Ohm, D. Milstead, and T. Moa, *Searches for exotic stable massive particles with the ATLAS experiment*. *oai:cds.cern.ch:1397376*. PhD thesis, Stockholm U., Stockholm, 2011. Presented 04 Nov 2011.
- [4] *Search for charged long-lived heavy particles with the ATLAS Experiment at the LHC*, Tech. Rep. ATLAS-CONF-2012-022, CERN, Geneva, Mar, 2012.
- [5] ATLAS Collaboration, G. Aad et al., *Search for Heavy Long-Lived Charged Particles with the ATLAS detector in pp collisions at $\sqrt{s} = 7$ TeV*, Phys.Lett. **B703** (2011) 428–446, arXiv:1106.4495 [hep-ex].
- [6] ATLAS Collaboration, G. Aad et al., *Search for Massive Long-lived Highly Ionising Particles with the ATLAS Detector at the LHC*, Phys.Lett. **B698** (2011) 353–370, arXiv:1102.0459 [hep-ex].
- [7] ATLAS Collaboration, G. Aad et al., *Search for stable hadronising squarks and gluinos with the ATLAS experiment at the LHC*, Phys.Lett. **B701** (2011) 1–19, arXiv:1103.1984 [hep-ex].
- [8] ATLAS Collaboration, G. Aad et al., *Searches for heavy long-lived sleptons and R-Hadrons with the ATLAS detector in pp collisions at $\sqrt{s} = 7$ TeV*, arXiv:1211.1597 [hep-ex].
- [9] CMS Collaboration, S. Chatrchyan et al., *Search for heavy long-lived charged particles in pp collisions at $\sqrt{s}=7$ TeV*, Phys.Lett. **B713** (2012) 408–433, arXiv:1205.0272 [hep-ex].

- [10] D0 Collaboration, V. M. Abazov et al., *Search for Charged Massive Long-Lived Particles*, Phys. Rev. Lett. **108** (2012) 121802. <http://link.aps.org/doi/10.1103/PhysRevLett.108.121802>.
- [11] CDF Collaboration, T. Aaltonen et al., *Search for Long-Lived Massive Charged Particles in 1.96 TeV $\bar{p}p$ Collisions*, Phys. Rev. Lett. **103** (2009) 021802, [arXiv:0902.1266](https://arxiv.org/abs/0902.1266) [hep-ex].
- [12] ATLAS Collaboration, G. Aad et al., *Observation of a new particle in the search for the Standard Model Higgs boson with the ATLAS detector at the LHC*, Phys.Lett.B (2012) , [arXiv:1207.7214](https://arxiv.org/abs/1207.7214) [hep-ex].
- [13] CMS Collaboration, S. Chatrchyan et al., *Observation of a new boson at a mass of 125 GeV with the CMS experiment at the LHC*, Phys.Lett.B (2012) , [arXiv:1207.7235](https://arxiv.org/abs/1207.7235) [hep-ex].
- [14] B. Andersson, G. Gustafson, G. Ingelman, and T. Sjostrand, *Parton Fragmentation and String Dynamics*, Phys.Rept. **97** (1983) 31–145.
- [15] T. Sjostrand, S. Mrenna, and P. Z. Skands, *PYTHIA 6.4 Physics and Manual*, JHEP **0605** (2006) 026, [arXiv:hep-ph/0603175](https://arxiv.org/abs/hep-ph/0603175) [hep-ph].
- [16] Atlas Collaboration Collaboration, G. Aad et al., *Study of Jet Shapes in Inclusive Jet Production in pp Collisions at $\sqrt{s} = 7$ TeV using the ATLAS Detector*, Phys.Rev. **D83** (2011) 052003, [arXiv:1101.0070](https://arxiv.org/abs/1101.0070) [hep-ex].
- [17] R. Corke and T. Sjostrand, *Multiparton Interactions with an x -dependent Proton Size*, JHEP **1105** (2011) 009, [arXiv:1101.5953](https://arxiv.org/abs/1101.5953) [hep-ph].
- [18] T. Aoyama, M. Hayakawa, T. Kinoshita, and M. Nio, *Revised value of the eighth-order QED contribution to the anomalous magnetic moment of the electron*, Phys. Rev. D **77** (2008) 053012. <http://link.aps.org/doi/10.1103/PhysRevD.77.053012>.
- [19] D. Hanneke, S. Fogwell Hoogerheide, and G. Gabrielse, *Cavity control of a single-electron quantum cyclotron: Measuring the electron magnetic moment*, Physical Review A **83** (2011) no. 5, 052122, [arXiv:1009.4831](https://arxiv.org/abs/1009.4831) [physics.atom-ph].
- [20] C. Anderson, *THE POSITIVE ELECTRON*, Phys.Rev. **43** (1933) 491–494.
- [21] G. Dobrychev, P. Nedelec, D. Sillou, G. Gribakin, H. Walters, et al., *Proposal for the AEGIS experiment at the CERN Antiproton*

- Decelerator (Antimatter Experiment: Gravity, Interferometry, Spectroscopy)*, .
- [22] S. Dimopoulos and H. Georgi, *Softly Broken Supersymmetry and $SU(5)$* , Nucl.Phys. **B193** (1981) 150.
- [23] Super-Kamiokande Collaboration Collaboration, H. Nishino et al., *Search for Proton Decay via $p \rightarrow e^+\pi^0$ and $p \rightarrow \mu^+\pi^0$ in a Large Water Cherenkov Detector*, Phys.Rev.Lett. **102** (2009) 141801, arXiv:0903.0676 [hep-ex].
- [24] M. Fairbairn, A. Kraan, D. Milstead, T. Sjostrand, P. Z. Skands, et al., *Stable massive particles at colliders*, Phys.Rept. **438** (2007) 1–63, arXiv:hep-ph/0611040 [hep-ph].
- [25] J. A. Conley, J. S. Gainer, J. L. Hewett, M. P. Le, and T. G. Rizzo, *Supersymmetry Without Prejudice at the LHC*, Eur.Phys.J. **C71** (2011) 1697, arXiv:1009.2539 [hep-ph].
- [26] M. Dine, A. E. Nelson, and Y. Shirman, *Low-energy dynamical supersymmetry breaking simplified*, Phys.Rev. **D51** (1995) 1362–1370, arXiv:hep-ph/9408384 [hep-ph].
- [27] P. Fayet, *Mixing Between Gravitational and Weak Interactions Through the Massive Gravitino*, Phys.Lett. **B70** (1977) 461.
- [28] G. F. Giudice, M. A. Luty, H. Murayama, and R. Rattazzi, *Gaugino mass without singlets*, JHEP **9812** (1998) 027, arXiv:hep-ph/9810442 [hep-ph].
- [29] L. Randall and R. Sundrum, *Out of this world supersymmetry breaking*, Nucl.Phys. **B557** (1999) 79–118, arXiv:hep-th/9810155 [hep-th].
- [30] W. Buchmuller, K. Hamaguchi, and J. Kersten, *The Gravitino in gaugino mediation*, Phys.Lett. **B632** (2006) 366–370, arXiv:hep-ph/0506105 [hep-ph].
- [31] J. L. Feng, S. Su, and F. Takayama, *Supergravity with a gravitino LSP*, Phys.Rev. **D70** (2004) 075019, arXiv:hep-ph/0404231 [hep-ph].
- [32] S. Raby, *Gauge mediated SUSY breaking at an intermediate scale*, Phys.Rev. **D56** (1997) 2852–2860, arXiv:hep-ph/9702299 [hep-ph].
- [33] H. Baer, K.-m. Cheung, and J. F. Gunion, *A Heavy gluino as the lightest supersymmetric particle*, Phys.Rev. **D59** (1999) 075002, arXiv:hep-ph/9806361 [hep-ph].

- [34] A. Mafi and S. Raby, *A Solution to the mu problem in the presence of a heavy gluino LSP*, Phys.Rev. **D63** (2001) 055010, arXiv:hep-ph/0009202 [hep-ph].
- [35] S. Raby, *Gauge mediated SUSY breaking with a gluino LSP*, Phys.Lett. **B422** (1998) 158–162, arXiv:hep-ph/9712254 [hep-ph].
- [36] A. Mafi and S. Raby, *An Analysis of a heavy gluino LSP at CDF: The Heavy gluino window*, Phys.Rev. **D62** (2000) 035003, arXiv:hep-ph/9912436 [hep-ph].
- [37] A. C. Kraan, *Interactions of heavy stable hadronizing particles*, Eur.Phys.J. **C37** (2004) 91–104, arXiv:hep-ex/0404001 [hep-ex].
- [38] M. Bahr, S. Gieseke, M. Gigg, D. Grellscheid, K. Hamilton, et al., *Herwig++ Physics and Manual*, Eur.Phys.J. **C58** (2008) 639–707, arXiv:0803.0883 [hep-ph].
- [39] D. Casadei, T. Cornelissen, C. Gay, K. Grahn, C. Gemme, S. Hellman, E. Klinkby, C. Marino, R. Mackeprang, P. Mermod, W. Mills, D. Milstead, C. Ohm, H. Ogren, T. Petersen, A. Pinder, M. Joergensen, L. Rossi, and D. Zieminska, *Search for Stable Hadronising Squarks and Gluinos at the ATLAS Experiment at the LHC*, .
- [40] Evans, Lyndon, (ed.) and Bryant, Philip, (ed.), *LHC Machine*, JINST **3** (2008) S08001.
- [41] J.-L. Caron, *Magnetic field induced by the LHC dipole's superconducting coils.. Champ magnetique cree par les bobines superconductrices des aimants dipolaires du LHC.*, AC Collection. Legacy of AC. Pictures from 1992 to 2002., Mar, 1998.
- [42] C. Lefèvre, *The CERN accelerator complex. Complexe des accélérateurs du CERN*, Dec, 2008.
- [43] H.-L. Lai, M. Guzzi, J. Huston, Z. Li, P. M. Nadolsky, et al., *New parton distributions for collider physics*, Phys.Rev. **D82** (2010) 074024, arXiv:1007.2241 [hep-ph].
- [44] A. Martin, W. Stirling, R. Thorne, and G. Watt, *Parton distributions for the LHC*, Eur.Phys.J. **C63** (2009) 189–285, arXiv:0901.0002 [hep-ph].
- [45] *The Durham HepData Project Online PDF Plotter*.
<http://hepdata.cedar.ac.uk/pdf/pdf3.html>.

- [46] P. Jenni, M. Nessi, M. Nordberg, and K. Smith, *ATLAS high-level trigger, data-acquisition and controls: Technical Design Report*. Technical Design Report ATLAS. CERN, Geneva, 2003.
- [47] ATLAS Collaboration, G. Aad et al., *The ATLAS Experiment at the CERN Large Hadron Collider*, JINST **3** (2008) S08003.
- [48] ATLAS Collaboration, *ATLAS Public Images*, .
www.atlas.ch/photos/.
- [49] Particle Data Group Collaboration, J. Beringer et al., *Review of Particle Physics (RPP)*, Phys.Rev. **D86** (2012) 010001.
- [50] L. Landau, *On the energy loss of fast particles by ionization*, J.Phys.(USSR) **8** (1944) 201–205.
- [51] E. Klinkby and J. D. Hansen, *W mass measurement and simulation of the Transition Radiation Tracker at the ATLAS experiment*.
[oai:cds.cern.ch:1123367](https://cds.cern.ch/record/1123367). PhD thesis, Univ. Copenhagen, Copenhagen, 2008. Presented on 02 Jul 2008.
- [52] P. Wagner, *Performance of the ATLAS transition radiation tracker readout with high energy collisions at the LHC*, Nuclear Instruments and Methods in Physics Research Section A: Accelerators, Spectrometers, Detectors and Associated Equipment (2012) no. 0, –.
<http://www.sciencedirect.com/science/article/pii/S0168900212005086>.
- [53] A. Preisert and F. Sauli, *Drift and Diffusion of Electrons in Gases: a Compilation*, CERN Report 84-08 (1984) .
- [54] ATLAS Collaboration, *ATLAS TRT Public results page*, .
<https://twiki.cern.ch/twiki/bin/view/AtlasPublic/TRTPublicResults>.
- [55] T. Schönfeldt, *Electron identification with the ATLAS TRT*, Master’s thesis, Niels Bohr Institute, Copenhagen U., 2010.
- [56] *ATLAS detector and physics performance: Technical Design Report, 1*. Technical Design Report ATLAS. CERN, Geneva, 1999.
- [57] ATLAS Collaboration Collaboration, G. Aad et al., *Luminosity Determination in pp Collisions at sqrt(s)=7 TeV Using the ATLAS Detector at the LHC*, Eur.Phys.J. **C71** (2011) 1630,
[arXiv:1101.2185](https://arxiv.org/abs/1101.2185) [hep-ex].
- [58] P. Calafiura, W. Lavrijsen, C. Leggett, M. Marino, and D. Quarrie, *The athena control framework in production, new developments and lessons learned*, .

- [59] R. Brun and F. Rademakers, *ROOT: An object oriented data analysis framework*, Nucl.Instrum.Meth. **A389** (1997) 81–86.
- [60] M. Ballintijn, R. Brun, F. Rademakers, and G. Roland, *The PROOF Distributed Parallel Analysis Framework based on ROOT*, ArXiv Physics e-prints (2003) , arXiv:physics/0306110.
- [61] J. Allison, K. Amako, J. Apostolakis, H. Araujo, P. Dubois, et al., *Geant4 developments and applications*, IEEE Trans.Nucl.Sci. **53** (2006) 270.
- [62] M. Asai, *Geant4 - a simulation toolkit*, Trans.Amer.Nucl.Soc. **95** (2006) 757.
- [63] J. E. Gaiser, *Charmonium Spectroscopy from Radiative Decays of the J/ψ and ψ'* . PhD thesis, 1982.
- [64] ATLAS Collaboration Collaboration, G. Aad et al., *Search for anomaly-mediated supersymmetry breaking with the ATLAS detector based on a disappearing-track signature in pp collisions at $\sqrt{s} = 7$ TeV*, Eur.Phys.J. **C72** (2012) 1993, arXiv:1202.4847 [hep-ex].
- [65] ATLAS Collaboration Collaboration, G. Aad et al., *Search for decays of stopped, long-lived particles from 7 TeV pp collisions with the ATLAS detector*, Eur.Phys.J. **C72** (2012) 1965, arXiv:1201.5595 [hep-ex].
- [66] M. D. Joergensen and J. B. Hansen, *Search for long lived massive particles with the ATLAS detector at the LHC*. oai:cds.cern.ch:1370233, Master's thesis, Bohr Inst., Copenhagen, 2011. Presented 06 Feb 2011.
- [67] E. W. Weisstein, "Uniform Product Distribution.", From MathWorld—A Wolfram Web Resource. . <http://mathworld.wolfram.com/UniformProductDistribution.html>.
- [68] G. Cowan, K. Cranmer, E. Gross, and O. Vitells, *Asymptotic formulae for likelihood-based tests of new physics*, European Physical Journal C **71** (2011) 1554, arXiv:1007.1727 [physics.data-an].
- [69] A. L. Read, *Presentation of search results: The $CL(s)$ technique*, J.Phys. **G28** (2002) 2693–2704.
- [70] RooStats Team Collaboration, G. Schott, *RooStats for Searches*, arXiv:1203.1547 [physics.data-an].
- [71] W. Beenakker, R. Hopker, M. Spira, and P. M. Zerwas, *Squark and gluino production at hadron colliders*, Nucl. Phys. **B492** (1997) 51–103, arXiv:hep-ph/9610490.

- [72] W. Beenakker, M. Kramer, T. Plehn, M. Spira, and P. M. Zerwas, *Stop production at hadron colliders*, Nucl. Phys. **B515** (1998) 3–14, hep-ph/9710451.
- [73] A. Kulesza and L. Motyka, *Threshold resummation for squark-antisquark and gluino-pair production at the LHC*, Phys. Rev. Lett. **102** (2009) 111802, arXiv:0807.2405 [hep-ph].
- [74] A. Kulesza and L. Motyka, *Soft gluon resummation for the production of gluino-gluino and squark-antisquark pairs at the LHC*, Phys. Rev. **D80** (2009) 095004, arXiv:0905.4749 [hep-ph].
- [75] W. Beenakker, S. Brensing, M. Kramer, A. Kulesza, E. Laenen, et al., *Soft-gluon resummation for squark and gluino hadroproduction*, JHEP **0912** (2009) 041, arXiv:0909.4418 [hep-ph].
- [76] W. Beenakker, S. Brensing, M. Kramer, A. Kulesza, E. Laenen, and I. Niessen, *Supersymmetric top and bottom squark production at hadron colliders*, JHEP **1008** (2010) 098, arXiv:1006.4771 [hep-ph].
- [77] W. Beenakker, S. Brensing, M. Kramer, A. Kulesza, E. Laenen, et al., *Squark and gluino hadroproduction*, Int. J. Mod. Phys. **A26** (2011) 2637–2664, arXiv:1105.1110 [hep-ph].
- [78] M. Kramer, A. Kulesza, R. van der Leeuw, M. Mangano, S. Padhi, et al., *Supersymmetry production cross sections in pp collisions at $\sqrt{s} = 7$ TeV*, arXiv:1206.2892 [hep-ph].